UNIVERSITY OF CALIFORNIA,
IRVINE

Bi-Directional Brain-Computer Interfaces: Stimulation Artifact Suppression Design and Walking Exoskeleton Implementation

DISSERTATION

submitted in partial satisfaction of the requirements
for the degree of

DOCTOR OF PHILOSOPHY

in Biomedical Engineering

by

Jeffrey Lim

Dissertation Committee:
Professor Zoran Nenadic, Chair
Assistant Professor Beth Lopour
Professor Frithjof Kruggel

2023

DEDICATION

To my friends and family, for their patience and support.

TABLE OF CONTENTS

LIST OF FIGURES

LIST OF TABLES

ACKNOWLEDGMENTS

I would like to thank the National Science Foundation (NSF-1446908 and NSF-1646275) for funding this work.

I would also like to thank my colleagues at the Center for Biomedical Signal Processing and Computation: Mina Ibrahim, Claudia Serrano Amenos, Piyashi Biswas, Shravan Thaploo, Dr. Po T. Wang, Dr. An Do, and my advisor Dr. Zoran Nenadic, for all their support and contributions to my research.

I would also like to thank our collaborators at the Nanoscale Communication Integrated Circuits Labs at UCI, the Anderson Lab at Caltech, and the Neurology team and support staff at Rancho Los Amigos National Rehabilitation Center.

The text of this dissertation is a reprint of the material as it appears in [2, 3, 4, 5], used with permission from Frontiers in Neuroscience (Frontiers), the Journal of Neuroengineering (IOP Science), the IEEE Transactions on Biomedical Engineering (IEEE Computer Society) and the IEEE EMBS. The co-authors listed in these publications are Dr. Po T. Wang, Haoran Pu, Dr. Alireza K. Bidhendi, Dr. Omid M. Arasteh, Dr. Spencer Kellis, Dr. Susan J. Shaw, Dr. Michelle Armacost, Dr. Hui Gong, Dr. Charles Y Liu, Professor Payam Heydari, Professor Richard A Andersen, Assistant Clinical Professor An H. Do, Professor Zoran Nenadic.

VITA

Jeffrey Lim

EDUCATION

Doctor of Philosophy in Biomedical Engineering **2023**
University of California, Irvine *Irvine, California*

Advanced to Candidacy September 2019
Expected Defense Date: February 24th 2023
Advisor: Professor Zoran Nenadic

Bachelor of Science in Bioengineering **2015**
University of California, San Diego *La Jolla, California*

Cum Laude

RESEARCH EXPERIENCE

Graduate Student Researcher **2016–2023**
University of California, Irvine *Irvine, California*

TEACHING EXPERIENCE

Teaching Assistant **2018–2019**
University of California, Irvine *Irvine, California*

BME130: Biomedical Signals and Systems
BME170L: Biomedical Engineering Laboratory

Professional Experience

Diazyme Laboratories **June 2015–June 2016**
Biotechnician *Poway, California*

Collected and analyzed immunoassay data for automatic chemiluminescent analyzers

Autotelic Inc. **June 2013–October 2013**
Research Technician *City of Industry, California*

REFEREED JOURNAL PUBLICATIONS

An Energy-Efficient CMOS Dual-Mode Array Architecture for High-Density ECoG-Based Brain-Machine Interfaces **Dec 2019**

IEEE Transactions on Biomedical Circuits and Systems (Volume: 14, Issue: 2, April 2020)

O. Malekzadeh-Arasteh, H. Pu, **J. Lim**, C.Y. Liu, A.H. Do, Z. Nenadic, P. Heydari

Optimal artifact suppression in simultaneous electrocorticography stimulation and recording for bi-directional brain-computer interface applications **Apr 2020**

Journal of Neural Engineering

H. Pu, **J. Lim**, S. Kellis, C.Y. Liu, R.A. Andersen, A.H. Do, P. Heydari, Z. Nenadic

Artifact propagation in subdural cortical electrostimulation: Characterization and modeling **Oct 2022**

Frontiers in Neuroscience

J. Lim, P.T. Wang, S.J. Shaw, H. Gong, M. Armacost, C.Y. Liu, A.H. Do, P. Heydari, Z. Nenadic

A Benchtop and Bedside Validation of a Low-cost Programmable Cortical Stimulator in a Testbed for Bi-directional Brain-Computer-Interface (BD-BCI) Research. **Dec 2022**

Frontiers in Neuroscience

W.J. Sohn, **J. Lim**, P.T. Wang, H. Pu, O. Malekzadeh-Arasteh, S.J. Shaw, M. Armacost, H. Gong, S. Kellis, R.A. Andersen, C.Y. Liu, P. Heydari, Z. Nenadic, A.H. Do

REFEREED CONFERENCE PUBLICATIONS

Characterization of Stimulation Artifact Behavior in Simultaneous Electrocorticography Grid Stimulation and Recording **Jul 2018**

40th Annual International Conference of the IEEE Engineering in Medicine and Biology Society (EMBC)

J. Lim, P.T. Wang, A.K. Bidhendi, O. Malekzadeh-Arasteh, S.J. Shaw, M. Armacost, H. Gong, C.Y. Liu, P. Heydari, A.H. Do, Z. Nenadic

Dipole cancellation as an artifact suppression technique in simultaneous electrocorticography stimulation and recording **Mar 2019**

9th International IEEE/EMBS Conference on Neural Engineering (NER)

J. Lim, P.T. Wang, H. Pu, C.Y. Liu, S. Kellis, R. A. Andersen, P. Heydari, A.H. Do, Z. Nenadic

Pre-whitening and Null Projection as an Artifact Suppression Method for Electrocorticography Stimulation in Bi-Directional Brain Computer Interfaces **Jul 2020**

42nd Annual International Conference of the IEEE Engineering in Medicine & Biology Society (EMBC)

J. Lim, P.T. Wang, S.J. Shaw, M. Armacost, H. Gong, C.Y. Liu, A.H. Do, P. Heydari, Z. Nenadic

A Fully-Integrated 1μW/Channel Dual-Mode Neural Data Acquisition System for Implantable Brain-Machine Interfaces **Nov 2021**

43rd Annual International Conference of the IEEE Engineering in Medicine & Biology Society (EMBC)

O. Malekzadeh-Arasteh, H. Pu, A.R. Danesh, **J. Lim**, P.T. Wang, C.Y. Liu, A.H. Do, Z. Nenadic, P. Heydari

SUBMITTED ABSTRACTS

Artifact propagation in electrocorticography stimulation **May 2018**

Seventh International BCI Meeting, Abstract Book

J. Lim, P.T. Wang, S.J. Shaw, M. Armacost, H. Gong, C.Y. Liu, P. Heydari, A.H. Do, Z. Nenadic

BOOK CHAPTERS

BCI-Based Neuroprostheses and Physiotherapies for Stroke Motor Rehabilitation **Nov 2022**

Neurorehabilitation Technology (Pages 509-524)

J. Lim, D. Lin, W.J. Sohn, C.M. McCrimmon, P.T. Wang, Z. Nenadic, A.H. Do

ABSTRACT OF THE DISSERTATION

Bi-Directional Brain-Computer Interfaces: Stimulation Artifact Suppression Design and Walking Exoskeleton Implementation

By

Jeffrey Lim

Doctor of Philosophy in Biomedical Engineering

University of California, Irvine, 2023

Professor Zoran Nenadic, Chair

The prevalence of neurodegenerative diseases and injuries that result in motor impairment, such as stroke and spinal cord injury, have motivated researchers to explore brain-computer interface (BCI) technologies as a solution to treat damaged neural functions. More specifically, these BCIs promise to either rehabilitate, supplement or bypass affected areas by allowing patients to power motor prostheses or other assistive devices using neural signals. The most recent BCI research has increasingly focused on invasive neural interfacing modalities such as electrocorticography and microelectrode arrays, which confer advantages such as higher spatial resolution and larger frequency bandwidth. They also provide the capability of delivering cortical electrostimulation to elicit artificial sensory feedback, which is critical to motor functions. A BCI implementing closed-loop electrostimulation sensory feedback control is referred to as a "bi-directional" brain-computer interface (BD-BCI). These BD-BCIs improve on uni-directional designs in that they restore function in a more biomimetic fashion, and feedback has the potential to improve BCI performance. Invasive BD-BCIs also possess the potential to be realized as fully implantable devices, which greatly improves the practicality of these devices for chronic use.

A number of design obstacles, however, must be resolved before a fully implantable BD-BCI

can be realized. One such problem is that the simultaneous stimulation and recording necessary for motor BD-BCI causes strong electrical artifacts to propagate to the recording site. These artifacts can potentially obscure neural features or saturate analog front-ends. To begin to address these problems, our work first characterizes the propagation of stimulation artifacts using data collected during clinical cortical mapping procedures. We then detail how these artifact characteristics can be exploited by artifact suppression methodologies. Additionally, we also propose dipole cancellation as an analog front-end artifact suppression method designed to safeguard against amplifier saturation. We also propose a digital back-end method that utilizes pre-whitening and null projection to efficiently suppress residual artifacts persisting through front-end artifact suppression methods. Finally, we show a demonstration of an embedded BD-BCI exoskeleton system that abides by fully-implantable constraints. This device allowed a human subject implanted with ECoG electrodes to wirelessly control a robotic leg exoskeleton, as well as delivered electrostimulation-induced leg sensation during leg swing.

Chapter 1

Introduction and Background

1.1 Introduction to Brain-Computer Interfaces

A number of medical conditions and injuries in the central or peripheral nervous system can result in a spectrum of impairment ranging from partial paralysis to complete locked-in syndrome. These include amyotrophic lateral sclerosis (ALS), spinal cord injury (SCI), brain stroke, and other neuromuscular diseases such as Parkinson's. A commonality in these cases is that the neural pathways responsible for the impaired functions are partially intact. For example, even a person with paraplegia or tetraplegia may retain electrophysiological signals in the central nervous system that correspond with motor intent and experience sensation at infra-lesional locations if the correct neural circuits are activated. Due to this phenomena, there has been increasing scientific interest in brain-computer interface (BCI) technologies, which promise to allow affected persons to treat their impairment by rehabilitating or replacing their lost functions. Rehabilitative BCI [6] seek to facilitate recovery of damaged neural pathways by allowing the subject to practice the lost function to induce neuroplastic restoration of those pathways. In other cases where the impairment is more severe, perma-

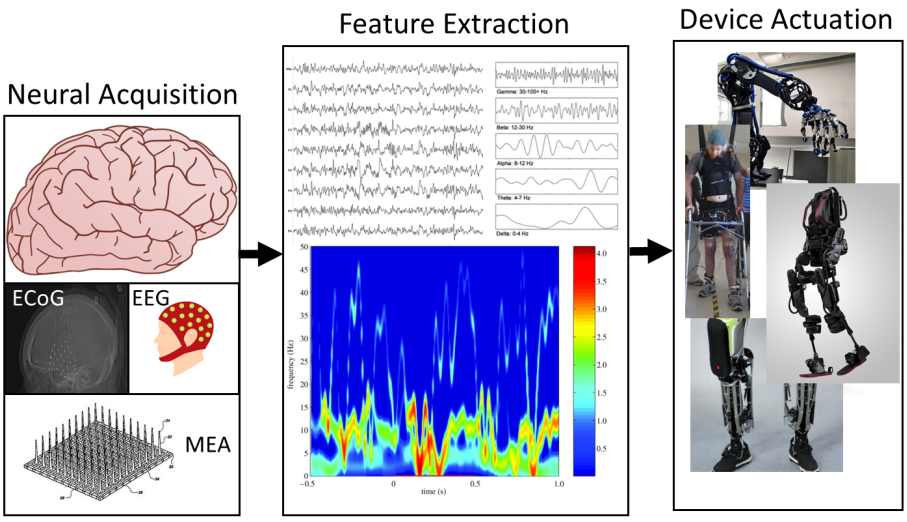

Figure 1.1: Typical BCI paradigm. BCIs utilize neural recording modalities to capture signals from the brain. These signals are processed for neural features that are induced by the behavioral tasks. Neural features are interpreted by the BCI and converted into commands for various types of end-effector devices.

nent replacement may be more suitable to allow the subject to bypass the damaged neural pathways with the BCI device [7].

In its simplest implementation, a BCI is a device that records electrophysiological signals from the nervous system, and then translates those signals into command signals for various types of end-effectors, like spellers and motor prostheses [7, 8]. This paradigm (see Figure 1.1) requires methodologies to capture these electrophysiological signals, which can range from invasive to non-invasive (see Figure 1.3). Examples that will be discussed in this work include electroencephalography (EEG), electrocorticography (ECoG), and intracortical microelectrode arrays (MEAs). Behavioral tasks, such as physical or imagined movements, can cause changes in the electrophysiology that can be captured by these recording methods. We refer to these types of phenomena as neural features, which can be extracted from recorded data using signal processing and statistical techniques. Such neural features can be captured by BCI and interpreted using machine learning and pattern recognition methods in order generate commands to control end-effectors [9]. In the following sections, we will

discuss the utility of the aforementioned recording modalities, as well as examples of BCI using them.

1.2 Electroencephalography-based BCI

EEG is a popular choice for neural electrophysiological recording in BCI due to its accessibility and ease of use. EEG records the cumulative electrical activity of large populations of neurons from the scalp [10]. Arrays of EEG electrodes are typically mounted onto an elastic fabric cap and are affixed to physiologically predetermined locations on the scalp (see Figure 1.2) using a conductive gel, which minimizes the impedance of the electrode-scalp interface. Event-related synchronization or desynchronization (ERS/ERD) [11] of the firing patterns of populations of neurons in response to behavioral tasks gives rise to neural modulations at specific frequencies. A classic example of such modulation is the synchronization of EEG oscillations in the α frequency range (8-12 Hz) in response to an awake human subject keeping their eyes closed [12]. This causes a measurable change in the spectral power in the α range in the parietal region that can be quantified using time-frequency analyses. BCI can utilize this aspect of these features to predict behavior and to control end-effectors.

An early example of BCI utilizing EEG is the P300 speller [13, 14]. These devices use the P300 feature, which is a positive voltage deflection occurring over the parietal area 300 milliseconds after a novel visual stimuli is presented. The BCI speller utilizes the P300 by displaying the subject an array of random letters. When the letter the subject desires to type appears, the P300 is triggered, which is detected by the BCI. The BCI then uses classifiers to determine which letter to type. In this way, locked-in subjects with conditions like ALS, are able to use this method of typing to communicate [15, 16]. Other common EEG BCI applications seek to restore motor functions for those suffering from conditions like stroke [17], traumatic brain injury or SCI. These seek to utilize imagined or actual

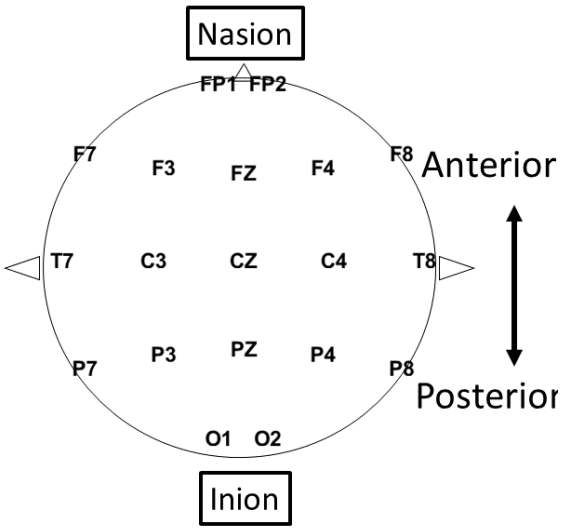

Figure 1.2: Diagram for 19-channel EEG following the international 10-20 EEG standard.

movements to modulate sensorimotor neural rhythms in order to power end-effectors such as functional electrical stimulation (FES) or robotic prosthetics. For example, our lab has previously demonstrated the ability for EEG-controlled FES to restore walking capability in a paraplegic subject [18]. Other applications have included motor-imagery controlled robotic arm for stroke rehabilitation [19] and virtual avatar controlled walking simulators [20]. Despite successes using EEG-based BCI, they still have limitations that have motivated researchers to consider alternative methods.

1.3 Invasive Brain-Computer Interfaces

Invasive recording modalities confer several advantages to BCI, primary of which are increased frequency bandwidth and spatial resolution [21]. Typical EEG records a frequency range of 0.5-50 Hz [22], largely due to artifacts resulting from line noise (60 Hz) and muscle activity occurring at frequencies greater than 50 Hz. EEG also has a limited spatial resolution, as it natively captures neural signals that are dispersed since they must propagate through brain tissue, cerebrospinal fluid, skull and scalp tissue. Modeling studies estimate

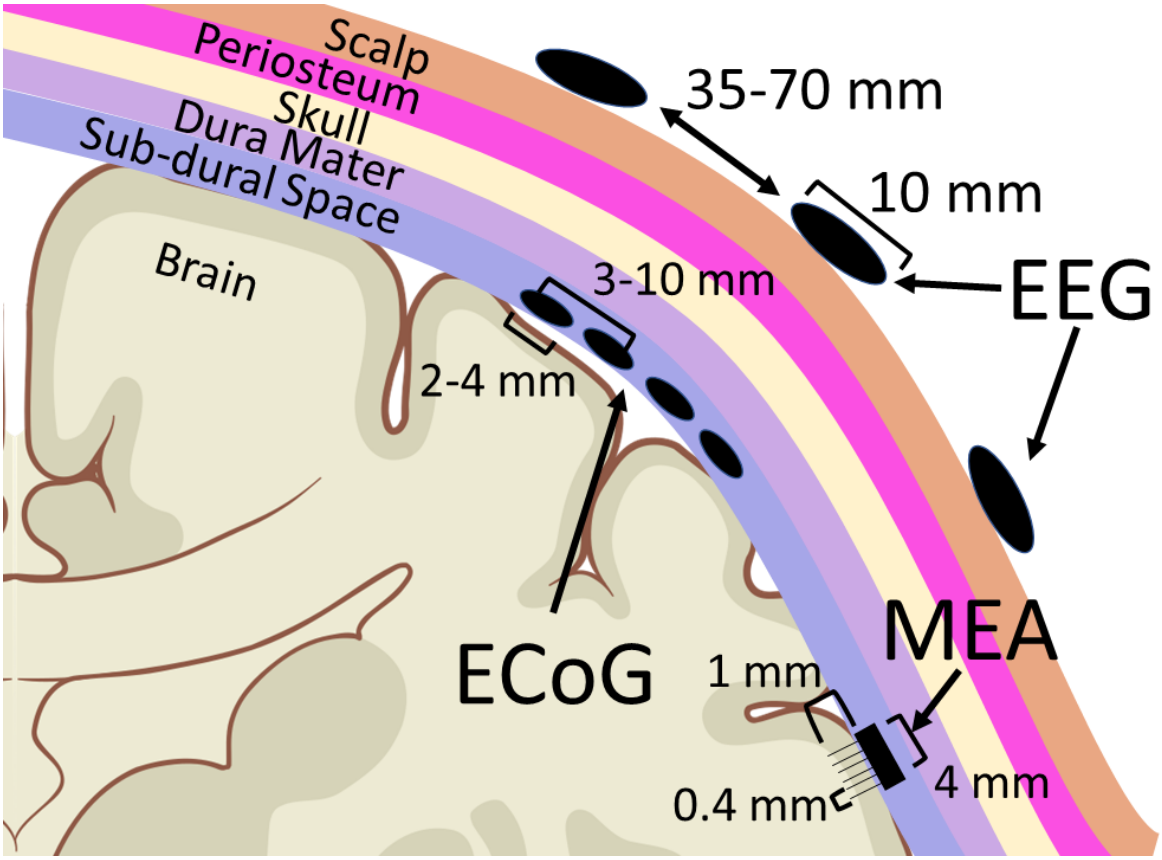

Figure 1.3: Dimensions and placement of EEG, ECoG and MEA electrodes. Brain tissue layer sizes are exaggerated for visibility. Ranges for measurements are given based on common sizes for each recording modality.

that the standard 19 electrode 10-20 system has an estimated spatial resolution of 22-37 cm^2, with higher density 129 electrode having 6-8 cm^2 [23]. An improvement to the spatial and frequency properties of EEG can be achieved by using ECoG, which is an array of platinum or stainless steel electrodes embedded in a flexible plastic sheath implanted in the subdural space (cf. Figure 1.3). In contrast to EEG, ECoG typically exhibits a frequency bandwidth extending up to the high-γ band (80-160 Hz). These higher frequency oscillations contain critical information for more advanced BCI processes, such as phoneme decoding [24] and multiple degree-of-freedom motor control [25, 26]. With regards to spatial resolution, commercial ECoG grids typically comes in standard ($\sim$10 mm) and high-density ($3-4$mm) arrangements, allowing researchers to tailor the spatial resolution to their application. For example in sensorimotor BCI applications, it may be useful to have one ECoG grid spanning both the sensory and motor cortices to encompass both types of neural activity. Alternatively, denser grids have demonstrated the capability of capture highly localized high frequency activity [27, 28, 29]. Similarly, MEA electrodes significantly increase the spatial resolution by utilizing micrometer-scale, penetrating, "shank" probes arranged in up to 16×16 arrays with 200-400 μm in between. These MEAs are inserted into the brain tissue itself, allowing them to measure both local field potentials (LFPs), as well as action potentials [30]. The improved spatial and spectral resolution of both ECoG and MEAs have been greatly utilized for BCI devices [21].

The first of human invasive-based BCIs implemented computer screen cursor control based on ECoG signals [31]. This device demonstrated how simple one-dimensional BCI control could be achieved with a variety of imagined and physical behavioral tasks, including hand opening/closing, speech, and tongue protrusion. Other data collected in this study was also used to perform offline decoding using neural networks. These analyses showed that frequencies up to 200 Hz contained relevant information for decoding, providing a basis for more modern ECoG BCI. Subsequent studies include 3D cursor control using a custom high-density ECoG grid [32], reach/grasp tasks with arm exoskeleton [33], and an arm exoskeleton

rehabilitative BCI for chronic stroke survivors [34]. Similarly, studies utilizing MEA-based BCI control include various 3D robotic arm control studies in tetraplegic subjects [35, 36, 37]. Though these studies have been mostly demonstrated in a laboratory setting, their success supports the viability of using invasive recording modalities for more widespread use in treating a variety of motor conditions. A chief motivator for this is that these invasive BCI can be realized as fully-implantable devices, which significantly improves the practicality of BCI devices, which currently typically rely on bulky, non-portable, external hardware. A fully-implantable implementation also removes the need for ECoG or MEA transdermal access ports, which are undesirable in the long term due to infection risk and unappealing aesthetics. To date, Vansteensel et. al [38] have demonstrated the use of an ECoG-based fully implantable BCI speller device in ALS patients. Additionally, a responsive neural stimulator (RNS) utilizing ECoG [39, 40] has recently attained FDA approval, paving the way for fully-implantable BCI incorporating electro-cortical stimulation for feedback. This is a functionality that is unique to invasive BCI and is especially critical for motor BCI seeking to implement sensory feedback, which is critical to normal motor function [41, 42, 43] and improves BCI control [44, 45].

1.4 Artificial Sensation

Early on in BCI prosthetics research, it was evident that adoption of the technology would be contingent on the ability for these prostheses to provide sensory feedback. The few BCI implementing some type of sensation at the time typically relied on vibrotactile [46] or epidermal electrostimulation [47] feedback. More commonly, as is still the case today, most BCI would rely solely on visual feedback. Advances in biomaterials and electrical hardware have since made it possible to apply electrostimulation directly to the cortex using the same ECoG and MEA grids used to record neural signals. Though direct cortical electrostimulation in

this way is most regularly used clinically for cortical mapping procedures in epilepsy surgical evaluations [48], researchers also found the technique useful for identifying eloquent cortex for sensorimotor function [49]. More recent work has described the process of evoking artificial sensation using ECoG [50, 51, 52] and MEA [53, 54] electrodes. Additionally, unlike the other forms of feedback, naturalistic sensory responses were reported by some of the subjects in this study, like brushing or tapping at specific cutaneous locations, or even proprioceptive movement sensations. Thus arises the opportunity to incorporate these sensory functions into existing invasive motor BCI, resulting in what is referred to as a bi-directional BCI (BD-BCI).

1.5 Bi-Directional Brain-Computer Interfaces

As the name implies, a BD-BCI combines the feed-forward path that decodes neural signals and controls an end-effector with the feedback path that delivers electrostimulation directly to the cortex (see Figure 1.4). The bi-directional paradigm is especially critical in motor applications, where sensory and proprioceptive information is key to proper motor function [41, 42, 43]. Rouse et. al [55] and Stanislaski et. al [56] present one of the first examples of a fully-implantable device with both sensing and stimulation capabilities, though the stimulation feedback is intended for cessation of Parkinson's motor tremor, not sensory feedback. On the other hand, Flesher et al. [44] presents a study wherein they demonstrate the integration of intracortical microstimulation sensory feedback with MEA-based BCI control of a robotic arm. All of these studies report the difficulties in implementing both recording and stimulation functions simultaneously, as strong electrical artifacts propagate from the stimulation site to the recording site. This can result in interruptions of BCI decoding performance as the frequency response of somatosensory stimulation [51, 52] often overlaps with the bandwidth of physiological neural signals like high-γ [27, 26, 25]. BD-BCI therefore must

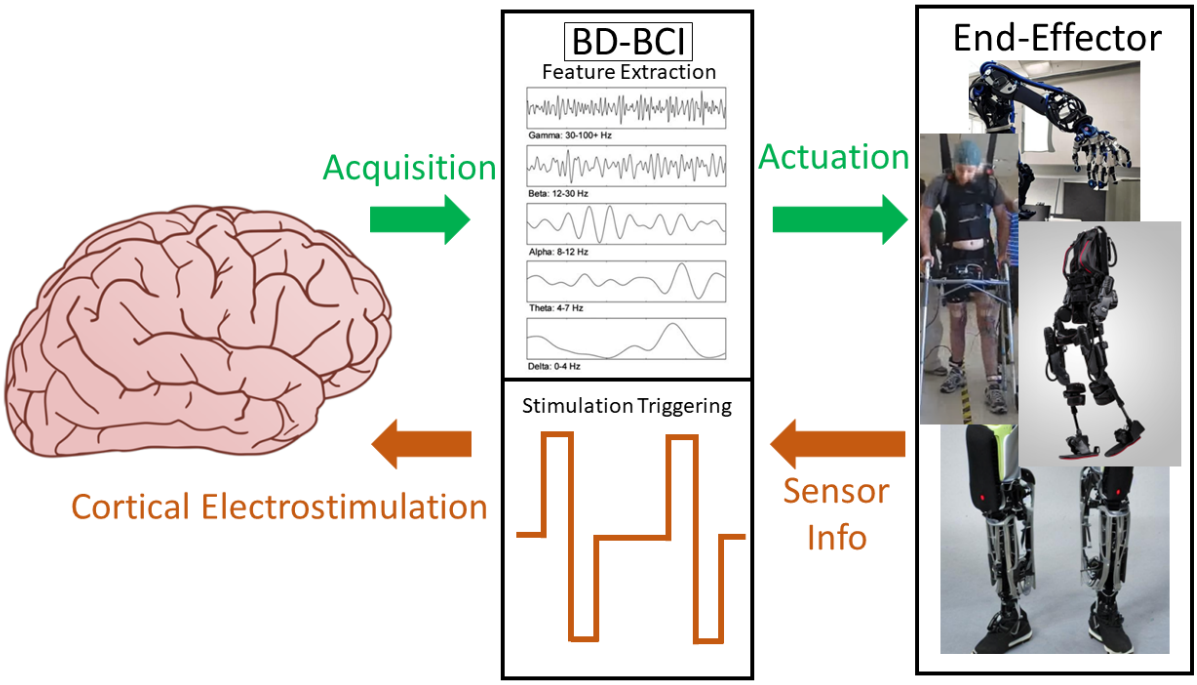

Figure 1.4: Diagram of BD-BCI operation. Feed-forward decoding path is the same as for BCI. BD-BCI adds feedback path in the form of cortical electrostimulation triggered based on information from sensors on the end-effector.

implement efficient artifact suppression strategies to enable both neural signal acquisition and sensory feedback stimulation simultaneously.

1.6 Artifact Suppression Strategies

A necessary pre-condition for artifact suppression strategies is that large-amplitude (i.e. artifacts$\sim$mV, ECoG neural signal $\sim$50-100 μV) stimulation artifacts must be properly captured without saturating recording front-ends. To this end, hardware innovations have been devised to increase front-end dynamic range [57, 58] to enable neural recording in the presence of artifacts. Other front-end approaches, like our recently-developed dipole cancellation [3, 59] safeguard against saturation, while adaptive filtering [60] and template subtraction [61] reduce artifacts in the captured data. Even with the implementation of such meth-

ods, residual artifacts will persist and must be additionally suppressed by digital back-end methods.

The simplest of these back-end methods include blanking-reconstruction techniques, wherein data samples containing artifacts are removed and subsequently replaced by sample-and-hold [62] or interpolated [63, 64, 65] data points. Current BD-BCIs [44] typically implement this method and interleave the stimulation and recording. However, this approach is suboptimal since it records data intermittently, thereby degrading the performance of BCI decoding algorithms. Additionally, such a BD-BCI system can only provide intermittent feedback. Alternative approaches have been tried by other groups, for example Stanslaski et al. proposed to orient the ECoG stimulation electrodes in a way that minimizes the artifact presence at the recording site [56]. Subsequently, they applied frequency-domain filtering to remove the residual artifacts [56, 55].

Another approach to null residual artifacts is to construct an artifact template by averaging artifact waveforms and subtract the template from the signal [66, 67]. Signal decomposition techniques, such as independent component analysis (ICA) [68, 69] or emprical mode decomposition (EMD) [70, 71], have been useful in separating artifacts from neural data and are thus considered state-of-the-art artifact suppression techniques. Many of these techniques, however, can create significant signal distortions due to data removal (blanking-reconstruction) or replacement (template subtraction). Furthermore, ICA-based methods may struggle with separating artifact and neural subspaces, as they are not guaranteed to be independent. Similarly, EMD may struggle in situations where the frequency response of the neural signal and stimulation overlap, as is often the case in motor BD-BCI applications. Ultimately, the problem of simultaneous stimulation and recording is still unresolved for BD-BCI, and further work must be performed before these devices can be fully realized.

1.7 Significance of This Work

In this dissertation, we discuss the problem of stimulation artifacts for BD-BCI, as well as methods for artifact suppression and an implementation for a walking exoskeleton BD-BCI system. First, we present a characterization study for stimulation artifacts in ECoG [2, 5]. We used data collected during cortical electrostimulation procedures performed as part of clinical epilepsy mapping procedures (Phase II epilipse surgical evaluation). The characterization analysis provides temporal, spectral and spatial features of artifacts, which can then utilized to improve or inspire new artifact suppression strategies.

Subsequently, we propose methods for artifact suppression that can be employed at the front-end and back-end of BD-BCI devices. As the first challenge posed to BD-BCI is the resolution of large stimulation artifacts without saturating front-end amplifiers, we propose a front-end method for safeguarding against amplifier saturation. We refer to this method as dipole cancellation [3, 59], which is a method utilizing multiple stimulation dipoles to reduce the amplitude of artifacts propagating from a stimulation site to a recording site. In this work, we demonstrate the effectiveness of this method in a brain phantom approximating the electrical conductive properties of brain tissue [3].

After artifact suppression is performed at the front-end, the next challenge BD-BCI must address is that residual artifacts persist to the back-end of the device. In regards to this, we propose an algorithm utilizing pre-whitening and null projection (PWNP). The effectiveness of this method is assessed in a variety of neural recording modalities, including EEG, ECoG and MEAs. The artifact suppression results of the PWNP method are then compared against a current state-of-the-art ICA-based method. We thus demonstrate how the PWNP method can serve to efficiently suppress artifacts, and could potentially be used to enable real-time BD-BCI operation.

Finally, we use the principles discussed in this work to devise a walking exoskeleton BD-

BCI system. Existing examples of motor BD-BCI implementing cortical electrostimulation feedback have used robotic arm prosthetics [72, 44]. There also exists a study implementing a long-term ECoG-based walking exoskeleton [73], but this study does not implement sensory feedback stimulation. To build upon these studies, we present a prototype, embedded systems BD-BCI that abides by fully-implantable constraints that we have integrated with a walking leg exoskeleton. The performance of this system was demonstrated with a single subject (Phase II epilepsy monitoring), who wirelessly controlled the exoskeleton with motor-modulated neural signals, while simultaneously receiving cortical electrostimulation sensory feedback during exoskeleton leg swing. As our BD-BCI has been designed with implantability in mind, we propose this study supports the viability of future iterations of this device to serve as a fully-implantable BD-BCI for walking exoskeleton applications. These could then be implanted in SCI subjects suffering from paraplegia or tetraplegia, restoring their sensorimotor walking function.

Chapter 2

Artifact Propagation in Subdural Cortical Electrostimulation: Characterization and Modeling

2.1 Motivation

Despite the need for a characterization of electrostimulation artifacts in invasive neural recording modalities, there have been few attempts to provide a comprehensive analysis of spatial, temporal and spectral features in simultaneous neural recording and stimulation. This is surprising given the prevalence of clinical ECoG mapping in epilepsy surgical evaluation (Phase II epilepsy monitoring). We used data from four ECoG subjects to perform analyses of ECoG stimulation artifacts in the temporal, frequency and spatial domains. As previous works suggest that conduction of neural signals through neural tissue follows dipole volume conduction [74, 75, 76, 77, 78], we also conducted a modeling study to ascertain whether the dipole model is an accurate model of the stimulation artifact of the stimula-

tion artifact propagation. Collectively, these findings deepend our understanding of cortical electrostimulation and provide critical design specifications for future BD-BCI systems.

2.2 Methods

2.2.1 Subject information and ECoG stimulation procedure

Four patients undergoing Phase II epilepsy monitoring gave written informed consent to participate in the study. Subject 1 and 3 were implanted with platinum ECoG grids (Ad-Tech, Oak Creek, WI). Subjects 2 and 4 had platinum-iridium ECoG grids (Integra Life-Sciences, Plainsboro, NJ) implanted. The placement and number of ECoG grids/strips, as well as the choice of stimulation electrodes were solely guided by clinical needs. We only analyzed the stimulation epochs from grids that had all electrodes stimulated (representative grids). Other implanted grid/strips were excluded because they had either incomplete or no stimulation coverage.

We recorded clinical ECoG data at the bedside during eloquent cortex mapping procedures. These procedures are a standard part of Phase II epilepsy monitoring and entail electrostimulation of cortical tissue across sequential channels of the ECoG grids. A bipolar stimulation channel consisted of a pair of adjacent electrodes connected to a Natus®Nicolet™ Cortical Stimulator (Natus Medical Incorporated, Pleasanton, CA). For each stimulation channel, the stimulator delivered a biphasic square pulse train with equal-length anodic/cathodic pulse width ranging from 200 to 250 μs over a short stimulation epoch. The duration of stimulation epochs varied from 2 to 5 seconds across subjects. The stimulation amplitude also varied from 2 mA to 12 mA, typically in 2 mA increments. Note that the choice of stimulation channels and parameters was solely guided by clinical needs. See Table 2.1 for a comprehensive list of stimulation parameters and representative grid information for each

Table 2.1: Stimulation parameters and representative grid information.

Stim./Grid Parameters	Subject 1	Subject 2	Subject 3	Subject 4
Stimulation Frequency (Hz)	50	50	50	50
Pulse Width (μs)	200	250	200	250
Epoch Duration (s)	3	5	2	2
Amplitude (mA)	2-8	2-10	3-12	2-12
Grid Vendor	Integra	Ad-Tech	Integra	Ad-Tech
Grid Type	Standard	Standard	High Density	High Density
Electrode Spacing (mm)	10	10	3	4
Electrode Diameter (mm)	4.75	4.00	2.00	2.00
Exposure Diameter (mm)	1.5	2.3	1.0	1.0
Reference/Ground	LPG1/2	LTG19/20	Off-grid	Off-grid

subject. We acquired ECoG data at 512 Hz using a Natus®Quantum™ amplifier (Natus Medical Incorporated, Pleasanton, CA) during the entire mapping procedure and annotated stimulation channels and epochs. This amplifier had a $\pm$ 3 dB linear range 0.01 - 219 Hz for 512 Hz sampling rate.

2.2.2 MR-CT Image Segmentation and Co-Registration

A more detailed description of the MR-CT co-registration procedure is described in Appendix A. To aid in the artifact propagation characterization, we first determined the coordinates of the ECoG electrodes in reference to the brain. Specifically, we used pre-implantation MRI (post-explantation MRI for Subject 4) and post-implantation CT images to co-register the ECoG electrodes with brain-segmented MR images. For this purpose, we used the Elastix toolbox [79, 80], which performs nonrigid co-registration of MRI and CT images. We used default parameters and a normalized mutual information similarity metric. We fixed the CT image to preserve the electrode coordinates, while moving the MR image until it was transformed to the CT coordinate space. We then segmented the transformed MRI using the Mango [81, 82, 83] segmentation plugin to prepare for co-registration with the electrode coordinates segmented from the CT images.

The segmentation of the electrode coordinates from subject post-implantation CT data followed the procedure described in [84]. First, to identify the electrode locations, we thresholded the CT intensity data. For each electrode location, this procedure generated an intensity point cluster. Subsequently, we ran a clustering algorithm utilizing DBSCAN [85] that returned the center-point for each electrode in the array. These CT-space electrode coordinates were then overlaid onto the transformed MRI-segmented brain to complete the co-registration process. Finally, we scaled the coordinates by the CT image voxel dimensions (mm) to convert from voxels to physical space.

2.2.3 Time Domain Analysis

We collected ECoG data at the bedside during cortical electrostimulation procedures. Each time the subject received stimulation, we timestamped the corresponding stimulation epoch so that these data could be subsequently identified and segmented out for further analysis. For each subject, this procedure generated several hours of data. We used MATLAB (MathWorks, Natick, MA) for data processing and analysis. The signals were first visually inspected to assess the quality of the baseline ECoG data and confirm the presence of stimulation artifacts. Subsequently, for each channel, we removed low-frequency drifts by high-pass filtering at $\geq$1.5 Hz (zero-phase, first-order, Butterworth filter). Note that this filter had negligible effects on the rest of the signal (see Figure 2.2). We then segmented the individual stimulation epochs from the rest of the data using the documented timestamps. The electrodes comprising the stimulation channel were excluded from the analysis due to amplifier saturation. Any electrodes with signals exceeding the clinical amplifier's saturation limit ($\pm$8.7 mV) were also excluded. For each remaining electrode, we identified the responses to individual biphasic pulses. Depending on the duration of the stimulation epoch (see Table 2.1), this procedure resulted in 100 to 250 pulse responses per stimulation epoch. Within each stimulation epoch and for each electrode, we then quantified the artifact

amplitude by finding the extreme value of each pulse response. This procedure was aided by utilizing the known pulse train frequency (50 Hz) and MATLAB's extrema detection algorithm.

2.2.4 Frequency domain analysis

To take advantage of the periodic nature of the stimulation signals and corresponding ECoG responses, we also analyzed data in the frequency domain. To this end, we divided each stimulation epoch into five equal, non-overlapping segments. We then performed the fast Fourier Transform (FFT) on each data segment and calculated their power spectral densities (PSDs). We repeated the same procedure for baseline epochs, defined as duration-matched periods immediately preceding the corresponding stimulation epochs. To quantify the effect of the stimulation across frequency, f, we calculated the interference index, $I(f)$, as:

$$I(f) = \frac{1}{2} \log \frac{\sigma_{\mathrm{t}}^2(f)}{\sigma_{\mathrm{on}}(f)\sigma_{\mathrm{off}}(f)} \tag{2.1}$$

where $\sigma_{\mathrm{on}}(f)$ and $\sigma_{\mathrm{off}}(f)$ are the frequency-dependent standard deviations of the stimulation and baseline PSDs, respectively, and $\sigma_{\mathrm{t}}^2(f)$ is the total variance calculated as [86]:

$$\sigma_{\mathrm{t}}^2(f) = \frac{\sigma_{\mathrm{on}}^2(f) + \sigma_{\mathrm{off}}^2(f)}{2} + \frac{\left[\mu_{\mathrm{on}}(f) - \mu_{\mathrm{t}}(f)\right]^2}{2} + \frac{\left[\mu_{\mathrm{off}}(f) - \mu_{\mathrm{t}}(f)\right]^2}{2} \tag{2.2}$$

In the above equation, $\mu_{\mathrm{on}}(f)$ and $\mu_{\mathrm{off}}(f)$ are the frequency-dependent means of the stimulation and baseline PSDs, respectively, and $\mu_{\mathrm{t}}(f)$ is the total mean calculated as: $\mu_{\mathrm{t}}(f) = \frac{1}{2}(\mu_{\mathrm{on}}(f) + \mu_{\mathrm{off}}(f))$. Note that Equation (2.1) is a variant of the deflection coefficient [87] that can account for overlapping means and unequal variances between the stimulation-on and stimulation-off PSDs [88]. We also compared the power distribution in the stimulation-on and stimulation-off conditions across frequencies and tested the statistical significance of these differences by performing the Kolmogorov-Smirnov (KS) test.

2.2.5 Spatial domain analysis

Based on the artifact amplitudes calculated in the time domain analysis, we characterized each stimulation epoch by calculating its median artifact amplitude. We repeated this procedure for each electrode in the grid, and then interpolated and color-coded these median values to generate artifact spatial maps. From these maps, we defined a saturation region as the cortical area within which artifacts were large enough to saturate a hypothetical ULP amplifier. To this end, we first derived a saturation limit from the specifications of an implantable bi-directional BCI prototype [55]. Specifically, a supply voltage of 2.2 V and a gain of 66 dB (2000×) yielded a saturation limit of ±1,100 μV. We then marked this saturation limit as a contour on the artifact spatial maps and defined the contour interior as the saturation region. Finally, we quantified the extent of the saturation region by calculating the worst-case distance (WCD), defined as the maximum distance between the mid-point of the stimulation channel and the saturation contour.

2.2.6 Dipole model analysis

Our preliminary work suggests that the spatial distribution of artifacts follows the voltage distribution of an electric dipole [2]. To test this hypothesis, we estimated a dipole model from ECoG measurements and assessed its accuracy using an R-squared value. We then used the model to predict spatial distributions of artifacts and compared them to distributions generated from experimental data.

The spatiotemporal distribution of potentials due to a dipole in a homogeneous, isotropic, purely resistive medium is given by [89]:

$$\phi(x,y,z,t) = \frac{I(t)}{4\pi\sigma}\left(\frac{1}{\|r(x,y,z) - r_+\|} - \frac{1}{\|r(x,y,z) - r_-\|}\right) \tag{2.3}$$

where $\phi(x, y, z, t)$ is the potential field at a point (x, y, z) and time t, generated by a pair of positive and negative, time-dependent, point current sources with the position vectors $r_+ \in \mathbb{R}^3$ and $r_- \in \mathbb{R}^3$, respectively. The vector $r(x, y, z) \in \mathbb{R}^3$ defines the position of the point (x, y, z). Note that we defined these position vectors, r_+, r_-, and r, with respect to an arbitrarily chosen origin and that the choice of origin is irrelevant due to the homogeneity and isotropy assumptions. For the justification of cortical tissue behaving as a homogeneous, isotropic, purely resistive medium, we refer to [90, 91, 92, 89]. Finally, σ is the conductivity of the medium and $I(t)$ is current of the source/sink.

Taking the above considerations into account, the dipole equation can be reformulated as:

$$V_e = kI \left(\frac{1}{\|r_e - r_+\|} - \frac{1}{\|r_e - r_-\|} \right) + n, \qquad e = 1, 2, \cdots, N_e \tag{2.4}$$

where V_e is the artifact amplitude measured at electrode e, N_e is the number recording electrodes, and I is the amplitude of the stimulation current. The position vectors r_e, r_+, and r_- define the positions of the electrode e, the current source, and the current sink, respectively. We calculated these position vectors from the CT images with respect to an arbitrary origin. The slope parameter k accounts for the geometry of the current transmission path, the electrode size and material, and the impedance of the electrode-tissue interface. Finally, the intercept parameter n accounts for the placement of the reference electrode, background neural activity, and environmental noise. Note that the choice of the reference electrode was determined clinically (see Table 2.1). Generally, its position was not on a zero-potential line, defined theoretically as a line equidistant to the dipole source and sink. This may have contributed to a non-zero reference voltage that needs to be accounted for by n.

For a given dipole location, we measured the artifact amplitudes, V_e, at multiple stimulation currents, I, and estimated the parameters k and n in Equation 2.4 using a linear least-

squares approach. We also quantified the goodness-of-fit using the R-squared value. Once the parameters, $\hat{k}$ and $\hat{n}$, are estimated, we predicted the spatial distribution of artifacts, $\hat{V}_e$, using the model Equation (2.4). Finally, we interpolated the predicted artifact values and then mapped them onto the MR-CT co-registered images for visualization purposes.

2.3 Results

2.3.1 Co-Registration

Figure 2.1 shows the results of the co-registration procedure for all four subjects. Subsequently, we used these co-registration images for visualization purposes and spatial domain analysis. While we analyzed a single representative grid for each subject (see Table 2.1), we still obtained abundant data, with 6–21 dipoles per grid and 2–7 stimulation amplitudes per dipole. The analyzed grid for Subject 1 was a 4×5 standard grid implanted over the left, posterior parietal area. Subject 2 had a 4×5 standard grid implanted over the left temporal lobe. Subject 3 had a 4×8 high-density grid in the interhemispheric space over the left motor leg area. Finally, Subject 4 had a 4×8 high-density grid placed over the right motor arm area.

2.3.2 Time Domain Analysis

Visual inspection of the ECoG data at various time scales revealed salient features of stimulation artifacts. Looking on a minutes time scale, we easily identified the individual stimulation epochs, since stimulation created significant artifacts in the ECoG data across multiple electrodes.

On a seconds time scale, we observed large voltage deviations in the millivolts range during

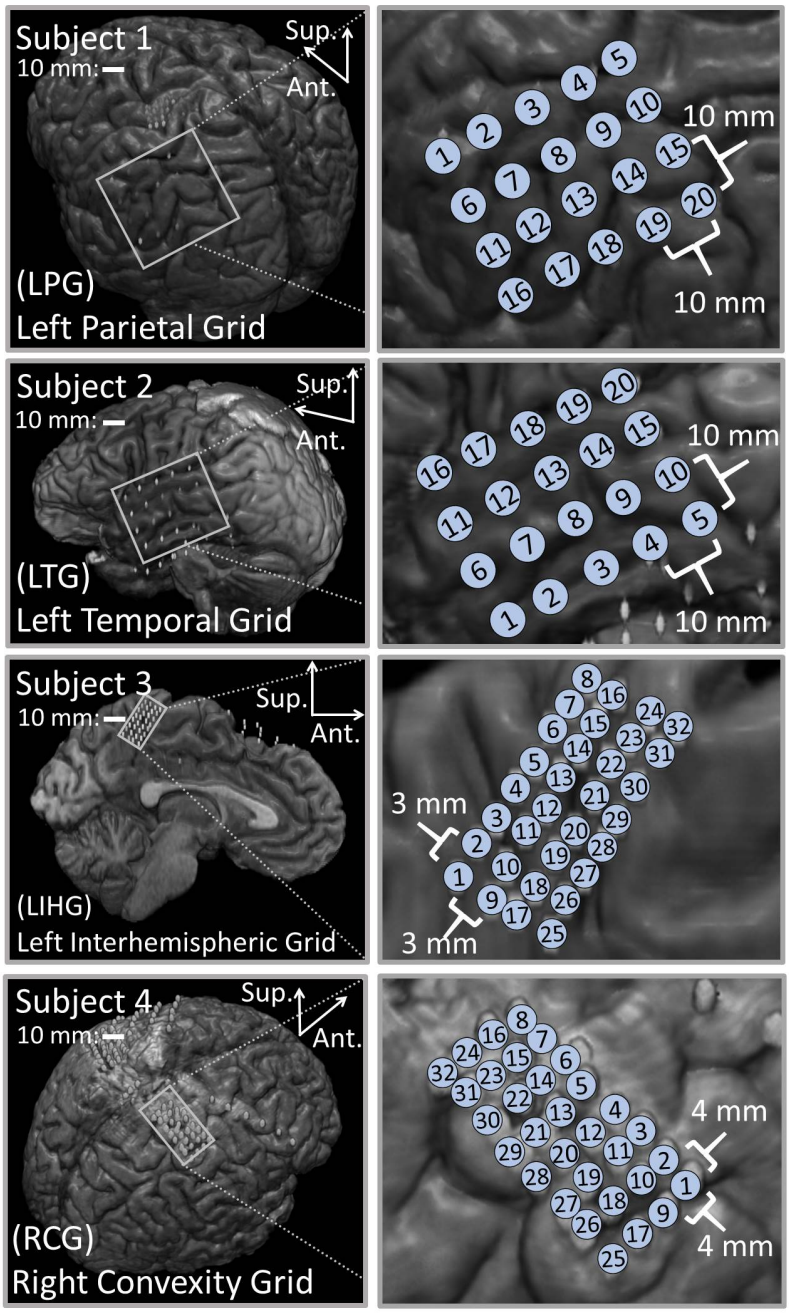

Figure 2.1: Co-registration of electrodes segmented from CT images and brain segmented from MRI. (Left) Co-registration image for each subject, with the representative grid outlined in white. Note that the points representing electrodes are not to scale. Also note that the co-registration image for Subject 3 shows a left hemisphere (sagittal plane) with electrodes in the inter-hemispheric fissure. (Right) Insets of representative grids with electrode numbers encircled. The label size is not related to the electrode size.

the stimulation epochs, particularly on electrodes close to the stimulating channel. These deviations are significantly larger than typical ECoG signals, which have an amplitude of 10's of microvolts [21, 25]. Despite the supposed charge balance of the biphasic square waveform, these electrodes accumulated a significant DC drift over the duration of the stimulation epoch (see Figure 2.2). This so-called "ratcheting effect" [93] was prominent in the raw ECoG data across all four subjects. The voltage drifts caused by the ratcheting effect generally exceeded the amplitude of the pulse responses by several fold, and occasionally drove electrodes adjacent to the stimulation channel to the saturation voltage of the recording system amplifier (± 8.7 mV). High-pass filtering at 1.5 Hz removed the ratcheting effect on non-saturated electrodes. Note that the polarity of the DC drift on ratcheting electrodes depended on their position with respect to the current source/sink at the onset of the stimulation.

Pulse responses across electrodes exhibited phase-locking on a milliseconds time scale, especially at higher stimulation amplitudes. More specifically, voltage peaks/troughs on artifact-affected electrodes occurred within 2 ms (1 sample) of each other (see Figure 2.3). This behavior was consistent across stimulation channels and grids. For all four subjects, the frequency of the pulse responses matched the frequency of the stimulation pulse train (50 Hz). These observations are consistent with the assumptions of the dipole model given by Equation (2.4).

2.3.3 Frequency Domain Characteristics

The power distribution of stimulation artifacts resembled the theoretical power spectrum of a biphasic pulse train (Figure 2.4). These similarities suggest that the propagation of artifacts from the stimulation channel to the recording electrodes can be approximated by a linear system. The system identification of such a model would require the simultaneous

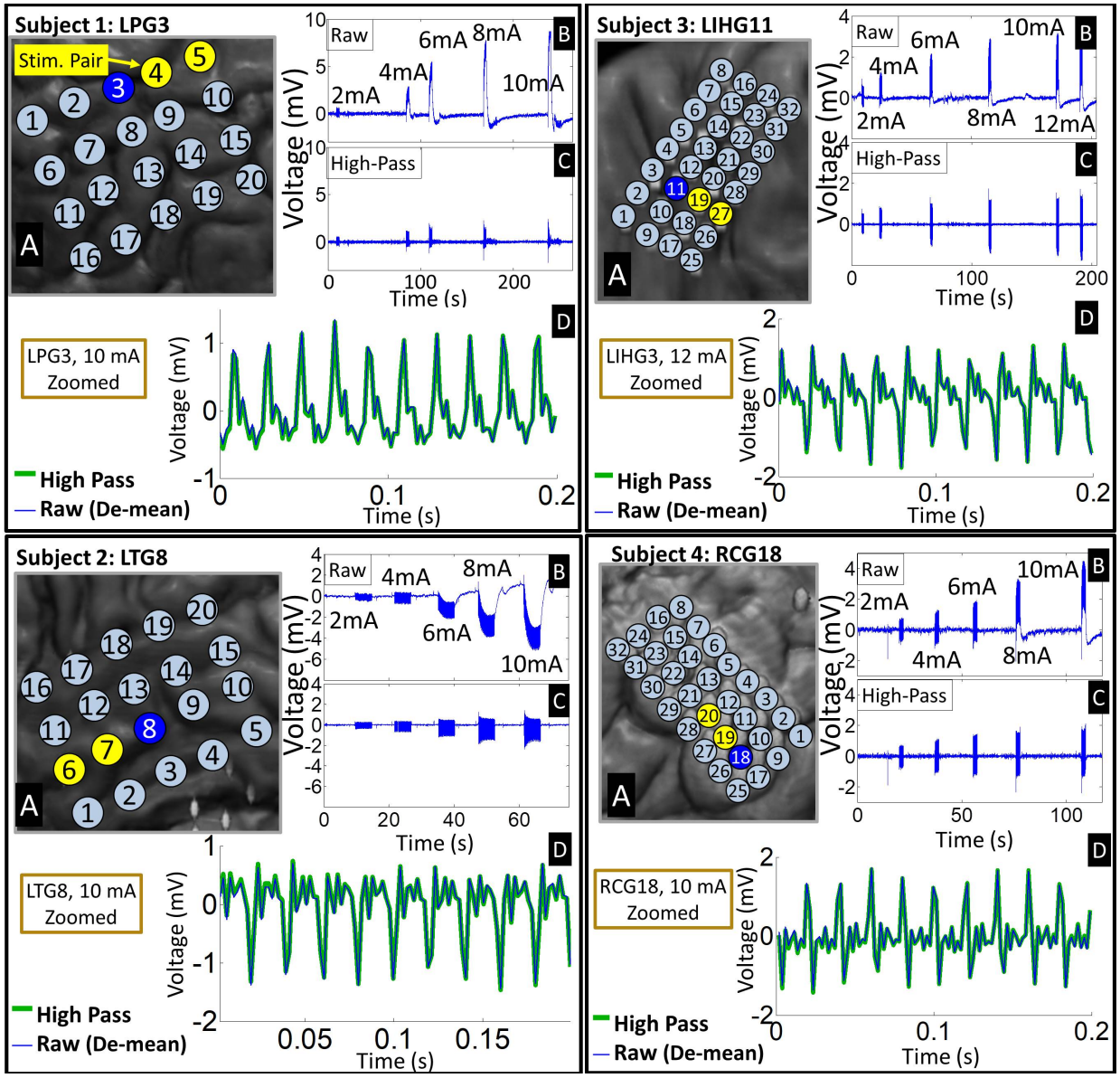

Figure 2.2: Representative examples of time-domain signal features across four subjects. (A) Insets of co-registered images showing the representative grid with the stimulation channel marked in yellow. (B) Time-domain signals from an electrode (marked by blue on the grid) adjacent to the stimulation channel exhibiting ratcheting effects. The raw waveforms show 5 - 6 stimulation epochs at different stimulation amplitudes. Note that ratcheting severity increases with stimulation amplitude. (C) The ratcheting is removed by high-pass filtering at 1.5 Hz. (D) A zoomed plot of the strongest artifacts before and after filtering shows that high-passing has negligible effect on the individual pulse responses. Raw signal is de-meaned so that it can be overlaid with high-passed signal.

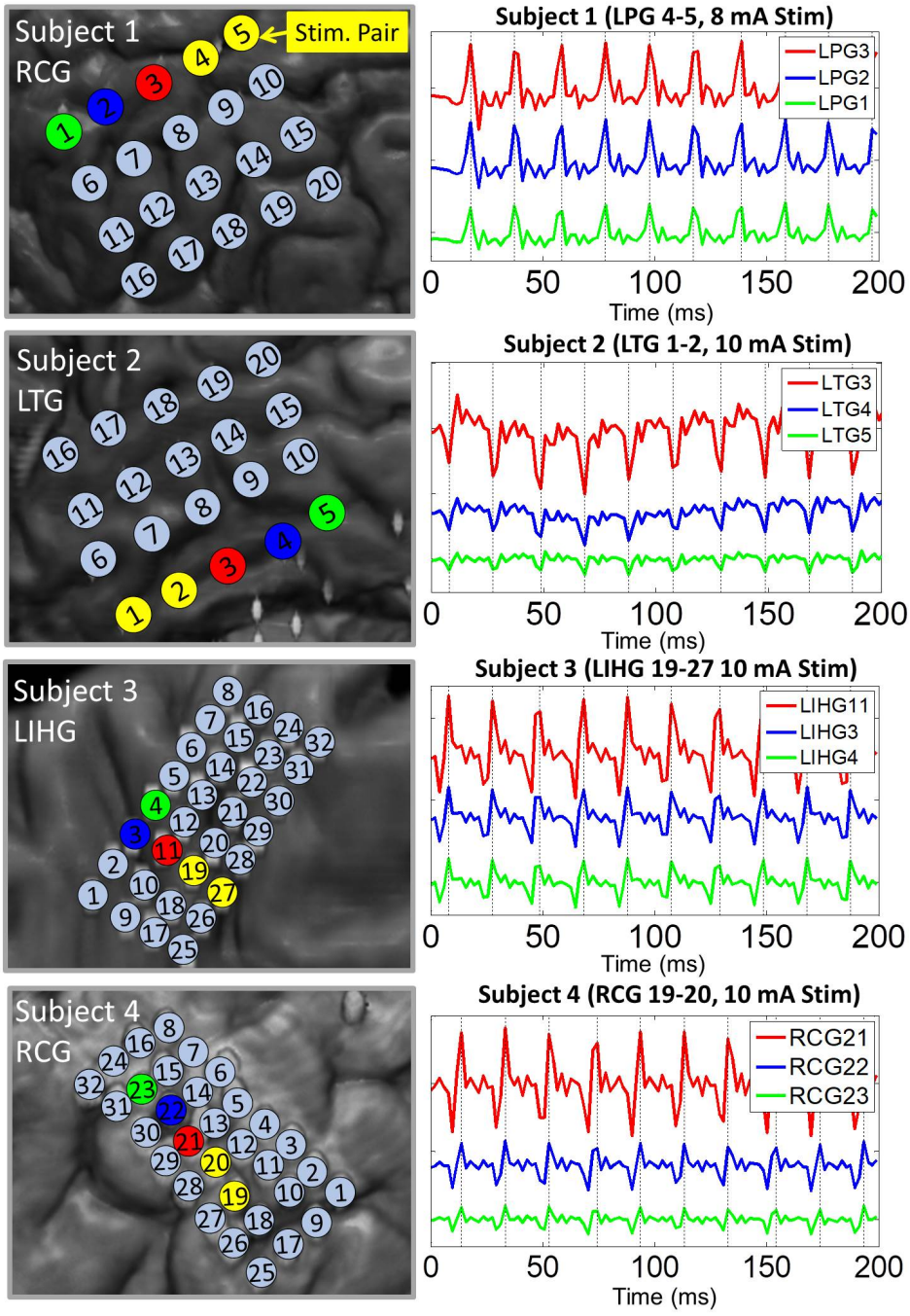

Figure 2.3: Representative examples of pulse response phase-locking in all 4 subjects. (Left) Insets of co-registration images, with color-coded electrodes lying in the direction of strongest artifact (co-linear with the dipole moment). (Right) ECoG data high-passed at 1.5 Hz with colors matched to the corresponding electrode. Artifact peaks/troughs, marked by vertical lines, on these electrodes are within 2 ms (1 sample) of each other. Pulse responses occur every 20 ms (50 Hz pulse train frequency). The artifact amplitude decreases with distance from the stimulation channel.

recording of stimulation pulse trains and ECoG responses. Strong stimulation artifacts at the fundamental frequency and its super-harmonics interfere with ECoG frequencies that underlie motor behavior [25, 26], most notably those in the γ band. Conversely, the band below the fundamental frequency exhibited little or no artifacts. This suggests that increasing the stimulation frequency above 160 Hz (the upper limit of ECoG γ band [32]) could spare the γ band from excessive artifacts in ECoG-based BD-BCI systems. Recent experiments have demonstrated that reliable perception can be elicited in humans with stimulation frequencies as high as 500 Hz [51], so high-frequency stimulation might be a viable artifact mitigation strategy for BD-BCIs. However, such a high stimulation frequency would significantly increase the power consumption. This trade-off must especially be considered for fully implantable BD-BCI, where preserving the battery life may be of critical importance.

2.3.4 Spatial Domain Characteristics

Artifact spatial maps exhibited dipole-like voltage distributions, representative examples of which are shown in Figure 2.5 - 2.8 for each subject. The amplitude of a pulse response recorded by an electrode depended on the position of that electrode with respect to the stimulation channel. Generally, the artifact amplitude scaled inversely with the distance of the electrode to the stimulating channel, which is consistent with Equation (2.4). Furthermore, electrodes lying co-linearly with the stimulation dipole moment experienced stronger artifacts compared to those lying orthogonally. Also, artifact amplitudes increased monotonically with stimulation amplitude, which resulted in the expansion of the saturation region. Correspondingly, the worst-case distance also monotonically increased with stimulation amplitude for these examples. Some exceptions to these behaviors occurred at higher stimulation amplitudes, where the increased current caused a departure from the dipole voltage distribution.

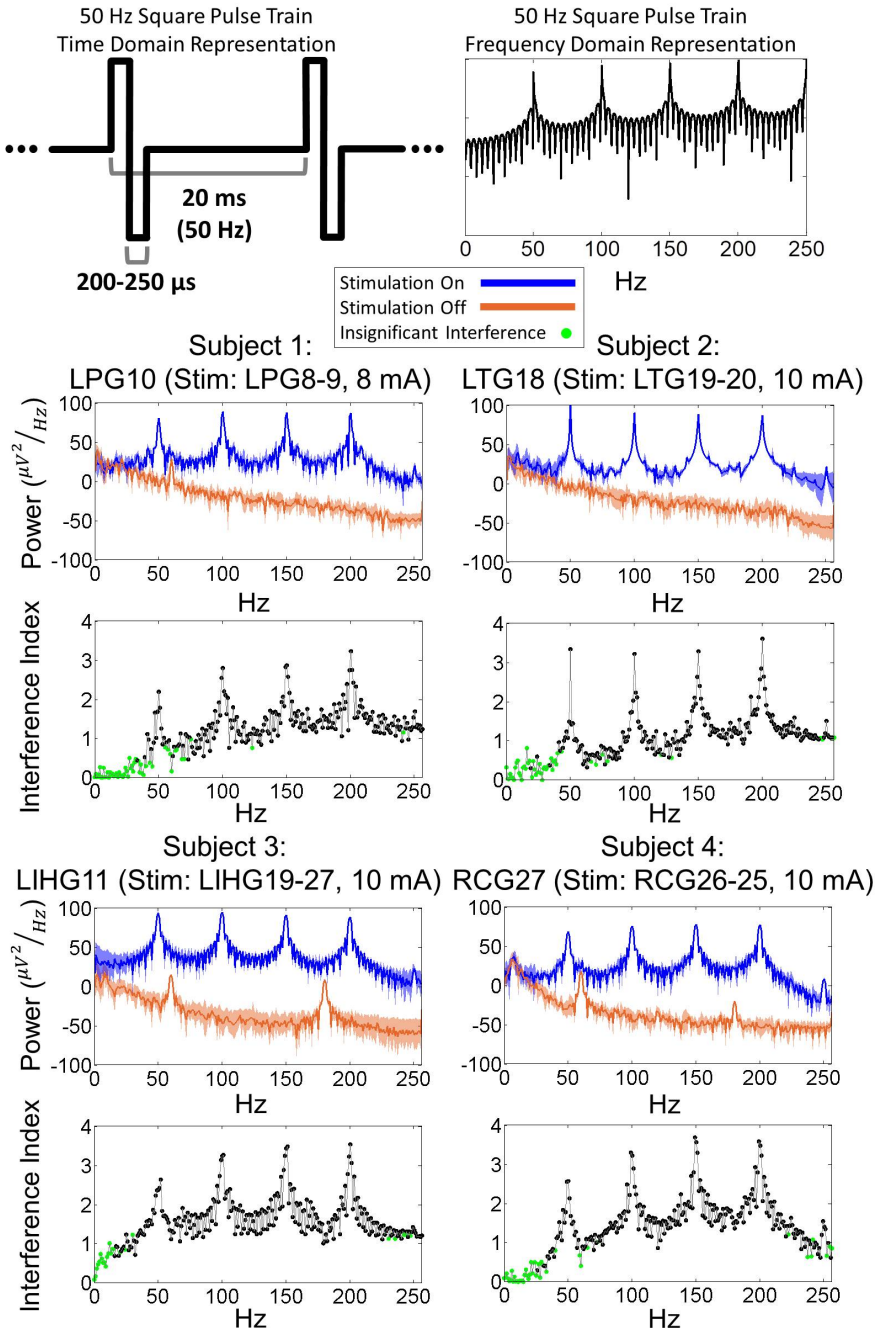

Figure 2.4: (Top)Time domain and frequency domain representations of a 50 Hz square pulse train. (Bottom) Power spectra of ECoG signals during 50 Hz biphasic square pulse stimulation for worst-case electrodes from each subject. The power distribution of ECoG signals, with peaks present at 50, 100, 150, 200 Hz, resembles the power distribution of a 50 Hz square pulse train. Interference index and Kolmogorov-Smirnoff testing (p=0.01) show that a majority of significantly impacted frequencies are above the 50 Hz stimulation pulse frequency.

The ranges of WCDs for each subject over all stimulation channels and amplitudes are reported in Table 2.3. For a comprehensive list of all WCDs across all subjects, stimulation channels, and stimulation amplitudes, the reader is referred to Appendix B. We found the saturation regions to be localized to the vicinity of the stimulation channel, with WCDs ranging from 4.43 to 38.34 mm. Generally, larger WCDs corresponded to larger stimulation amplitudes. The resolution of the WCD is limited by the relatively coarse spatial resolution of ECoG electrodes within a grid. Other factors, such as grid placement and electrode material properties may have also affected the WCD values. Another contributing factor is the location of the stimulation channel within the grid, which may limit the ability for the dipole field to be captured entirely, e.g, stimulation channels placed on the corner or the edge of the grid.

Table 2.2 shows the median and median absolute deviation (MAD) for parameters of the linear regression model and goodness-of-fit values across different stimulation channels for each subject. We chose median-based statistics to counter the effect of a few outliers, primarily contributed by stimulation channels located at the corners of ECoG grids. Despite the differences in implantation site and grid size/type, the median values of $\hat{k}$ remained relatively consistent across subjects and ranged from 2.1 to 3.9 $\Omega\,$mm. Similarly, the median values for $\hat{n}$ were consistent across subjects, and ranged from -78 μV to 70 μV. These values are within the same order of magnitude as ECoG signals [21, 25], which concurs with the fact that $\hat{n}$ is a parameter that accounts for neural activity and background noise. For a comprehensive list of $\hat{k}$ and $\hat{n}$ values across all dipoles and all subjects, the reader is referred to Appendix B.

Table 2.2 also shows that the median values of R-squared ranged across subjects from 0.78 to 0.88. Over all subjects, R-squared values ranged from 0.33 to 0.99, with a median of 0.80 and a median absolute deviation of 0.08 (see Appendix B for full table). This suggests that the dipole model is a good approximation for the propagation of stimulation artifacts

Table 2.2: Median and median absolute deviation (MAD) values for dipole model parameters and R-squared values across subjects. Median and MAD are calculated across all stimulation channels in each representative grid

Regression Parameter	Summary Statistic	Subject 1	Subject 2	Subject 3	Subject 4
$\hat{k}\,(\Omega\,\mathrm{mm})$	Median	3.9	3.3	2.1	3.3
	MAD	1.2	0.3	0.3	0.9
$\hat{n}\,(mV)$	Median	0.070	-0.078	-0.012	0.045
	MAD	0.074	0.080	0.061	0.129
R^2	Median	0.88	0.81	0.78	0.80
	MAD	0.06	0.10	0.04	0.10

Table 2.3: WCD ranges for each subject

Subject No.	Min. WCD (mm)	Max. WCD (mm)	Stim. Range (mA)
Subject 1	12.06	38.34	2–10
Subject 2	12.43	36.45	2–12
Subject 3	4.43	9.12	3–12
Subject 4	5.40	25.89	2–12

in ECoG. R-squared values falling in the lowest 15^{th} percentile ($R^2 < 0.57$) occurred due to violations of the dipole model assumptions. These include "island-like" saturation regions located away from the stimulation site, asymmetrical elongation of the saturation region along the edge of the grid, and abnormally strong artifacts appearing on electrodes adjacent to the stimulation channel.

2.4 Discussion

2.4.1 Time Domain Characteristics

Time-domain analysis revealed the ratcheting effect occurring in all subjects, most prominently at higher stimulation amplitudes (Figure 2.2). This is unsurprising given that strong

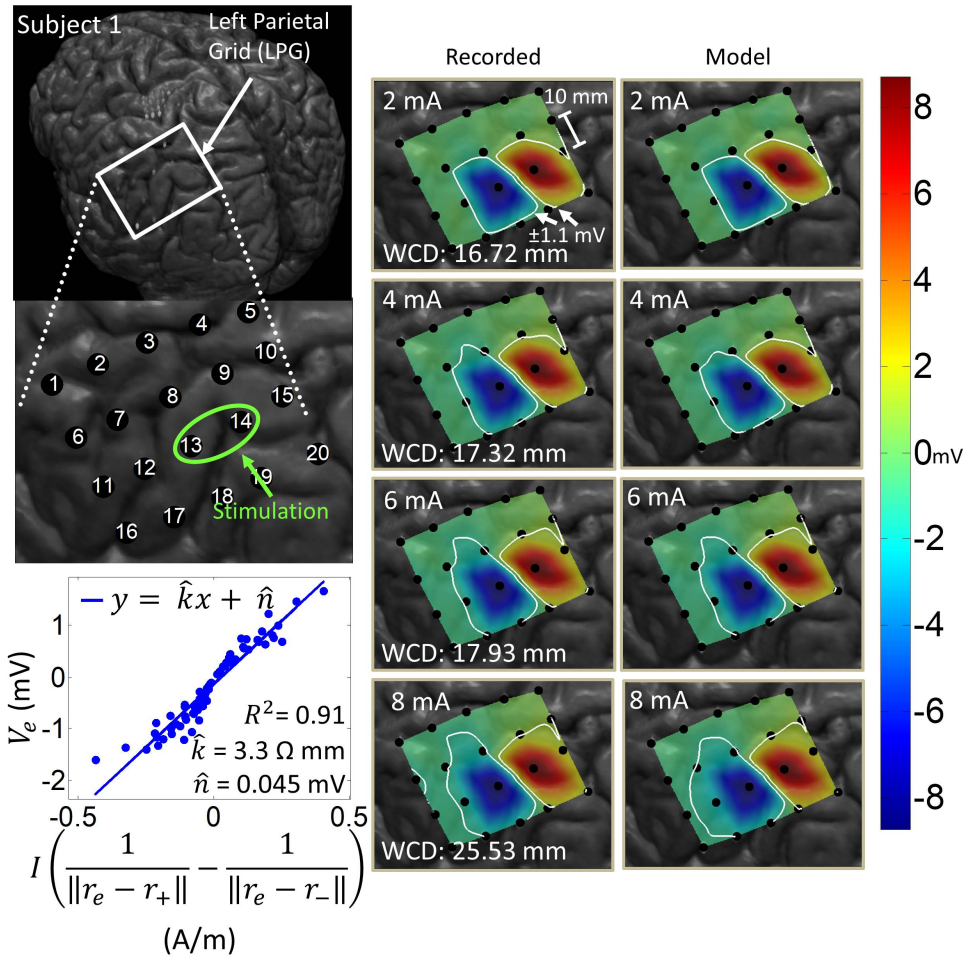

Figure 2.5: Artifact spatial maps based on recorded ECoG data and model predictions for Subject 1. (Top Left) Co-registration image showing the representative grid over the left parietal lobe. (Bottom Left) Regression results aggregating data from stimulation channel LPG13-14 for 2 - 8 mA stimulation amplitudes. Artifact spatial maps were generated using values from the recorded data (Middle) and the dipole model (Right). The worst-case distance (WCD) is the distance from the center of the stimulating channel to the farthest point on the ±1.1 mV contour. Note that the electrodes comprising the stimulation channel (LPG13-14) were saturated on the hospital ECoG recording system and recorded no data. As such these were excluded from the dipole regression and their values were set to ±8.711 mV (the saturation limit of the hospital ECoG recording system) on the artifact spatial maps.

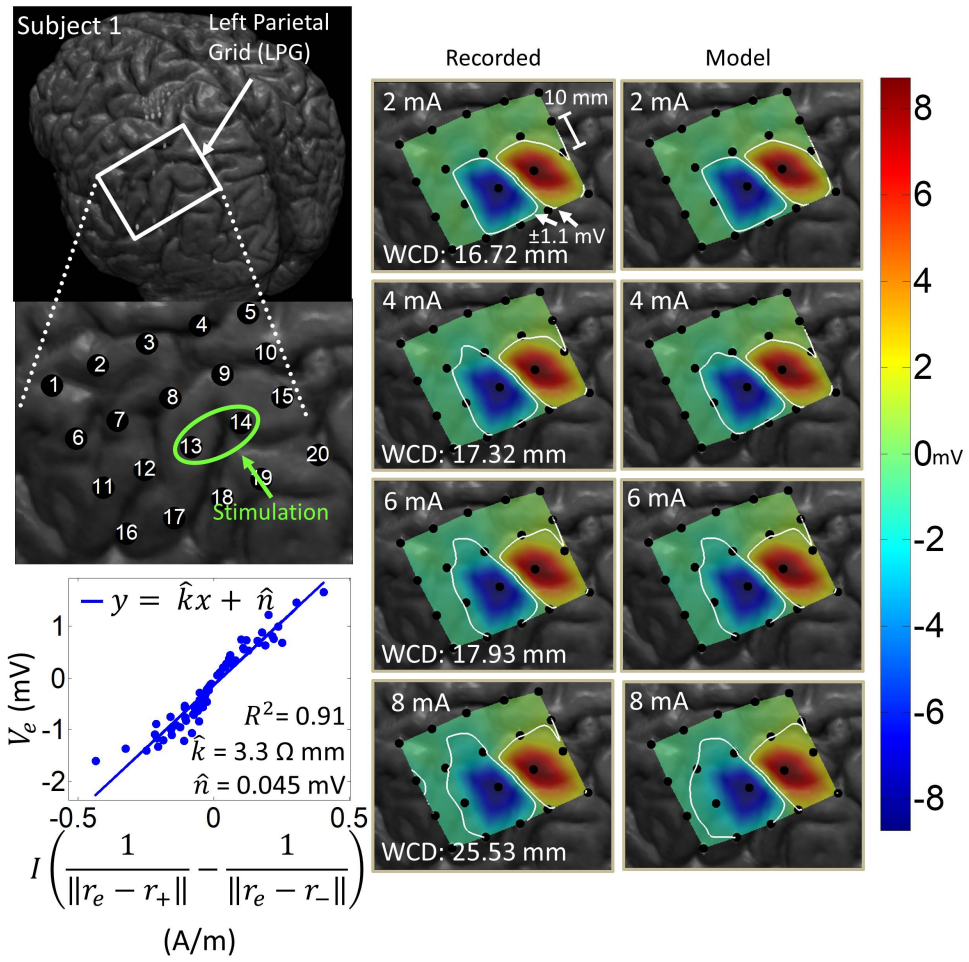

Figure 2.6: Artifact spatial maps for recorded ECoG data and model predictions for subject 2. (Top Left) Co-registration image showing the representative grid over the left temporal lobe. (Bottom Left) Regression uses ECoG data from 2 - 10 mA stimulation amplitudes on the stimulation channel LTG8-9. Artifact spatial maps were generated using values from the recorded data (Middle) the dipole model (Right). Electrodes LTG19 and LTG20 contained no recorded ECoG data, so they are excluded from the analysis (Values on the recorded data map are imputed from electrode LTG18).

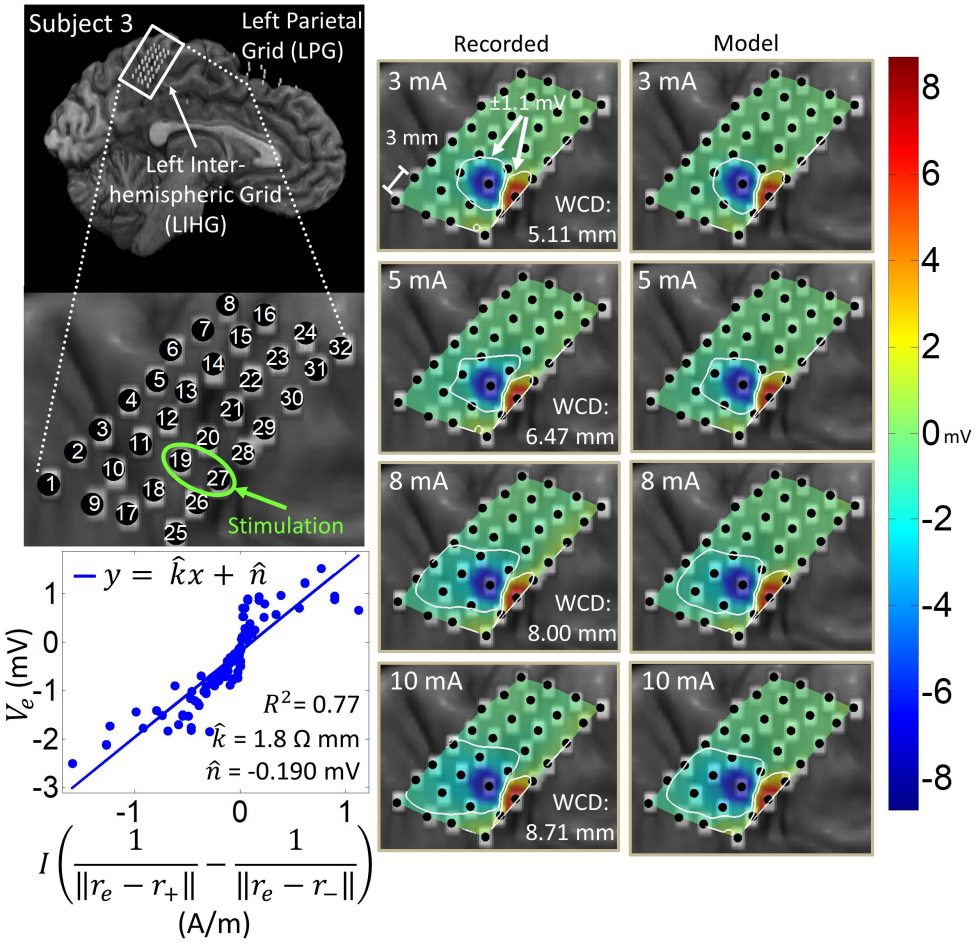

Figure 2.7: Artifact spatial maps for recorded ECoG data and model predictions for subject 3. (Top Left) Co-registration image showing the representative grid located over the leg area on the left side of the interhemispheric fissure. (Bottom Left) Regression results for the stimulation channel LIHG19-27 aggregating data from current amplitudes 3 - 10 mA. Artifact spatial maps were generated using values from the recorded data (Middle) the dipole model (Right).

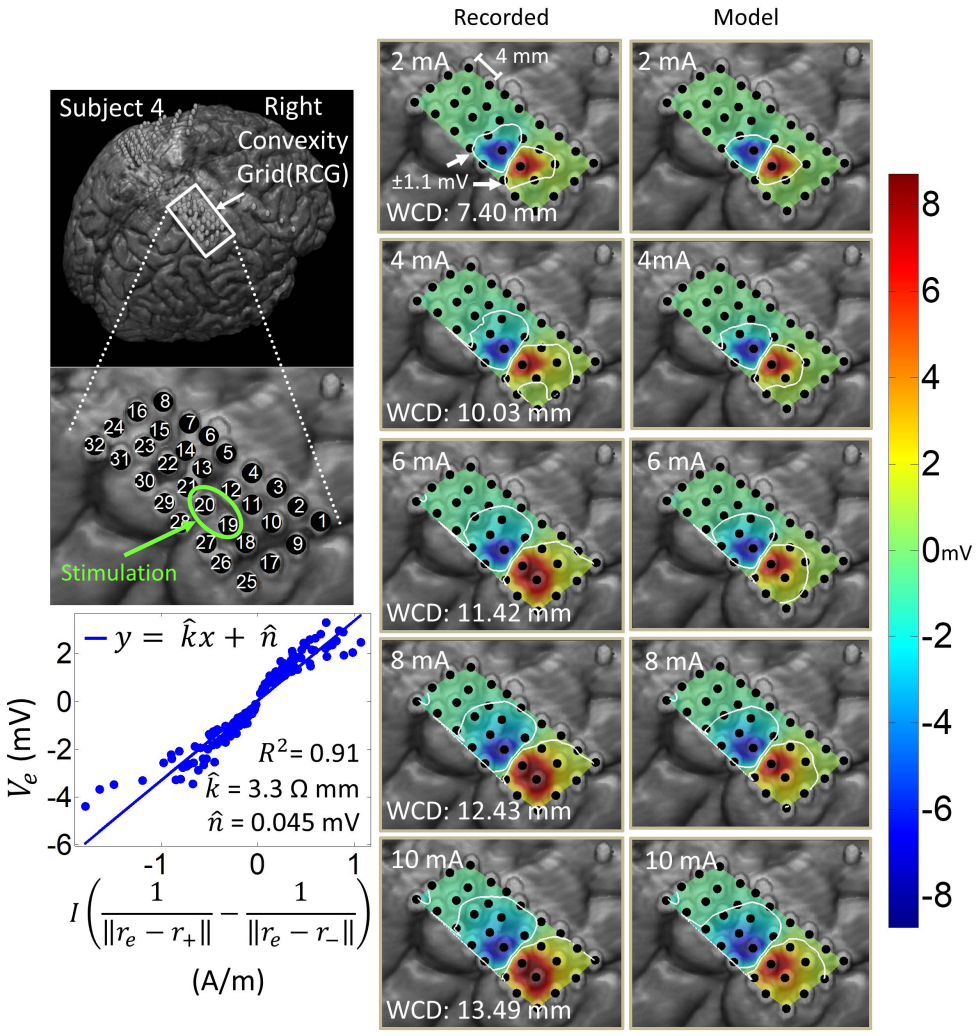

Figure 2.8: Artifact spatial maps for recorded ECoG data and predicted data for subject 4. (Top Left) Co-registration image showing the representative grid located over the right sensorimotor area. (Bottom Left) Regression results for the stimulation channel RCG19-20 aggregating data from current amplitudes 2 - 10 mA. Artifact spatial maps were generated using values from the recorded data (Middle) the dipole model (Right). Electrode RCG18 saturates at 6 mA and above, at which point it is excluded from the analysis as it no longer contains any ECoG data.

stimulation amplitudes are more likely to trigger irreversible Faradaic reactions at the electrode-tissue interface [93]. These reactions generate electrochemical products during the cathodic phase that diffuse away, preventing those products from being reverted during the anodic phase. Therefore, despite the charge-balancing of the biphasic pulses, this unrecoverable loss of charges creates a residual potential. Since stimulation pulses arrive every 20 ms, which is much faster than the tissue discharge time constant (a few seconds, see Figure 2.2), these residual potentials accumulate over the course of a stimulation epoch to generate significant DC voltage shifts. The presence of ratcheting in a clinical, FDA-approved stimulator suggests that BD-BCI systems need to be carefully designed with superior charge-balancing mechanisms [94, 95, 96].

The electrodes most severely affected by artifacts exhibited phase-locking of pulse responses. This is in agreement with the volume conduction assumption expressed by Equation 2.3. It also supports the possibility that ECoG electrodes impose consistent phase shifts whose differences fall below the signal sampling resolution of 512 Hz. To illustrate this, the model of electrode-electrolyte interface can be approximated by a parallel circuit consisting of a double-layer resistance and capacitance, serially connected to an electrolyte resistance [93, 97]. For a typical double-layer capacitance of 10-20 μF/cm^2 [93] and typical resistance values in the 100-200 Ω range [98], we estimate the ECoG electrodes' phase shifts to be in the microsecond range over the ECoG frequency band (0 - 200 Hz). Perturbing these parameters by a factor of 10 did not significantly change these estimates, with the largest phase shifts reaching 0.3 ms. Thus, we conclude that the differences in phase shifts imposed by individual ECoG electrodes likely fall below the sampling resolution of 1.95 ms (1/512 Hz), resulting in the appearance of phase-locked pulse responses.

2.4.2 Frequency Domain Characteristics

The power distribution of stimulation artifacts resembled the theoretical power spectrum of a biphasic pulse train (Figure 2.4). These similarities suggest that the propagation of artifacts from the stimulation channel to the recording electrodes can be approximated by a linear system. The system identification of such a model would require the simultaneous recording of stimulation pulse trains and ECoG responses. Strong stimulation artifacts at the fundamental frequency and its super-harmonics interfere with ECoG frequencies that underlie motor behavior [25, 26], most notably those in the γ band. Conversely, the band below the fundamental frequency exhibited little or no artifacts. This suggests that increasing the stimulation frequency above 160 Hz (the upper limit of ECoG γ band [32]) could spare the γ band from excessive artifacts in ECoG-based BD-BCI systems. Recent experiments have demonstrated that reliable perception can be elicited in humans with stimulation frequencies as high as 500 Hz [51], so high-frequency stimulation might be a viable artifact mitigation strategy for BD-BCIs. However, such a high stimulation frequency would significantly increase the power consumption. This trade-off must especially be considered for fully implantable BD-BCI, where preserving the battery life may be of critical importance.

2.4.3 Spatial Domain Characteristics

The worst-case distance analysis gives a metric for evaluating the saturation risk of stimulation at various current amplitudes. As can be seen from Figure 2.5 - 2.8, at the higher stimulation amplitudes, the saturation region extends to, and possibly beyond, the edges of the ECoG grids. However, studies on artificial somatosensation [51, 52] demonstrated that current amplitudes below 4 mA (and often times as low as 1 mA), delivered by subdurally implanted ECoG grids, were sufficient for eliciting somatosensory perception in human subjects. Saturation is thus only a concern when stimulation and recording electrodes are

immediately adjacent (within 20 mm) and when the recording device has a low saturation tolerance. Optimization of other parameters such as the pulse train frequency and pulse width also permits lower-amplitude stimulation to elicit similar sensations [51].

The current transmission path in cortical electrostimulation depends on a number of factors. Given the complexity of the problem, we adopted a path-agnostic approach by lumping these factors into a single parameter k (see Equation 2.4). Since the units of k are Ωm, we can interpret this parameter as the specific resistance of the path. Furthermore, these paths, as well as the electrode properties [97], may depend non-linearly on the current passing through. However, our approach assumes a single regression model across a range of current amplitudes. Despite these simplifying assumptions, we still achieved a median goodness-of-fit of 0.80 across all subjects and across a wide variety of stimulation scenarios. The departure from this behavior mostly happens for stimulation channels placed on the corners of grids. In these cases, the majority of artifacts lie outside of the grid and cannot be adequately measured. Other examples of non-dipole behavior, such as the formation of "islands" or extensions of the saturation region, are potentially the result of conduction of stimulation current along neural fibers, pockets of cerebrospinal fluid, or neural vasculature. Even in many of these cases, the R-squared value is still around 0.65. Taken together, these results confirm that the spatial variations of stimulation artifacts can be explained with a simple dipole-like model. Dipole models have long been used to describe the propagation of neural signals through neural tissues [74, 75, 76, 77, 78]. However, to our knowledge there have been no other works analyzing the dipole model's applicability to ECoG stimulation artifacts. These models can be used to predict the spatial extent of artifacts and ultimately the size of the saturation region.

2.4.4 Limitations

The main limitation of our work is that the results were derived from artifacts generated and recorded by a clinical ECoG stimulation/acquisition system. To make these results generalizable to BD-BCI systems, we imposed a ±1,100 μV saturation limit based on the specifications of an implantable BD-BCI prototype [55]. Furthermore, our observations may be specific to the type of ECoG grids that were being used by the clinic. However, our analysis still encompasses grids from different manufacturers (AdTech and Integra), different grid sizes (standard and high-density), a variety implantation sites, and multiple subjects. Note that ECoG grids with similar electrode materials (platinum), size and pitch have been successfully used for motor BCI applications [32, 99] as well as artificial sensation studies [51, 52]. The stimulation parameters used for this study also overlap with those used to elicit artificial sensations [52] in the same ECoG grids. Therefore, despite the limitations, the results in this study are likely still applicable to BD-BCI systems.

Chapter 3

Front-End Artifact Suppression: Dipole Cancellation

3.1 Motivation

The first major technical challenge fully implantable BD-BCI must face is the presence of strong artifacts to front-end amplifiers created by cortical stimulation. Specifically, a fully-implantable BCI must operate in an ultra-low-power (ULP) regime, which limits the nominal supply voltage of its analog front-end [55]. If stimulation artifacts reach or exceed this voltage—a likely scenario in bi-directional BCI operation—recording amplifiers will be saturated, thereby leading to unrecoverable loss of data.

To address this problem, we propose an artifact suppression method that is based on auxiliary stimulation applied between the stimulation and recording sites. This secondary stimulation is delivered simultaneously and in opposite polarity to the primary stimulation. Also, it operates at a fraction of the primary stimulation amplitude. We demonstrate the feasibility of this method first in simulations, and then in benchtop experiments with ECoG electrodes

and phantom tissue. Our results indicate that the artifacts can be suppressed below the potential saturation limit of an ULP amplifier array, while operating at only ∼10% of the stimulation voltage and without significant interference with the primary stimulation.

To motivate the development of our method, we observe that the artifact amplitude decays with the distance from a stimulation point. For simplicity, assume that stimulation is delivered at a point $r = 0$ (see Figure 3.1), and that the stimulation voltage is given by: $V_{\text{stim}}(r) = 1/(r + r_0)$, where $r_0 > 0$ is a constant. Note that this model corresponds to a monopolar current source [100] with normalized values of the current amplitude and conductivity. As can be seen, the artifacts exceed a hypothetical saturation threshold, V_{th}, in the assumed recording region. We then introduce a sink at $r = r_c$ with voltage $V_{\text{canc}}(r) = -\alpha/(|r - r_c| + r_0)$, where $\alpha \in [0, 1]$ is a fraction of the original source current. By simultaneously activating stimulation and cancellation, the voltages are superimposed: $V_{\text{total}} = V_{\text{stim}} + V_{\text{canc}}$. Choosing an appropriate α, e.g., $\alpha = 0.15$, renders $V_{\text{total}}(r) < V_{\text{th}}$ over the recording region, thus preventing saturation. At the same time, since $V_{\text{total}}(0) \approx V_{\text{stim}}(0) = V_s$, introducing cancellation does not significantly interfere with stimulation at $r = 0$. This concept, extended to bipolar stimulation, is the basis of our approach.

3.2 Methods

3.2.1 Simulations

Voltage propagation due to bipolar electrical stimulation is more appropriately described with the dipole model:

$$V_s(x, y, t) = \frac{I(t)}{4\pi\sigma}\left[\frac{1}{r_s^+(x, y)} - \frac{1}{r_s^-(x, y)}\right] \tag{3.1}$$

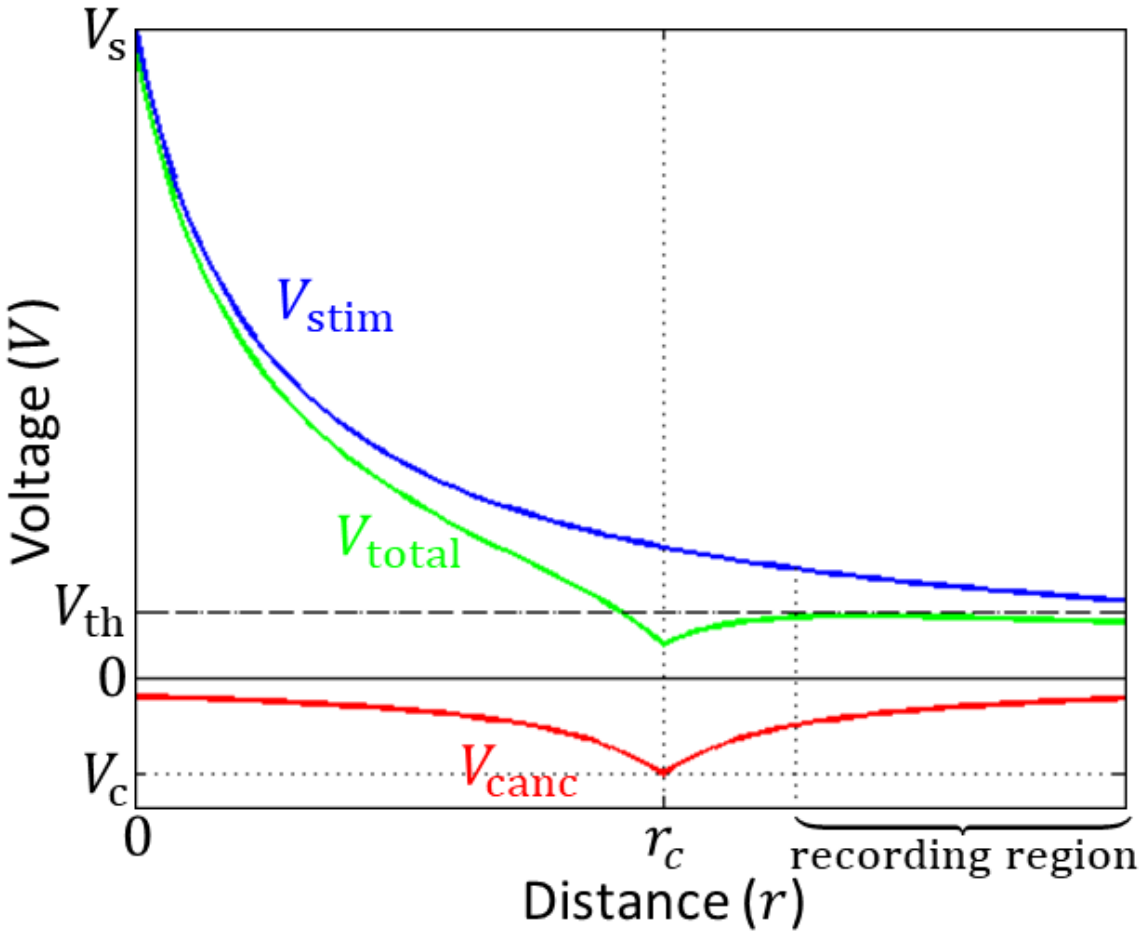

Figure 3.1: The voltage profile V_{stim} (blue) due to monopolar stimulation delivered at $r = 0$. V_{th}–saturation threshold. Recording electrodes are assumed to be on the far right. Canceling (opposite) stimulation at $r = r_c$ with the voltage profile V_{canc} (red). $V_{\text{total}} = V_{\text{stim}} + V_{\text{canc}}$ (green), with $V_c = -0.15\, V_s$.

where $V_s(x, y, t)$ is the voltage at a position (x, y) and time t, I is the stimulation current, σ (S/m) is the bulk tissue conductivity, and $r_s^+$and r_s^- are the distances between the point (x, y) and the dipole source and sink, respectively. Since subdurally implanted ECoG grids are primarily planar, the model(Equation 3.1) is set up in 2D (extension to 3D is straightforward). Also, this model assumes a primarily resistive signal propagation mechanism through an isotropic homogeneous medium. This is in agreement with our recent study [2], which characterized the artifact propagation in the human brain based on clinically recorded ECoG data.

Similar to Equation 3.1, the canceling dipole can be modeled as:

$$V_c(x, y, t) = -\alpha \frac{I(t)}{4\pi\sigma} \left[\frac{1}{r_c^+(x, y)} - \frac{1}{r_c^-(x, y)} \right] \tag{3.2}$$

where, as before, $\alpha \in [0, 1]$, and $r_c^+$and r_c^- are the distances between the point (x, y) and the canceling dipole source and sink, respectively. When cancellation is turned on, the total voltage is obtained by superposition: $V_t(x, y, t) = V_s(x, y, t) + V_c(x, y, t)$. These voltages were then simulated for a typical stimulation-recording ECoG grid configuration.

Since cancellation can potentially interfere with stimulation, we also simulated its effect on the voltage distribution near the stimulating dipole. To quantify the voltage discrepancy due to the presence of cancellation, we calculated $V_t(x, y, t) - V_s(x, y, t)$, which is essentially just $V_c(x, y, t)$. We are especially interested in $V_c(x_s^+, y_s^+, t)$ and $V_c(x_s^-, y_s^-, t)$, where (x_s^+, y_s^+) and (x_s^-, y_s^-) are the locations of the stimulation source and sink, respectively. If these voltages are sufficiently large, they may interfere with the stimulation's ability to cause sensation. We will refer to this phenomenon as desensitization throughout this paper.

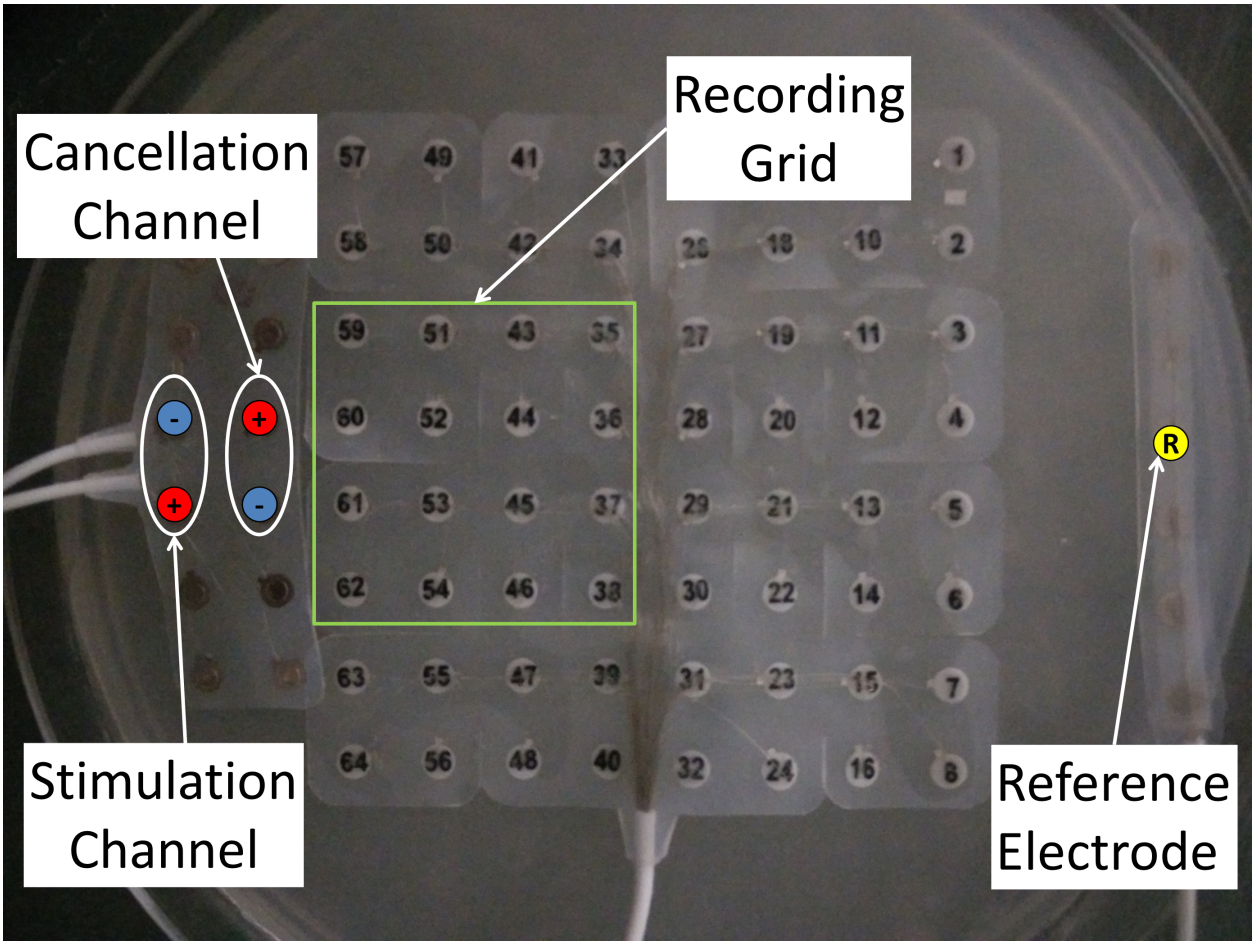

Figure 3.2: ECoG grids placed over phantom tissue in a Petri dish. The primary stimulation channel is located on the 2×6 grid on the pair farthest from the 8×8 recording grid. The cancellation channel is placed between the stimulation channel and the recording grid. The reference electrode is chosen from a 1×6 strip, positioned away from the stimulation channel.

3.2.2 Phantom Tissue Experiments

Food-grade agar (Now Foods, Bloomingdale, IL) was mixed into boiling water to form a gel preparation, which was poured into a Petri dish and an open-ended cylindrical mold. Both were placed in a refrigerator to set overnight. The voltage and current were measured across the gel within the mold, and the conductivity was calculated based on the radius and length of the mold. The conductivity of agar gels is typically manipulated by NaCl doping [101], in order to achieve brain conductivity values. However, the gel used in our study achieved these values without the doping.

ECoG grids (Ad-Tech, Oak Creek, WI) with platinum contacts were placed onto the agar phantom for recording and stimulating purposes (see Figure 3.2). The grids were soaked with deionized water and downward pressure was applied to ensure contact with the gel. Due to a limited number of amplifiers in our recording system, a 4×4 subset of an 8×8 grid was designated as the recording grid. A 2×6 grid was used for stimulation, and electrode pairs were chosen to deliver bipolar stimulation and cancellation as shown in Figure 3.2. A 1×6 ECoG strip was placed on the far end (away from the stimulation channel), and one of its central electrodes was used as the reference. The leads of the recording grid and reference were then connected to an array of bioamplifiers (MP150/EEG100C, Biopac Systems, Inc., Goleta, CA) where signals were amplified (×5,000) and acquired at 4 kHz.

A function generator (33250A, Agilent Technologies, Santa Clara, CA) supplied voltage to the bipolar stimulation channel (Figure 3.2). Cancellation was achieved by connecting a second function generator to the cancellation channel while reversing the polarity. The two function generators were synchronized and programmed to emit a 50-Hz sine wave for 2 s. The stimulation voltage peak-to-peak amplitude was held at 100 mV, while the cancellation voltage was swept from 0 mV to 100 mV in 10-mV increments (0%-100% cancellation). For each cancellation level, ten trials of 2-s stimulation trains were completed, and the signals from 16 ECoG electrodes were recorded and stored.

3.2.3 Analysis

The 2-s stimulation epochs were segmented from the raw data. For each epoch, the individual peaks/troughs were detected for all 16 channels and their median values were calculated across the epoch. For each recording electrode, the overall artifact amplitude was then obtained by calculating the median of these values across 10 trials. This procedure was repeated at each cancellation level, and the values were spatially interpolated, color-coded,

and mapped for analysis.

This analysis was facilitated by defining a hypothetical ULP amplifier saturation region based on an implantable bi-directional BCI prototype [55]. Specifically, given a supply voltage of 2.2 V and a gain of 66 dB, the saturation limit for this amplifier is ± 1100 μV. The effectiveness of our method was then gauged by superimposing the saturation contours onto the artifact spatial distribution maps.

3.2.4 Control Experiments

To investigate whether cancellation has a significant desensitization effect, the stimulation channel was disconnected while the cancellation channel was turned on. Signals were then recorded from the two ECoG electrodes previously used as the stimulation channel. Note that this is equivalent to simulating $V_c(x_s^+, y_s^+, t)$ and $V_c(x_s^-, y_s^-, t)$ in Section 3.2.1. The recording set up was otherwise the same as in the previous experiment. These measurements were performed by sweeping the peak-to-peak cancellation voltage from 10 mV to 100 mV in 10-mV increments, thus mimicking various cancellation levels. The recorded data were then analyzed as in Section 3.2.3, and the desensitization voltages, defined as the total voltage swing across the two electrodes, were calculated. These values were then tabulated and compared to the voltage swings caused by the stimulator. Since it is not possible to measure the voltages directly beneath the stimulating electrodes, these voltage swings, referred to as V_{gel}, were estimated by modeling the electrode-gel interface.

3.3 Results

3.3.1 Simulation Results

Two dimensional voltage fields were simulated as described in Section 3.2.1. To this end, the stimulating and recording ECoG grids were assumed to be adjacent to each other (see Figure 3.3), so as to mimic their respective placement on the sensory and motor cortices. The conductivity $\sigma = 1.7$ S/m was chosen to match the physiological values of human cerebrospinal fluid (CSF) [102]. Note that due to a subdural placement of ECoG electrodes, most of the current will pass through the subarachnoid space, meaning that the bulk conductivity is dominated by that of CSF. Since Equation 3.1 and 3.2 are static models, the current $I(t)$ was assumed constant, and the amplitude $I = 2.1$ mA was chosen. This caused the saturation of 4 channels of the recording grid (Figure 3.3A).

Figure 3.3B shows the effect of cancellation obtained by turning on the canceling dipole (parallel and oppositely polarized to the stimulating dipole), which was able to reshape the saturation contour and move it away from the recording grid, while drawing only 13% of the stimulating dipole current. The value $\alpha = 0.13$ was determined by trial and error to merely demonstrate our method. In a more rigorous approach, the calculation of this parameter could be cast within a constrained optimization framework. Figure 3.3C shows that the choice of the canceling dipole is not unique; in particular, this solution is superior to the previous one since the canceling dipole draws even less current and the saturation contours are farther from the recording grid. The location/orientation of the canceling dipole could also be found through optimization.

Figure 3.3D illustrates the discrepancy between the voltage fields in Figs. 3.3C and 3.3A. The discrepancy at the location of the stimulating dipole is 255 μV—a value significantly below the voltage delivered by the stimulator. Therefore, these small field perturbations in

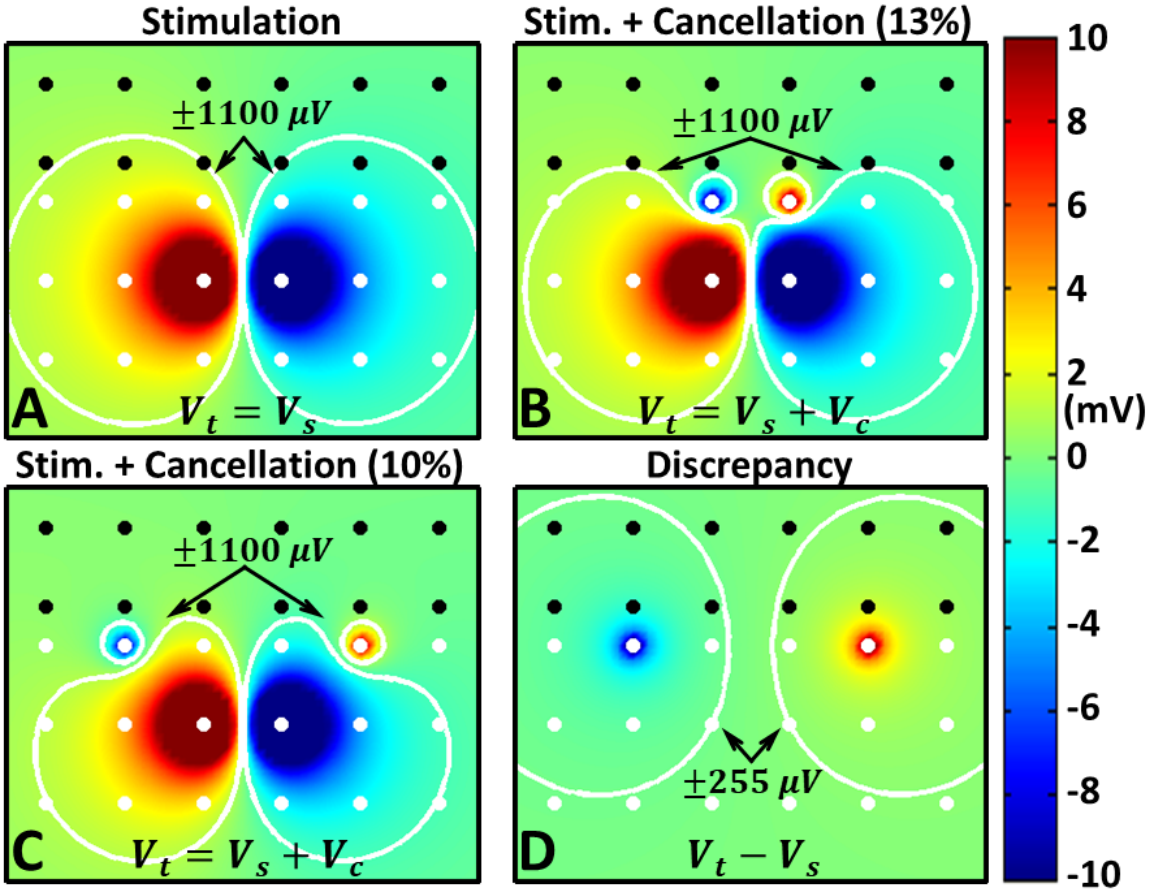

Figure 3.3: Simulation results. A: Spatial distribution of voltage due to the stimulating dipole located in the middle of the stimulating grid (white dots). The electrode pitch is 10 mm. The recording grid (black dots) cannot sense the voltages within the saturation contour. B: The voltage field after turning on the canceling dipole with $\alpha = 0.13$. The saturation contour is reshaped away from the recording grid. C: An alternative location of the canceling dipole ($\alpha = 0.10$). D: The discrepancy between the canceled field (C) and the original field (A). The voltages above 10 mV (below -10 mV) are clipped.

the vicinity of the stimulating dipole are unlikely to cause desensitization.

3.3.2 Experimental Results

By measuring the voltage and current across the mold filled with phantom tissue (see Section 3.2.2), the conductivity of the gel was estimated to be 1.5 S/m, which is consistent with the conductivity of human CSF [101]. Experimentally recorded data were then analyzed as outlined in Section 3.2.3. The 50-Hz stimulation artifacts were clearly visible on all 16 channels, and depending on the electrode location, the phase shifts were either 0° or 180°. Figure 3.4 shows the evolution of the stimulation artifact spatial maps at varying levels of cancellation. At 0% (the cancellation channel off), 3 recording electrodes fall within the saturation region. At 10%, the saturation contour recedes with only a single electrode remaining in the saturation region. When cancellation is at 20%, all the artifact amplitudes are below the saturation level, and they continue to decrease up until 40% cancellation level. From this point, the artifact amplitudes begin to increase, as the canceling channel becomes the dominant source of artifacts due to its proximity to the recording grid. This also leads to the reversal of the field's polarity. Finally, at 100% cancellation level, the saturation contour re-emerges with two channels falling within the saturation region.

The control experiment data were then analyzed as outlined in Section 3.2.4. For each cancellation level from 10% to 100%, the median voltages at the two electrodes corresponding to the stimulation channel were calculated, and the results are shown in Table 3.1. Note that the voltage measured at the electrode corresponding to the stimulator sink, V_c^-, is positive. This is expected behavior, given that this electrode is closer to the source of the cancellation channel (Figure 3.2). Similarly, the voltage V_c^+ is negative. The desensitization voltage, V_d, defined as the voltage swing across these electrodes, ranged from 0.4 mV at 10% cancellation to 3.8 mV at 100% cancellation.

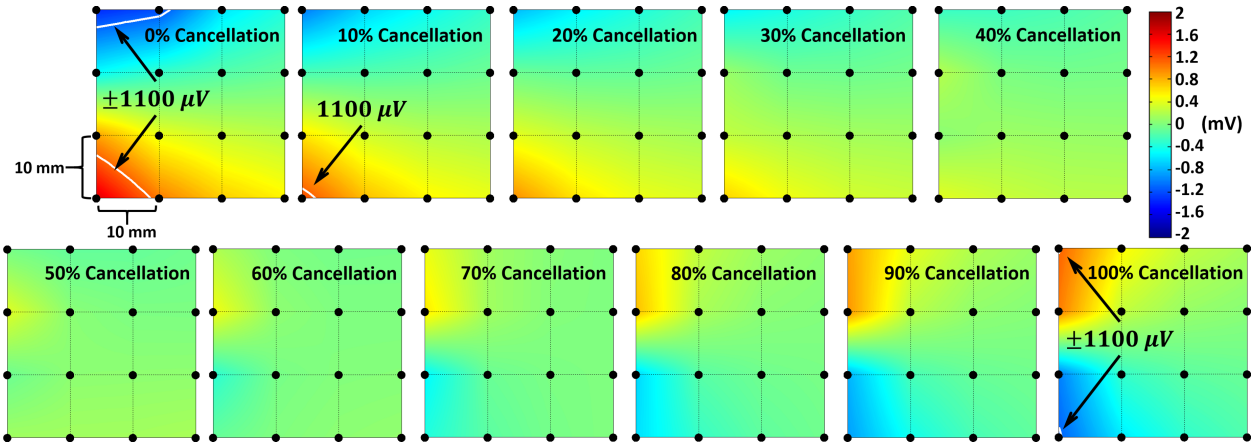

Figure 3.4: Artifact spatial distribution maps for varying levels of cancellation from 0% to 100%. The maps are oriented in the same way as the recording grid in Figure 3.2, with black dots representing individual electrodes. Cancellation levels between 10% and 20% are sufficient to prevent saturation.

Table 3.1: Voltages due to cancellation, V_c^- and V_c^+, measured at the stimulation channel's sink and source, respectively.

Peak-to-peak Cancellation Voltage (mV)	V_c^- (mV)	V_c^+ (mV)	Desensitization Voltage $V_d = V_c^- - V_c^+$ (mV)	$\frac{V_d}{V_{\text{gel}}}$ (%)
10	0.2586	-0.1390	0.3976	1.7
20	0.4562	-0.3477	0.8039	3.4
30	0.6575	-0.5513	1.2088	5.1
40	0.8609	-0.7561	1.6170	6.9
50	1.0623	-0.9571	2.0194	8.6
60	1.2623	-1.1574	2.4197	10.3
70	1.4612	-1.3522	2.8134	11.9
80	1.6590	-1.5486	3.2076	13.6
90	1.8064	-1.7372	3.5436	15.0
100	1.8923	-1.9181	3.8104	16.2

To gauge the likelihood of desensitization, V_d was compared to the stimulation voltage "experienced" by the gel. This voltage, denoted by V_{gel}, could not be directly measured, and had to be estimated. To this end, the electrode-gel interface was modeled as an RC circuit (see Figure 3.5):

$$|V_{\text{gel}}| \triangleq |V_1 - V_2| = \frac{R}{|2\,Z + R|}|V_s| \tag{3.3}$$

where Z is the impedance of the electrode-gel contact, R is the resistance of the gel current path, and $|V_s| = 100$ mV. Based on commonly reported values for ECoG electrodes [103], the total impedance of the path is assumed to be: $|2\,Z + R| = 1000\ \Omega$. The resistance, R, was calculated based on the gel conductivity, σ, the distance between the electrodes (10 mm), and assuming a cylindrical current path with a diameter equal to the depth of the gel (6 mm):

$$R = \frac{L}{\sigma A} = \frac{10 \times 10^{-3}\,\text{m}}{1.5\,\frac{\text{S}}{\text{m}}\,\pi(3 \times 10^{-3}\,\text{m})^2} = 235.8\,\Omega \tag{3.4}$$

After substituting these values into Equation 3.3, we find: $|V_{\text{gel}}| = 23.58$ mV. The ratio V_d/V_{gel} was then calculated (Table 3.1). At cancellation levels between 10% and 20%, which are sufficient to prevent saturation, the desensitization voltage is only a small fraction ($<$ 3.4%) of the gel voltage and is therefore unlikely to interfere with stimulation.

3.4 Discussion

Our simulation and benchtop experiments demonstrate that it is possible to shield recording electrodes from excessive artifact contamination by applying an auxiliary canceling dipole located between the stimulating dipole and the recording grid. Our method essentially amounts to quadrupole stimulation, where the two dipoles are asymmetric, though charge-

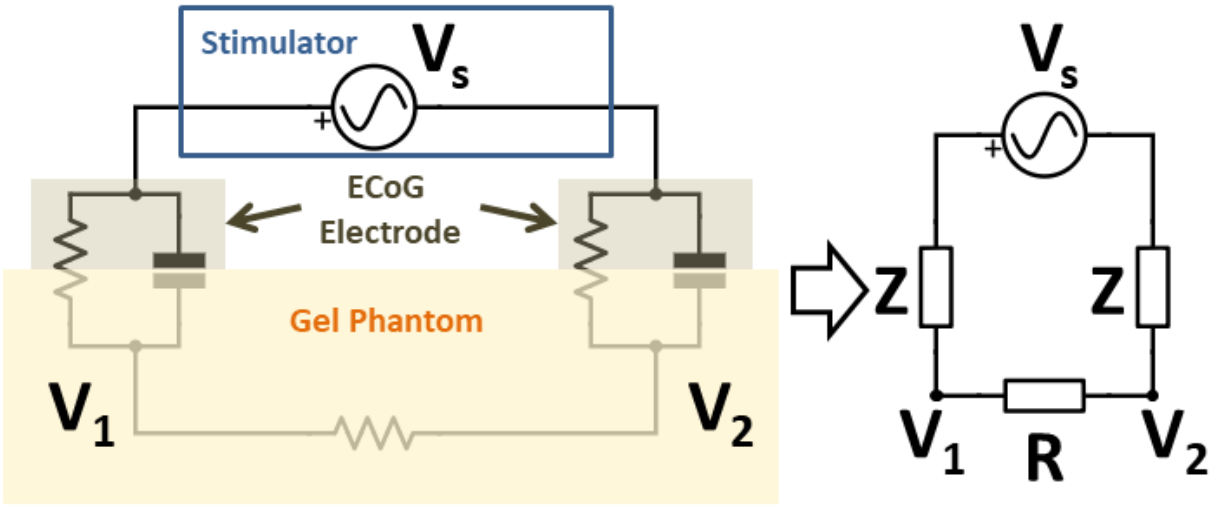

Figure 3.5: Model of the gel-electrode interface [1]. The stimulator is an AC voltage source with an amplitude, V_s. The gel was assumed to be purely resistive with some resistance R. V_{gel} is the voltage across this resistor.

balanced.

Unlike competing artifact suppression methods, e.g. [60], our method's primary objective is not to eliminate stimulation artifacts, but rather to keep them below the saturation limit of a ULP analog front-end. The remaining artifacts can be efficiently removed using a variety of digital signal processing techniques [104].

Our preliminary results indicate that saturation can be prevented by the canceling dipole drawing only ∼10% of the stimulating dipole's current. Therefore, the power overhead of this additional dipole is relatively small. Our analysis also suggests that the canceling dipole does not significantly interfere with the primary stimulation and is therefore unlikely to cause desensitization. In addition, since it operates at a fraction of the stimulation dipole's amplitude, the canceling dipole by itself is unlikely to cause sensation. These claims, however, can only be verified empirically by experimenting with human subjects, and the simple calculations in this study can provide useful guidelines.

While this study is primarily concerned with ECoG electrodes, our method may be applicable to other recording/stimulation modalities, such as microelectrode arrays [44, 53]. The main weakness of our method is that it requires electrodes between the stimulation and recording sites. This concern is substantially mitigated by employing high-density ECoG grids [29].

The canceling dipole amplitude and position were chosen to simply demonstrate and experimentally validate our method. These parameters could be optimized which would result in a greater degree of artifact suppression. Factors such as power consumption and desensitization voltage could be used as constraints in this optimization process. The development of such an optimization framework has been pursued by others in our group, and is described in [59].

Chapter 4

Back-End Artifact Suppression: Pre-whitening and null projection

4.1 Motivation

Even with the implementation of front-end hardware methods, residual artifacts will persist to the back-end and must be additionally suppressed by software-based methods. As mentioned in Section 1.6, many of these techniques fall short of enabling real-time, simultaneous recording and stimulation for BD-BCI. Motivated by these shortcomings, we have developed a technique based on pre-whitening and null projection (PWNP) [105] that efficiently separates artifact and neural subspaces. We achieve this using singular value decomposition, which rank-orders components such that the artifact subspace can be defined as the components with the highest singular values, allowing recorded signals to be projected away from the artifact subspace. In contrast to state-of-the-art ICA, which requires intensive numerical optimization to generate components and a manual combinatorial search to identify the artifact subspace, our technique achieved superior suppression results with a simpler

implementation in a single EEG subject [105].

In this work, we demonstrate the efficacy of the PWNP method in removing cortical electrostimulation artifacts from a variety of neural data. Firstly, we analyzed EEG data collected in the presence of voltage artifacts introduced by a signal generator via electrodes on the scalp. This analysis showed how PWNP is capable of reducing these artifacts, i.e. increasing the signal-to-interference ratio (SIR), while preserving neuromodulation features (signal-to-noise ratio, SNR). Secondly, we also analyzed ECoG data collected during cortical mapping procedures (Phase II epilepsy monitoring) to show that PWNP removes artifacts generated by subdural cortical electrostimulation. Finally, we analyzed data from MEAs collected during sensory stimulation to show how artifacts from sensory stimulation can be removed by PWNP while preserving neural features such as action potentials. Generally, the performance of the PWNP method on these various datasets were superior to those achieved by ICA (the current state-of-the-art), while maintaining a much simpler implementation. Therefore, we demonstrate that the PWNP is an effective technique for the removal of cortical stimulation artifacts with obvious applications to BD-BCI technologies.

4.2 Methods

4.2.1 Electrophysiological Data Collection and Pre-processing Procedures

Brain signals were recorded with the informed consent of all subjects, and all procedures performed were approved by the Institutional Review Board of the University of California, Irvine, the University of Southern California, and the Rancho Los Amigos National Rehabilitation Center. We conducted all research procedures according to the Declaration of Helsinki.

EEG Data Collection

We collected data from two subjects (Subjects 1 and 2) using 20-electrode (10-20 international system), EEG caps (Compumedics USA, Charlotte, NC). We reduced the 30-Hz impedance of the electrode-scalp interface below 10 kΩ by applying conductive gel and abrading the scalp. Nineteen single-channel amplifiers (EEG100C, Biopac Systems, Goleta, CA) captured EEG signals with respect to a reference electrode located over the frontal lobe between Fp1/Fp2 and Fz electrodes. Amplifiers gains were set to 5000$\times$ and band-pass filters were set to 1-35 Hz. These signals were then sampled at 4000 Hz and digitized with a 16-bit acquisition system (MP150, Biopac Systems, Goleta, CA). The acquisition system also simultaneously recorded analog signals generated by a custom MATLAB script (Mathworks, Natick, MA) that tracked the behavioral cues displayed during the experiment.

Prior to placing the EEG caps, two individual EEG electrodes were affixed to the scalp with adhesive cream (EC2, Natus Neurology, Middleton, WI) to the left and right posterior of the Cz electrode. A handheld, battery-powered impedance meter (EIM105, General Devices, Ridgefield, NJ) generated a 30-Hz voltage sine wave, which was then introduced to the scalp via these electrodes in a bipolar configuration. The impedance meter acted as a surrogate for a cortical stimulator, and its output was recorded in parallel by the MP150 system. We first collected baseline activity for one minute without turning on the stimulation. Subsequently, subjects initiated the behavioral task, wherein the stimulator was turned on and subjects followed auditory cues that alternated between "eyes open" and "eyes closed". Each eyes-open or eyes-closed epoch lasted 15 seconds, for a total of 20 epochs (5 minutes total). We then saved the EEG data for later analysis.

ECoG Data Collection

We collected ECoG data at the hospital bedside from two subjects (Subjects 3 and 4) undergoing electrical stimulation as part of epilepsy surgery evaluation. Subject 3 was implanted with a standard size (10 mm spacing, 2.3 mm disc electrode diameter, platinum-iridium contacts) 4×5 ECoG grid (Integra Life Sciences, Plainsboro NJ) over the right temporal lobe. Subject 4 was implanted with the same type of grid over the left frontal cortex (see Figure 4.1). A clinical-grade bioamplifier (Natus® Quantum™, Natus Medical Incorporated, Pleasanton, CA) recorded ECoG signals at a sampling rate of 512 Hz. As part of eloquent cortex mapping procedures, an FDA-approved cortical stimulator (Nicolet® Cortical Stimulator, Natus Medical Incorporated, Pleasanton CA) delivered square pulse trains across a pair of electrodes (stimulation channel). Each pulse train was delivered for a predetermined duration (stimulation epoch) across a range of current amplitudes (2-10 mA). The stimulation parameters used for each subject are listed in Table 4.1. We saved the collected ECoG data for later analysis in MATLAB. Data from the electrodes comprising the stimulation channel were excluded as they saturated during stimulation. All data were high-pass filtered (4^{th} order, Butterworth, 1.5 Hz, zero-phase). We segmented each of the stimulation epochs from the overall data, alongside an equal-length segment of baseline ECoG immediately preceding the stimulation epochs. We analyzed a single representative 10 mA stimulation epoch from each subject, as these amplitudes created the strongest artifacts and thus represent a worst-case scenario for artifact suppression. We then used the segmented baseline and stimulation epochs to compare the performance of the PWNP and ICA artifact suppression algorithms.

Table 4.1: Stimulation Parameters

Parameter	Subject 3	Subject 4
Pulse Frequency	50 Hz	50 Hz
Pulse Width	250 μs	250 μs
Stim. Epoch	5 s	2 s
Current Amplitude	2-10 mA	2-10 mA

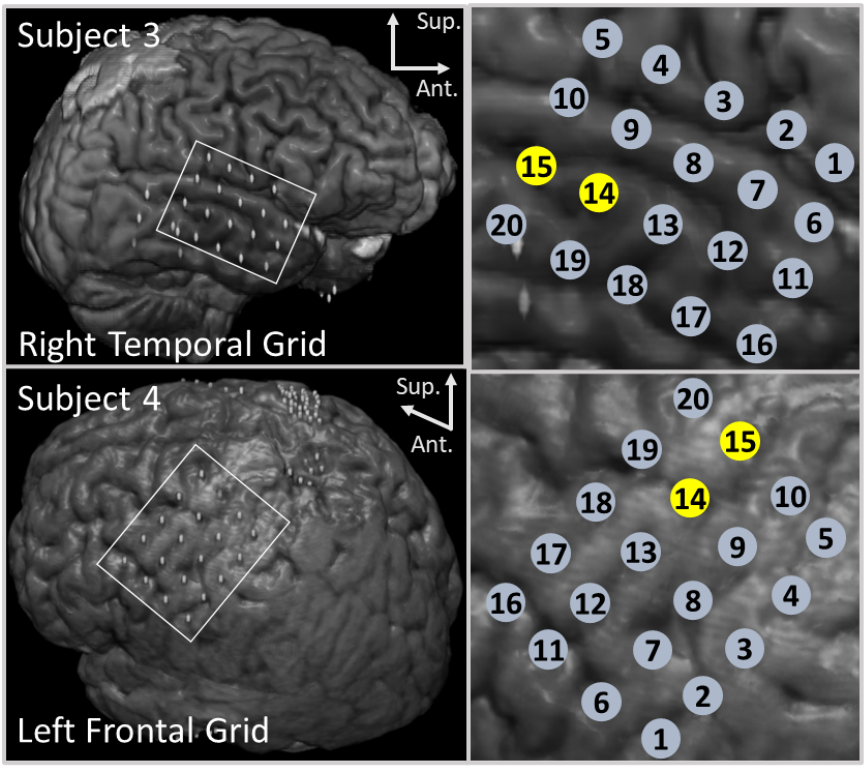

Figure 4.1: MR-CT co-registered images with ECoG grids. Subject 3 and Subject 4 had 4 $\times$ 5 grids implanted in the right temporal area and left frontal area, respectively. Highlighted electrodes mark the bioplar stimulation channels.

MEA Data Collection

MEA data were collected from two 7×7 sputtered iridium oxide film (SPIROF) tipped microelectrode arrays (Blackrock® Microsystems, Salt Lake City UT) implanted in the primary somatosensory cortex (S1) in a single subject (Subject 5). As no imaging data is available for this subject, the approximated location of this array on a brain template is shown in Figure 4.2. Data were collected at a sampling frequency of 30 kHz from a total of 96 channels, as one electrode on each array was designated as the reference/ground (Electrode 49 for MEA1 and Electrode 98 for MEA2). A cortical stimulation device (Blackrock CereStim, Blackrock® Microsystems, Salt Lake City UT) delivered stimulation through a single electrode (Electrode 19). A one-second stimulation epoch consisted of delivering a train cathodic-leading biphasic square pulses at a frequency of 294 Hz, phase width of 200 μs, and a current amplitude of 100 μA. These stimulation epochs were repeated 10 times with an average of 27 seconds in-between. Electrodes that were saturated due to stimulation artifacts exceeding an absolute voltage amplitude of 8192 μV (mostly occurring on MEA1, see Figure 4.2) were excluded from analysis as they contained no useful neural data, leaving 54 non-saturated channels across both arrays. Similarly to the ECoG data, we segmented stimulation epochs from the overall data. We then high-passed ($\geq$0.1 Hz) and linearly detrended these stimulation epochs and subsequently appended them into one 10-second epoch. We also segmented a 10-second of data occurring between two consecutive stimulation epochs and designated these data as the baseline epoch. These baseline and stimulation epochs were saved for later analysis.

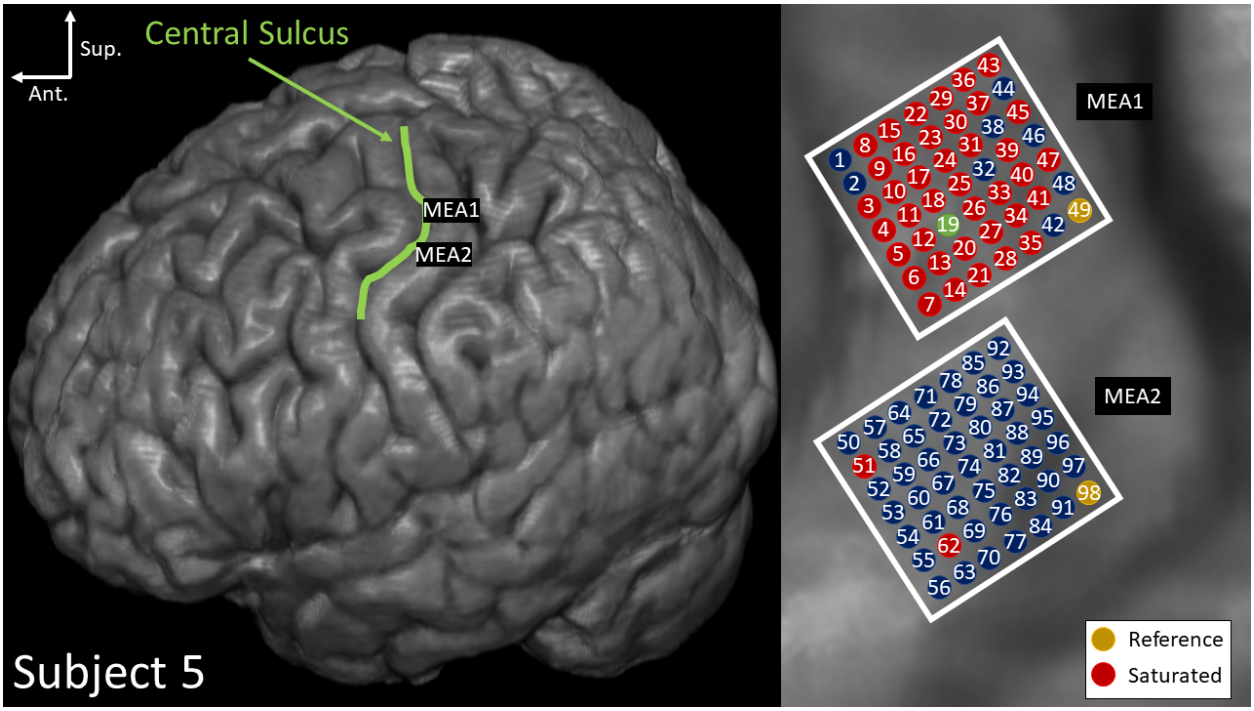

Figure 4.2: Approximate locations of the two MEAs superimposed on an MRI brain template. Two 7 x 7 MEAs were implanted over S1. Stimulation was applied to electrode 19 on MEA1 (electrodes 1 - 49). Saturated electrodes are marked in red. Electrodes 49 and 98 were used as reference for their respective MEAs.

4.2.2 Artifact Suppression Procedures

Pre-whitening and Null Projection (PWNP) Algorithm

The PWNP algorithm is fully described in [105], and its theoretical basis can be found in [106]. The algorithm exploits the fact that artifacts are typically much stronger than neural activity, and thus reside in a low-dimensional subspace, corresponding to the highest singular values of the data matrix. This allows the artifact subspace to be readily identified, so the data can be projected to its orthogonal complement through null projection. The resulting data will then reside in an artifact-free subspace. The pre-whitening step serves to remove spatial correlations between electrodes, which improves the SNR of the neural signal. Mathematically these steps can be expressed as:

$$\mathbf{X}_S^{\text{clean}} = \mathbf{\Sigma}_B^{\frac{1}{2}}\mathbf{H}\mathbf{H}^{\mathrm{T}}\left[\mathbf{\Sigma}_B^{-\frac{1}{2}}(\mathbf{X}_S - \mu_S\mathbf{1}^{\mathrm{T}})\right] + \mu_S\mathbf{1}^{\mathrm{T}} \tag{4.1}$$

$\mathbf{X}_S \in \mathbb{R}^{n\times t_S}$ represents the original, artifact-laden, stimulation data containing n channels and t_S time points. Correspondingly, $\mathbf{X}_S^{\text{clean}} \in \mathbb{R}^{n\times t_S}$ represents the stimulation data after it has been "cleaned" by the PWNP method. $\mu_S \in \mathbb{R}^{n\times 1}$ is the time average of $\mathbf{X}_S$ and $\mathbf{1}$ is a column vector of ones such that subtracting $\mu_S\mathbf{1}$ de-means $\mathbf{X}_S$. The pre-whitening process is then completed by multiplying the de-meaned data by the pre-whitening matrix $\mathbf{\Sigma}_B^{-\frac{1}{2}} \in \mathbb{R}^{n\times n}$, which is calculated using the baseline data (see [105]). The columns of the null-projection matrix, $\mathbf{H} \in \mathbb{R}^{n\times(n-d)}$, are the pre-whitened data's left singular vectors that correspond to its lowest $n - d$ singular values, where d is the dimension of the artifact subspace. The artifact subspace dimension is equivalent to the number of singular values σ that satisfy the criterion $\sigma > \alpha\sqrt{t_S - 1}$ ($\alpha > 1$). This is modified from the original criterion $\sigma \approx \sqrt{t_S - 1}$ to account for signal noise [105]. The pre-whitened data are then null-projected (pre-multiplied by $\mathbf{H}^{\mathrm{T}}$), reconstructed (pre-multiplied by $\mathbf{H}$), and re-colored (pre-multiplied by $\mathbf{\Sigma}_B^{\frac{1}{2}}$). Finally the mean, μ_S, is added back to the data.

To determine the optimal value of the threshold multiplier α for each neural data set, we used the following procedure. First, the average power $\bar{P}$ was calculated for each channel as:

$$\bar{P} = \frac{1}{n_f} \int_{f_1}^{f_2} PSD(f)\, \mathrm{d}f \tag{4.2}$$

where $PSD(f)$ is the power spectral density, $[f_1, f_2]$ is the relevant frequency range, and n_f is the number of frequency points in that range. For the narrow-band, 30 Hz, EEG stimulation, we used the frequency range of $[f_1, f_2] = [29, 31]$ Hz. For the broad-spectrum ECoG/MEA stimulation response, we used a frequency range of $[f_1, f_2] = [0, f_s/2]$, where f_s is the sampling frequency. We then calculated $\bar{P}$ for both stimulation (P_s) and baseline (P_b) data and identified a worst-case electrode as the electrode with the largest average power difference ($P_s - P_b$). We subsequently varied $\alpha = [1, \alpha_{max}]$, where $\alpha = 1$ is the theoretical optimum and α_{max} is a conveniently chosen value at which the artifact subspace collapses into an empty set ($d = 0$). For each value of α within this range, we removed the artifacts from the worst-case electrode according to Equation 4.1, and calculated its average power P_α^{clean}. We then find the optimal value $\hat{\alpha}$ by:

$$\hat{\alpha} = \arg\min_{\alpha} |P_\alpha^{\text{clean}} - P_{\text{b}}|, \qquad \alpha \in [1, \alpha_{max}] \tag{4.3}$$

Note that this procedure takes advantage of the fact that the power difference between the baseline and stimulation data is largely due to the presence of artifacts. Therefore, upon cleaning, we expect that $P_{\hat{\alpha}}^{\text{clean}}$ approaches P_{b}.

ICA Artifact Suppression Procedure

To benchmark the artifact suppression performance of the PWNP method, we compared it against an ICA-based back-projection method. We used the FastICA toolbox in MATLAB [107] to generate independent components (ICs) for the EEG, ECoG, and MEA data. Unlike the PWNP method, in which the artifact subspace is readily identifiable due to rank-sorting of components, the ICA method necessitates a combinatorial search to identify the optimal artifact subspace. Given the number of channels we had in EEG, ECoG and MEA, it was not practical to perform a full combinatorial search. Instead, we used the following heuristic approach. Converged ICs were inspected in the time and frequency domains to identify components containing artifact features (e.g. patterns occurring at the pulse train frequency, power peaks occurring at pulse train frequency and super-harmonics [2, 5]). After the components comprising the artifact subspace were identified and nulled, the cleaned data were obtained via the back-projection method [108]. This procedure was repeated by nulling various combinations of artifact components until we achieved the best suppression result, defined as the minimum average power difference between ICA-cleaned and baseline states on the worst-case electrode.

4.2.3 Artifact Suppression Evaluation Analyses

EEG Artifact Suppression Evaluation

Using the procedures for PWNP (Section 4.2.2) and ICA (Section 4.2.2), we cleaned the stimulation EEG data of Subjects 1 and 2. Subsequently, we calculated the change in SNR and SIR due to artifact suppression for both PWNP and ICA methods in order to compare their performances. Due to the eyes open/closed task, we expect to observe modulation in the α band (8 – 12 Hz) [109]. To quantify this modulation, we introduced a SNR-like

metric, which compares the separability of the eyes-open/eyes-closed states. Specifically, we calculated SNR as a deflection coefficient [110]:

$$\mathrm{SNR}(f) = 10\log\sqrt{\frac{(\mu_c(f)-\mu_o(f))^2}{0.5(\sigma_c^2(f)+\sigma_o^2(f))}}, f \in [8,12]Hz \tag{4.4}$$

where $\mu_c(f)$ and $\mu_o(f)$ represent the average power in the α band over eyes-closed and eyes-open epochs, respectively. Correspondingly, $\sigma_c^2(f)$ and $\sigma_o^2(f)$ are the eyes-closed and eyes-open power variances in the α band. The overall SNR was then calculated as the average of SNR(f) over the α band.

To further compare suppression performances, we also introduced a metric to represent the SIR. This metric allowed us to evaluate the degree of stimulation interference in comparison to the amount of occipital α band modulation. We calculated the SIR as the ratio of the maximum average power in the α band to the maximum average power in the interference band, which we chose to be 29 - 31 Hz to capture the narrow-band, 30 Hz, sine stimulation (Equation 4.5). We used the maximum power for eyes-closed segments when the occipital α waves were present.

$$\mathrm{SIR} = 10\log\frac{\max\limits_{8\le f\le 12}\mu_c(f)}{\max\limits_{29\le f\le 31}\mu_c(f)} \tag{4.5}$$

For each channel, we calculated the SNR and SIR before suppression and after application of either the PWNP or ICA method. We then characterized the suppression performance of each method by calculating ΔSNR and ΔSIR, respectively defined as the change in SNR and SIR due to artifact suppression.

We expect that successful artifact suppression would increase the SIR ($\Delta\mathrm{SIR} > 0$) while not decreasing SNR ($\Delta\mathrm{SNR} \geq 0$). We subsequently used a paired signed rank test to confirm whether SIR values across electrodes were significantly different before and after applying

either suppression method. The same test was also used to assess whether the ΔSIR values across electrodes were significantly different between the two suppression methods. Finally, to visualize and compare the suppression results spatially, the ΔSIR values were color-coded and overlaid on a topographical EEG map.

ECoG and MEA Artifact Suppression Evaluation

ECoG and MEA stimulation data were cleaned using the PWNP and ICA methods described in Section 4.2.2 and 4.2.2, respectively. Unlike those in the EEG protocol, the subjects in the ECoG and MEA protocols did not perform any behavioral tasks, therefore an SNR could not be defined as was done with the EEG data. Instead, we evaluated the artifact suppression performance by comparing the PSD of cleaned data to that of the baseline. This approach is consistent with our previous assertion that most of the power differences between stimulation and baseline data are due to artifacts (see Section 4.2.2). For example, significant spectral differences between cleaned and baseline data, especially at the stimulation frequency and its super-harmonics, would indicate inadequate suppression. Conversely, more aggressive suppression could potentially remove neural features in addition to artifacts, resulting in "over-cleaning". To control for this outcome, we performed a baseline control experiment where we applied both artifact suppression method to the baseline epoch. Since baseline data contains no artifacts, we expect the baseline epoch to remain relatively unaffected by this procedure. To visualize potential distortions due to either method of artifact suppression, we compared the baseline epoch before and after cleaning in the time and frequency domains. We quantified the distortion in the time domain by calculating the root-mean-squared error (RMSE):

$$RMSE = \sqrt{\frac{1}{n}\sum_{i=1}^{n}(b_i - c_i)^2} \tag{4.6}$$

where n is the number of samples in the baseline epoch time series, b is original baseline data and c is the same data after suppression. These RMSE values were then color-coded and mapped to images of the ECoG/MEA grids to spatially visualize the effect of cleaning over multiple electrodes. Additionally, time domain data for a representative channel was shown before and after the PWNP/ICA cleaning procedures. We then visualized the effects of the cleaning procedures in the frequency domain by plotting average PSDs of baseline and cleaned epochs. A paired signed rank test was then performed to determine whether the power distributions were significantly different across frequencies.

We then examined the neural time series for the stimulation, PWNP-cleaned, ICA-cleaned and baseline conditions in order to assess the signal quality after artifact suppression. We next examined the aforementioned conditions in the frequency domain by calculating the PSD. We accomplished this by splitting the epoch for each condition (stimulation, PWNP-cleaned, ICA-cleaned, baseline) into 10 equal-length subsections, and then performing the fast Fourier transform on each section to obtain their PSDs. The average and standard deviation of these PSDs were then calculated over the sections. We subsequently plotted the PSDs for each condition for the worst-case electrode, defined as in Section 4.2.2. This allowed us to observe the frequency domain features introduced to the baseline PSD by the stimulation. Additionally, these PSDs allowed us to assess the reduction of artifact features by both suppression methods.

Unlike EEG artifacts, which had a narrowband frequency response, ECoG and MEA artifacts had a broadband power distribution. As such, the SIR defined by Equation 4.5 could not be used, so we introduced a separate SIR-like metric to quantify the artifact suppression performance. As was described in Section 4.2.2, we expect the power distribution of cleaned data to approach that of the baseline. To quantify the separation between power distributions, we calculated a variant of the deflection coefficient [86], which we refer to as the interference index. Note that this is a general metric that is capable of accounting for

overlapping means and unequal variances [87]. For two power distributions a and b, the interference index at frequency f is defined as:

$$I(f) = \frac{1}{2} \log \frac{\sigma_{\mathrm{t}}^2(f)}{\sigma_{\mathrm{a}}(f)\sigma_{\mathrm{b}}(f)} \tag{4.7}$$

where $\sigma_{\mathrm{a}}(f)$ and $\sigma_{\mathrm{b}}(f)$ are the standard deviations of PSDs for two conditions. Since the PSD sample sizes for each condition are equal ($n = 10$, see previous paragraph), the total standard deviation, $\sigma_{\mathrm{t}}(f)$, can be expressed as:

$$\sigma_{\mathrm{t}}^2(f) = \frac{\sigma_{\mathrm{a}}^2(f) + \sigma_{\mathrm{b}}^2(f)}{2} + \frac{\left[\mu_{\mathrm{a}}(f) - \mu_{\mathrm{t}}(f)\right]^2}{2} + \frac{\left[\mu_{\mathrm{b}}(f) - \mu_{\mathrm{t}}(f)\right]^2}{2} \tag{4.8}$$

where $\mu_{\mathrm{a}}(f)$ and $\mu_{\mathrm{b}}(f)$ are the means of the two PSDs and $\mu_{\mathrm{t}}(f) = \frac{1}{2}(\mu_{\mathrm{a}}(f) + \mu_{\mathrm{b}}(f))$ is the total mean. We first calculated the interference index between stimulation and baseline conditions to serve as a positive control (a = stimulation, b = baseline). Subsequently, we calculated the interference index between the cleaned and baseline conditions (a = cleaned, b = baseline) to evaluate the effectiveness of each artifact suppression method. Note that smaller artifact interference will result in a lower value of $I(f)$ (inverse to SIR). Ideally, in the case where there are no artifacts, the interference index will approach zero ($\sigma_{\mathrm{a}}(f) = \sigma_{\mathrm{b}}(f)$ and $\mu_{\mathrm{a}}(f) = \mu_{\mathrm{b}}(f)$). We then plotted the interference indices for the stimulation, PWNP-cleaned, and ICA-cleaned conditions for the worst-case electrode.

We further qualified each interference index by performing a rank-sum test to identify frequencies with power distributions different than those of the baseline condition. These significant interference frequencies were then marked on the interference index plots. We expect the superior suppression method to result in fewer significant interference frequencies.

As a positive control, we also calculated the number of significant interference frequencies in the stimulation data.

We additionally characterized the suppression results by calculating the interference indices for all electrodes in the grid between different conditions for each ECoG/MEA electrode. Specifically, we first calculated the interference index between the stimulation and baseline conditions as a positive control. Subsequently, we calculated the interference indices between the cleaned and baseline conditions to quantify the residual artifact for both artifact suppression methods. To verify whether the stimulation data was improved, we compare the interference indices across electrodes using a paired signed rank test. Subsequently, we compare between PWNP-cleaned and ICA-cleaned interference indices using the same test. To visualize the distribution of residual artifacts, we spatially interpolated, color-coded, and mapped the interference indices onto MR-CT co-registered images. For Subjects 3 and 4, we used pre-implantation MR images and post-implantation CT images to co-register ECoG grids onto a 3D brain rendering. We followed the same co-registration process outlined in [5]. For Subject 5, brain images were not available. Instead, the location of the MEA was estimated based on photographs of the implantation location taken during surgery and aligned to a template brain using anatomical landmarks.

Finally, in the absence of a behavioral task in the MEA protocol, we wanted to evaluate the ability of both artifact suppression methods to retain action potentials in the MEA data. Specifically, we identified an electrode exhibiting action potentials during the baseline condition. We then counted the number of action potentials occurring during the stimulation epochs for that electrode. After artifact suppression, we calculated the percent of retained action potentials for both the PWNP-cleaned and ICA-cleaned data.

4.3 Results

4.3.1 EEG Artifact Suppression Results

Artifact suppression results for EEG data showed that both methods successfully attenuated the artifacts, as evidenced by SIR improvements, while preserving the SNR. Using the PWNP method, we estimated the dimension of the artifact subspace to be four ($d = 4$, $\hat{\alpha} = 2.9$) for Subject 1 and $d = 7$ ($\hat{\alpha} = 1.2$) for Subject 2. For the ICA method, 3 of 19 converged components were identified as artifact components for Subject 1, and 3 of 15 were identified for Subject 2. The components comprising the artifact subspace in PWNP and the artifact components in ICA all contained significant power at the stimulation frequency (30 Hz). Figure 4.3 shows the change in the SNR (Equation 4.4) and SIR (Equation 4.5) after applying each artifact suppression technique. As expected, both methods resulted in SIR improvements that were statistically significant (a paired, right-tailed, signed rank test; Subject 1, p = 0.00007 for both methods; Subject 2, p = 0.00007 for both methods). Comparing between methods, the ΔSIR was greater for the PWNP method than for ICA method for both subjects. For example, for Subject 1, the best channel (C3) exhibited a ΔSIR of 47.2 dB for PWNP compared to 41.1 dB for ICA (see Table 4.2). This table also shows the summary statistics for ΔSIR and ΔSNR across all 19 channels for both subjects. Comparing the median ΔSIR values between suppression methods, PWNP outperformed ICA by 7.04 dB in Subject 1 and 10.84 dB in Subject 2. Furthermore, these performance improvements were statistically significant for both subjects (paired, right-tailed, signed rank test; Subject 1, p = 0.00201; Subject 2, p = 0.0016). The spatial distribution of ΔSIR (Figure 4.4) further highlights these results. Additionally, PWNP appeared to be the most effective on those electrodes closest to the stimulation channel, which were the most severely affected by artifacts. In comparison to the SIR changes, SNR changes were generally small (<1 dB). Statistical analysis showed that the SNR improvement after PWNP was statistically signif-

Table 4.2: Change in SIR and SNR after suppressing artifacts in EEG data for Subjects 1 and 2. The maximum ΔSIR and ΔSNR correspond to the electrodes that exhibited the largest SIR and SNR change upon artifact suppression. The median ΔSIR and ΔSNR are also reported with the median absolute deviation (MAD).

	Subject 1		Subject 2	
(dB)	PWNP	ICA	PWNP	ICA
max(ΔSIR)	47.20	41.10	43.08	35.20
max(ΔSNR)	4.41	3.51	5.13	7.75
median(ΔSIR)	34.22±9.02	27.18±8.34	31.79±7.85	20.95±7.04
median(ΔSNR)	0.18±1.02	0.59±0.84	-0.03±1.49	0.34±1.91

icant for Subject 1 (paired, right-tailed, signed rank test; p = 0.00258), but not for Subject 2 (p = 0.14312). For ICA, both subjects had statistically significant improvement in SNR (Subject 1, p = 0.00530; Subject 2, p = 0.00136). Note that SNR improvements are not the primary objective of artifact suppression.

4.3.2 ECoG Artifact Suppression Results

Like with EEG data, both methods were able to remove artifacts in the ECoG stimulation data. For the PWNP algorithm, we estimated the artifact dimension to be $d = 12$ ($\hat{\alpha} = 1.1$) for Subject 3 and $d = 11$ ($\hat{\alpha} = 1.1$) for Subject 4. For the ICA procedure, 10 of 18 components were identified as artifact components for Subject 3, while 11 of 15 were identified for Subject 4. The components comprising the artifact subspace in PWNP and the artifact components in ICA were nulled as explained in Sections 4.2.2 and 4.2.2, respectively.

ECoG signals exhibited prominent artifacts during stimulation. Figure 4.5A shows a representative segment of a stimulation epoch to illustrate this phenomenon. Despite their broadband nature, these artifacts were substantially reduced by both PWNP and ICA methods, examples of which are shown in Figure 4.5B and C, respectively. Generally, the signal amplitudes upon cleaning were more similar to those of baseline data (Figure 4.5D).

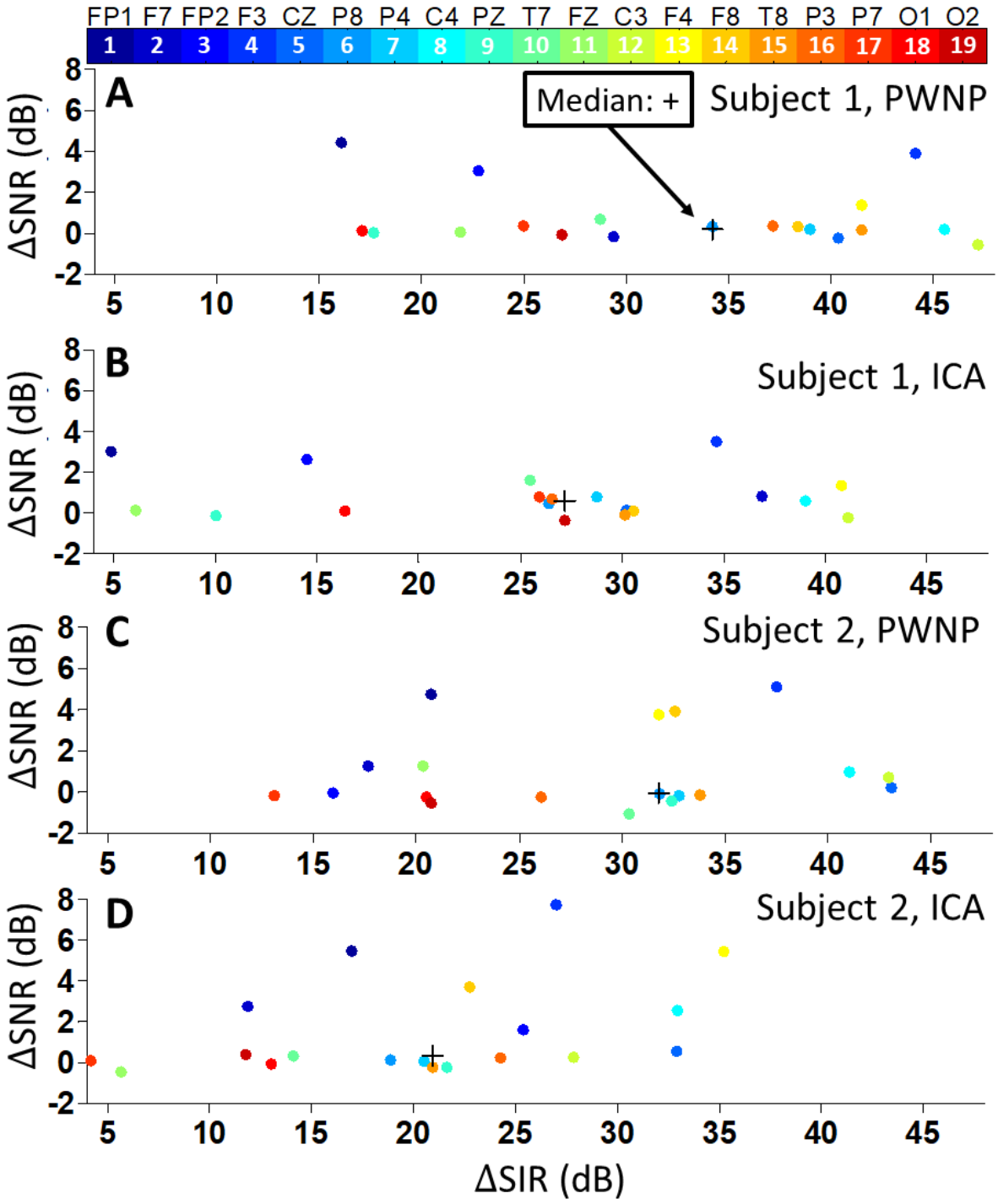

Figure 4.3: Plots of the change in SIR and SNR values upon applying PWNP/ICA artifact suppression techniques for the EEG data for Subjects 1 and 2. Each color corresponds to a different EEG channel. The median (ΔSIR,ΔSNR) point across electrodes is indicated on each plot by a "+". The SIR improved significantly for both subjects, with the PWNP method outperforming the ICA method. Both methods preserved the SNR, as evidenced by median $\Delta\text{SNR}\approx 0$. A numerical summary of these results is provided in Table 4.2.

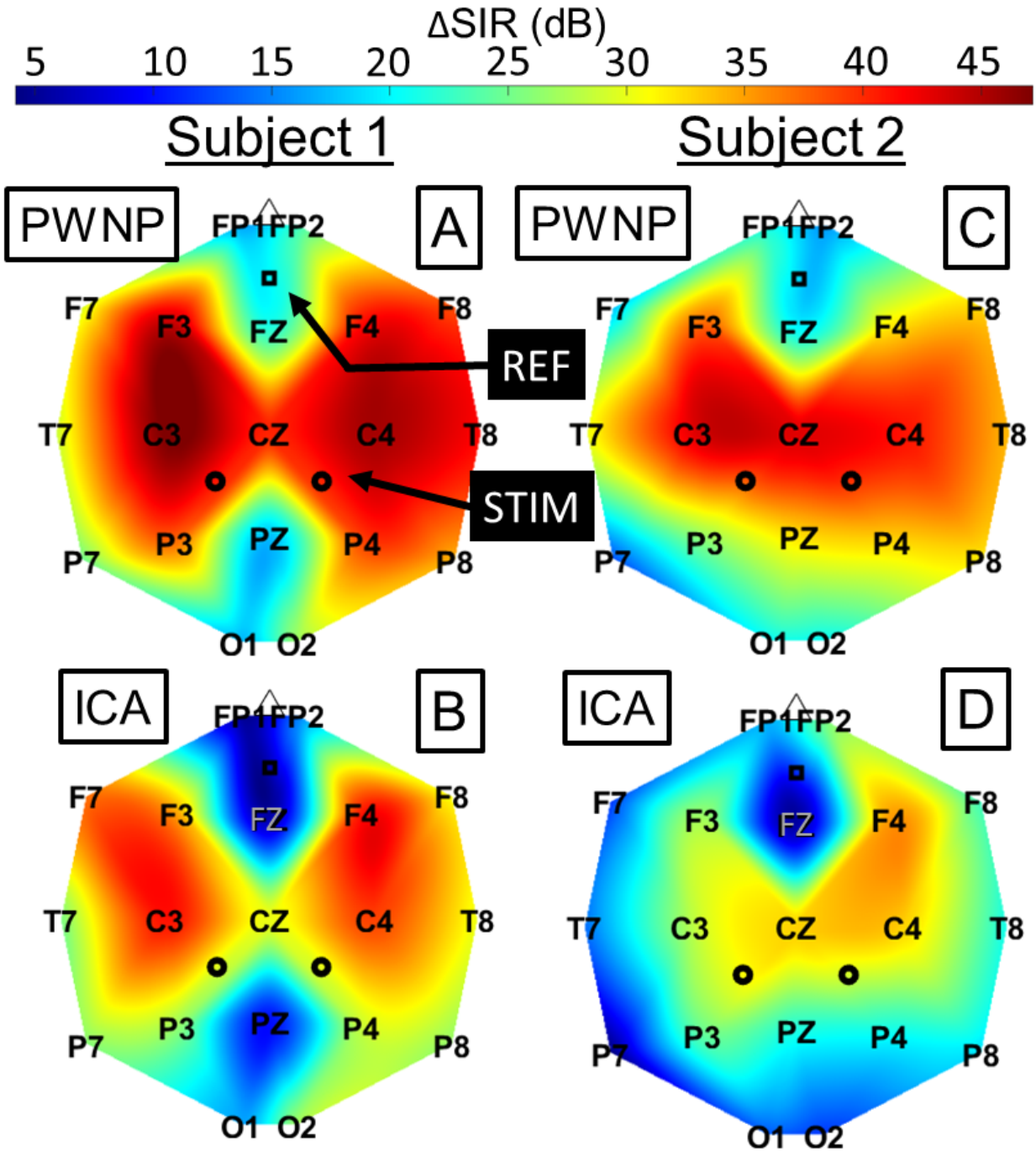

Figure 4.4: Maps of ΔSIR for both subjects for the PWNP-cleaned (A,C) and ICA-cleaned (B,D) data. Black square (reference electrode), black circles (stimulation electrodes). PWNP outperforms ICA for both subjects, with the most substantial suppression occurring on the most contaminated channels (C3, Cz, C4). Hot/cold spots away from electrodes are spatial interpolation artifacts due to sparse electrode coverage.

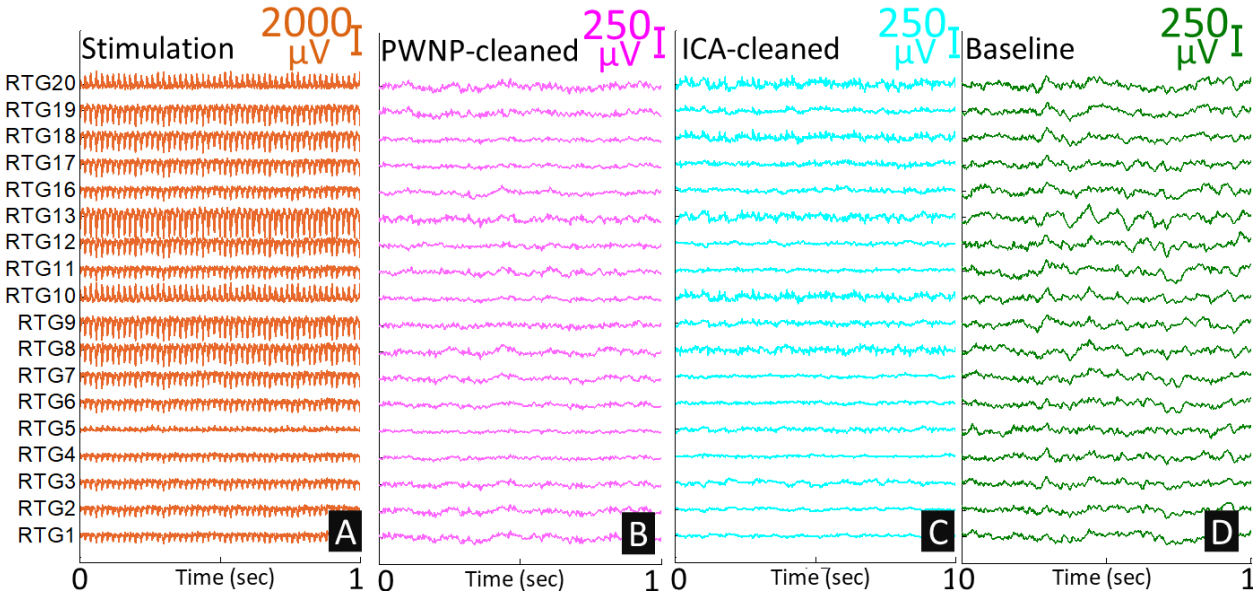

Figure 4.5: Representative ECoG time series from 18 channels of the right temporal grid (RTG) of Subject 3 (see Figure 4.1). The stimulation channel (RTG14-15) is omitted due to saturation. (A) One-second segment from the stimulation epoch. (B) Same segment after PWNP artifact suppression. (C) Same segment after ICA artifact suppression. (D) One-second segment from a baseline epoch occurring immediately before the stimulation epoch. Note that the stimulation data is shown at an eighth of the scale of the others.

To illustrate the effectiveness of artifact suppression in the frequency domain, Figure 4.6 shows example PSDs before and after cleaning from the worst-case electrodes. Unsurprisingly, these were the electrodes closest to the stimulation channel that were co-linear with the moment of the stimulation dipole [2, 5]. In comparison to the baseline data, stimulation PSDs exhibited peaks at the stimulation frequency (50 Hz) and its superharmonics, as well as a broadband increase. Upon artifact suppression, these artifact features were largely reduced and the PSDs were brought closer to the baseline. Furthermore, the PSDs of PWNP-cleaned data were generally closer to the baseline in comparison to their ICA counterparts.

The interference index of the stimulation data exhibited peak values at the stimulation frequency (50 Hz) and its super-harmonics, similarly to stimulation data PSDs. Figure 4.7 illustrates this effect for the worst-case electrode. These peaks were largely removed after artifact suppression, with the PWNP method outperforming ICA. This was evidenced by PWNP achieving lower interference index values compared to ICA. Summary statistics for

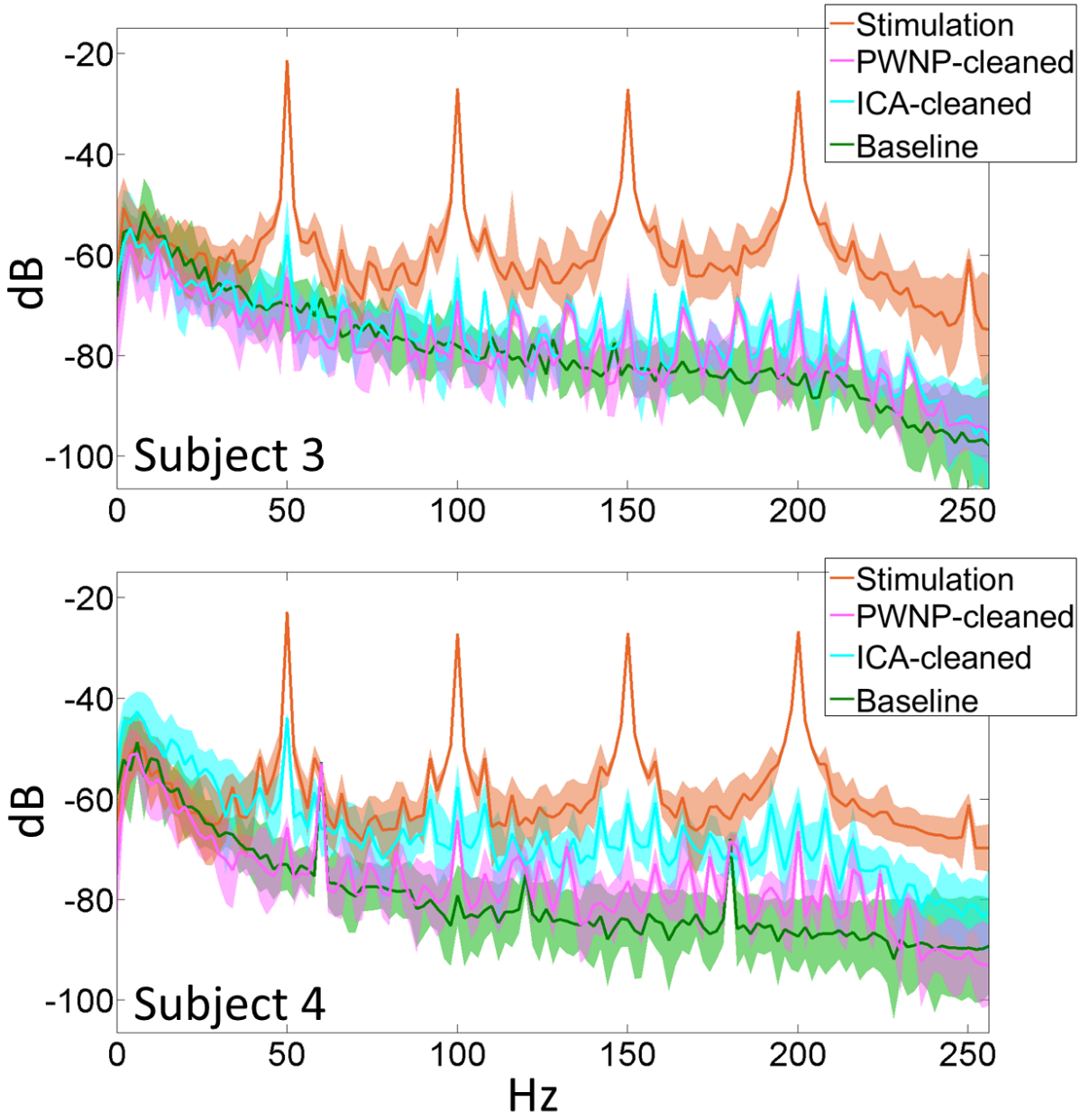

Figure 4.6: PSDs of ECoG signals under four different conditions from a worst-case electrode from both subjects (RTG13 for Subject 3 and LFG13 for Subject 4, cf. Figure 4.1). Solid lines represent the PSD averages taken over 10 subsections and shades represent corresponding one standard deviation bounds.

Table 4.3: Frequency-averaged interference indices, $\bar{I}$, (see Equation 2.1) and corresponding standard deviation, σ_I, for stimulation, PWNP-cleaned and ICA-cleaned conditions for worst-case electrode in ECoG data.

	Subject 3			Subject 4		
	Stim.	PWNP	ICA	Stim.	PWNP	ICA
$\bar{I}$	0.399	0.089	0.108	0.403	0.080	0.199
σ_I	0.318	0.102	0.140	0.320	0.100	0.121

these results are given in Table 4.3. Moreover, PWNP-cleaned data had fewer frequencies with significant residual interference compared to ICA-cleaned data (rank-sum test $p<0.01$).

To demonstrate the effectiveness of artifact suppression methods beyond the worst-case electrode, we spatially mapped the interference indices (Figure 4.8). As expected, the map corresponding to the stimulation data exhibited the highest values, especially in the vicinity of the stimulation channel. Both artifact suppression methods effectively reduced the interference indices across electrodes. Specifically, the interference indices upon PWNP suppression became significantly smaller (paired, left-tailed, signed rank test: Subject 3, $p = 4.8 \times 10^{-5}$; Subject 4, $p = 1.1 \times 10^{-4}$). Similar behavior was observed after ICA suppression as well (Subject 3, $p = 4.8 \times 10^{-5}$; Subject 4, $p = 1.1 \times 10^{-4}$). Consistent with our worst-case electrode analyses, we observed that PWNP generally outperformed ICA, particularly on the electrodes closest to the stimulation channel. Specifically, the PWNP method yielded lower interference indices across electrodes (paired, left-tailed signed rank test; Subject 3: $p=0.010495$; Subject 4: $p=0.000994$).

Figure 4.9 shows the results for the baseline control experiment. Since baseline data contained no artifacts, we expect artifact suppression methods to yield small RMSE values between baseline and artifact-suppressed baseline data. For PWNP, the average RMSE value across electrodes was 15.3 ± 2.3 μV, which accounted for only 6% of the pre-cleaning baseline voltage swing (256 μV). In contrast, much larger RMSE values were obtained with the ICA method (68.8 ± 27.4 μV), suggesting that it imposed more significant signal distor-

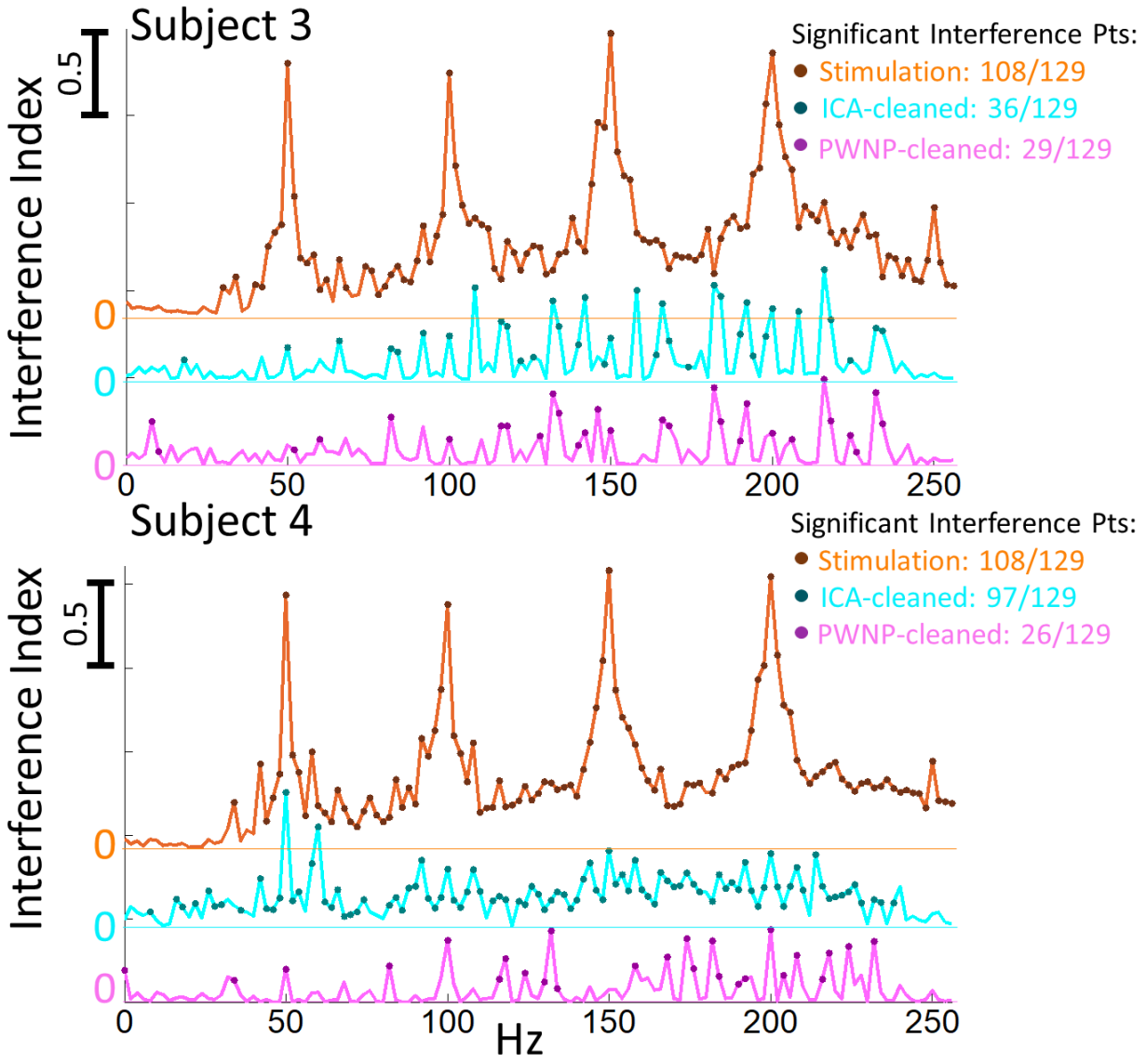

Figure 4.7: Interference indices calculated for worst-case electrodes from both subjects. Filled-circle markers indicate frequencies with significant interference, as determined by rank-sum test ($p<0.01$). The PWNP method achieved superior suppression results, as it generally resulted in lower interference indices, as well as fewer frequencies with significant residual interference.

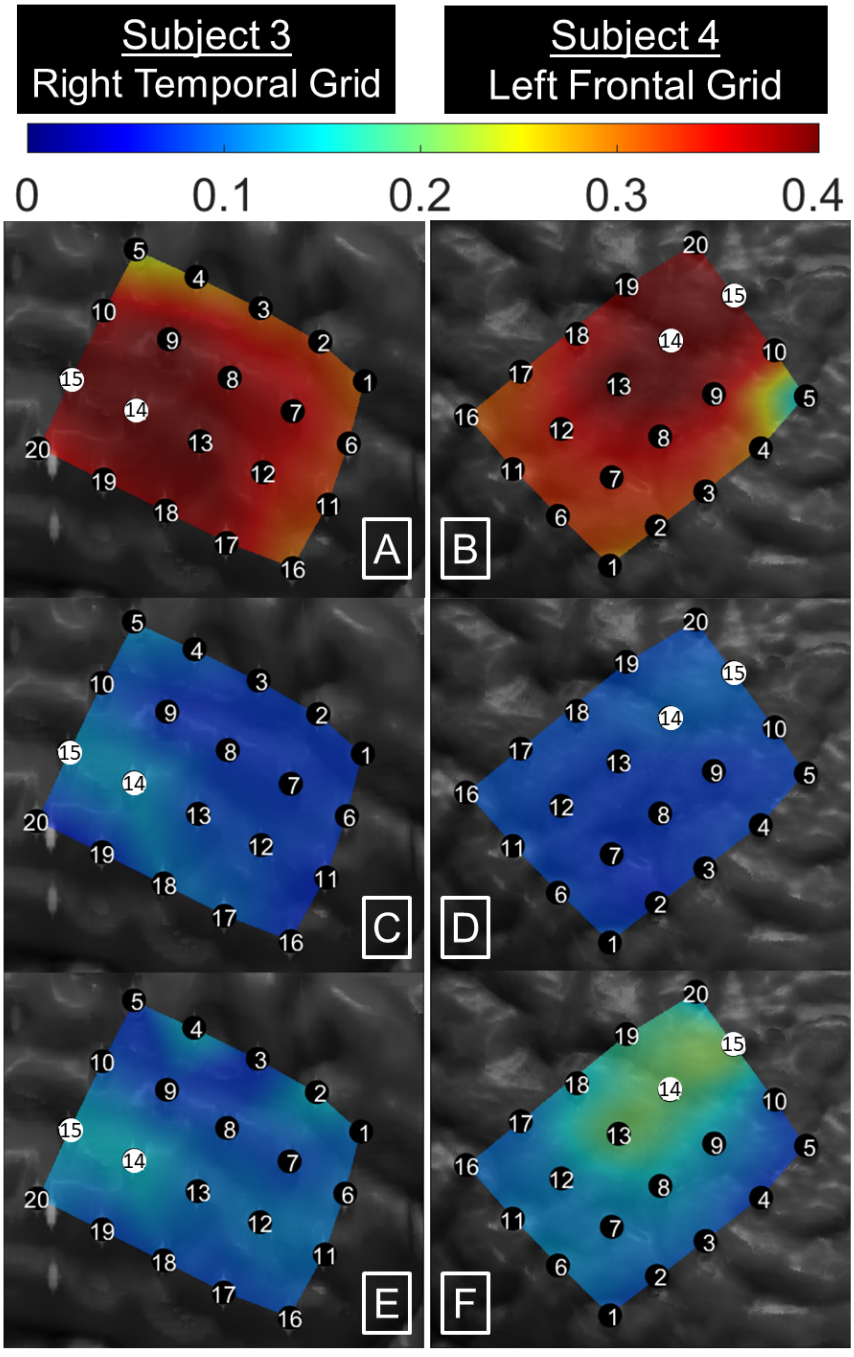

Figure 4.8: Frequency-averaged interference indices (Equation 2.1) were spatially interpolated, color-coded and mapped to cortical surfaces. For the saturated stimulation electrodes (white), the values were imputed to the highest value in the map to preserve the continuity of the interpolation. (A,B) Interference indices for stimulation data. (C,D) Interference indices for PWNP-cleaned data. (E,F) Interference indices for ICA-cleaned data. Note that the stimulation electrodes were saturated, so their value was imputed to the highest in the grid to preserve interpolation continuity.

tions. To visualize these distortions, Figure 4.9 also shows time domain baseline signals for a representative electrode before and after artifact suppression. We selected the representative electrode as the electrode exhibiting the RMSE closest to the median RMSE across the grid. As evidenced by these examples, the PWNP method introduced much less distortion in the time domain compared to the ICA method. We additionally characterized these post-suppression baseline distortions in the frequency domain. Comparing the PSDs before and after artifact suppression (signed rank test, $p<0.01$), we identified no frequencies exhibiting significantly different power distributions after PWNP artifact suppression, while 6 frequencies were identified for ICA. The PWNP method may have benefited over the ICA method from the fact that the baseline data epoch in this control experiment had been used to calculate the pre-whitening matrix, $\mathbf{\Sigma}_B^{-\frac{1}{2}}$, (see Equation 4.1). To rule this out, we performed control experiments on additional baseline epochs (C), while retaining the same PWNP and ICA parameters.

4.3.3 MEA Data Artifact Suppression Results

Artifact suppression evaluation for the MEA data yielded similar results as for ECoG data, with the PWNP method generally demonstrating superior suppression results. After excluding saturated electrodes (artifact amplitudes exceeding 8.7 mV) from both MEAs, we used data from the remaining 54 channels (cf. Figure 4.2) to train the PWNP and ICA algorithms. For the PWNP method, we estimated the artifact subspace dimension to be $d = 33$ ($\hat{\alpha} = 1.2$). For the ICA method, we identified 49 independent components as artifacts (out of 54 converged components). The artifact subspace in PWNP and the artifact components in ICA were nulled as explained in Sections 4.2.2 and 4.2.2, respectively. Since most of the electrodes on MEA1 were saturated, we focus on results from MEA2.

Figure 4.10 shows a representative segment of the stimulation data from the worst-case

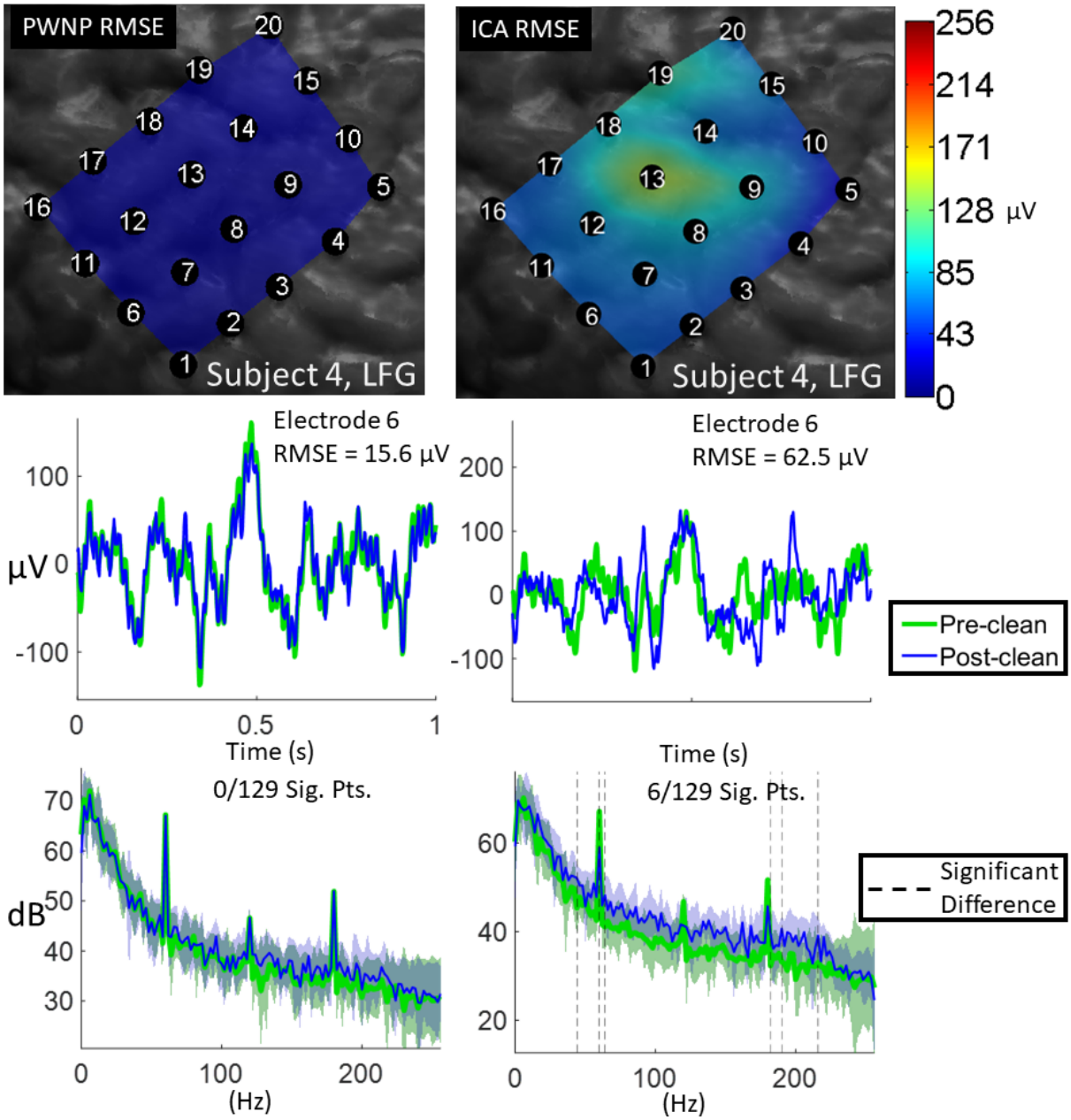

Figure 4.9: Baseline control experiment results for PWNP (Left) and ICA (Right) methods. (Top) RMSE values (Equation 4.6) spatially interpolated and mapped to MR-CT co-registered images of the ECoG grids from Subject 4. Color bar range is from 0 μV to 256 μV (maximum absolute voltage of the baseline data). (Middle) Representative baseline time domain examples before and after artifact suppression (Bottom) Representative frequency domain examples (mean PSD) from the same electrode before/after artifact suppression. Dashed lines indicate frequencies where the power distribution significantly differed before and after artifact suppression (signed rank test, $p<0.01$).

Table 4.4: Frequency-averaged interference indices, $\bar{I}$, and corresponding standard deviations, σ_I, for stimulation, PWNP-cleaned, and ICA-cleaned conditions for worst-case electrode in MEA data.

	Subject 5		
	Stim	PWNP	ICA
$\bar{I}$	0.292	0.045	0.089
σ_I	0.253	0.052	0.071

electrode on MEA2. Evidently, neural signals were dominated by extremely strong artifacts, whose amplitudes exceeded those of baseline signals by as much as two orders of magnitude. This is in contrast to the ECoG artifacts, which were generally an order of magnitude larger than the corresponding baseline signals (see Figure 4.5). Despite their large amplitude and broadband power distribution, these artifacts were still substantially reduced by both PWNP and ICA methods, bringing the signal amplitudes closer to those of the baseline data.

Figure 4.11 shows these representative signals in the frequency domain. The stimulation data PSDs exhibited a broadband increase, as well as peaks at the stimulation pulse train frequency (294 Hz) and its super-harmonics (589 Hz, 883 Hz, 1178 Hz, etc.). Note that these frequencies were rounded to the nearest whole number due to the 1-Hz frequency resolution of the PSD. Both PWNP and ICA reduced the artifact-related spectral features in the stimulation data and brought the resulting PSDs closer to that of the baseline data. However, PWNP appeared to outperform ICA as it produced data with less residual artifact.

The interference index of the stimulation data exhibited peaks at the stimulation frequency (294 Hz) and its super-harmonics, similar to their PSD. Figure 4.12 illustrates this phenomenon for the worst-case electrode. Both artifact suppression methods reduced the artifact peaks, with PWNP generally outperforming ICA. This was evidenced by PWNP achieving lower overall interference index values, for which summary statistics are shown in Table 4.4. PWNP also yielded signals with fewer significant residual interference frequencies in comparison to ICA (rank-sum test, $p<0.01$). These advantages were especially evident in the

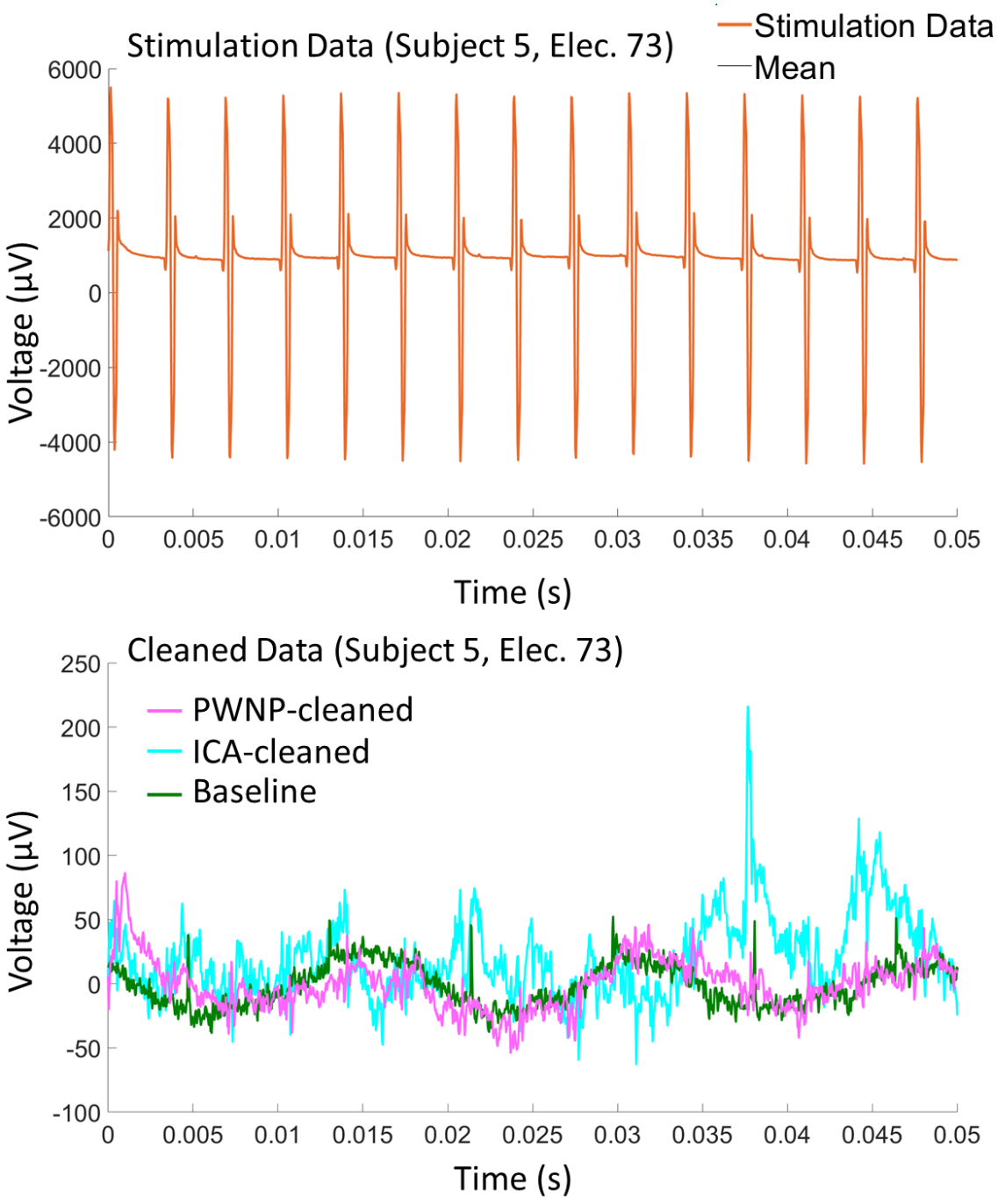

Figure 4.10: (Top) A representative sub-segment of the one-second long MEA stimulation epoch from the worst-case electrode on MEA2. (Bottom) The same data after artifact suppression using PWNP and ICA methods. Note the vastly different voltage scales before and after artifact suppression ($\sim$34$\times$). For reference, we show a duration-matched baseline segment sampled immediately preceding the stimulation data.

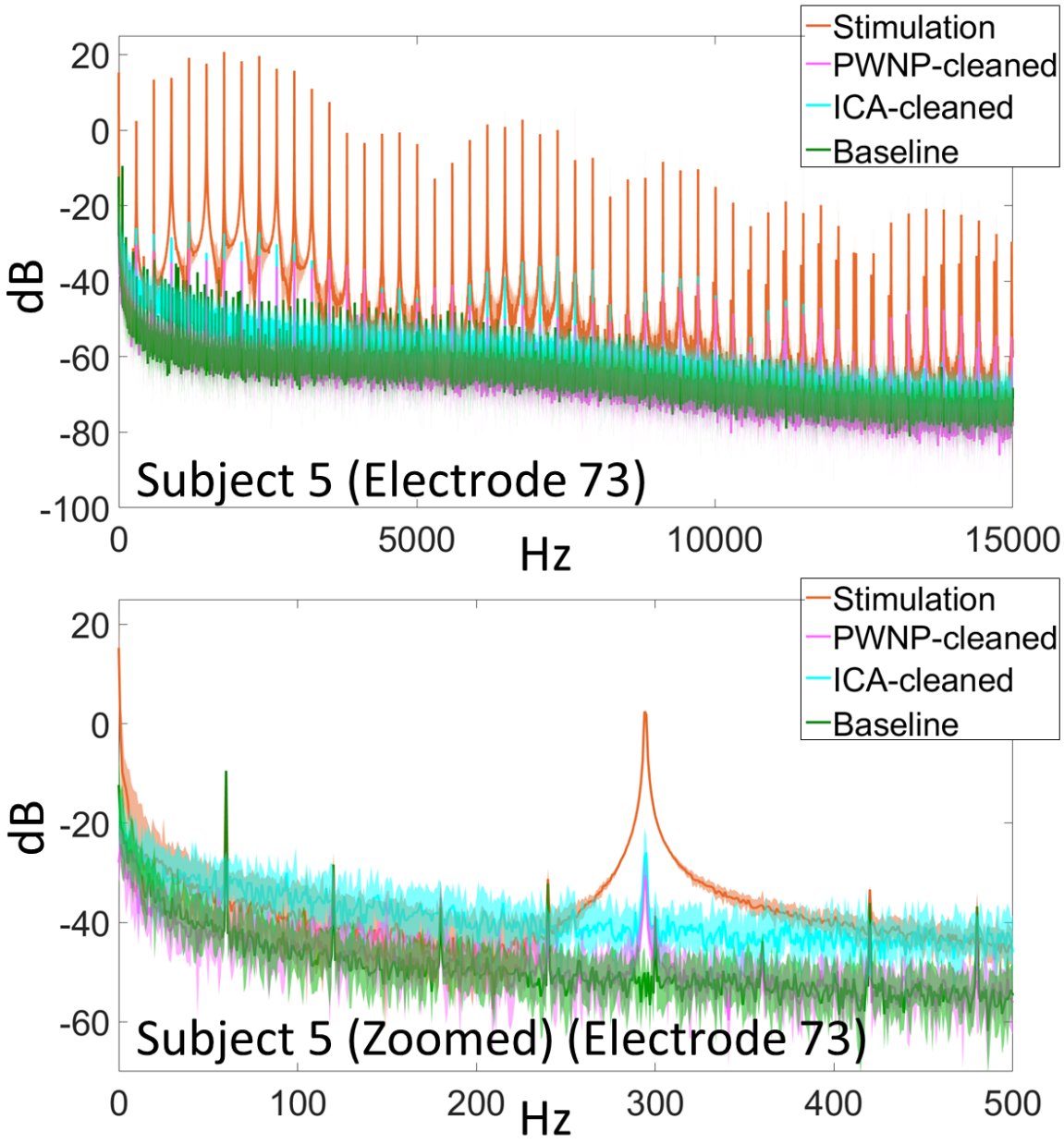

Figure 4.11: PSDs of signals under four different conditions from the worst-case electrode (Electrode 73) of MEA2. Solid lines represent the PSD averages taken over 10 stimulation epochs and shades represent corresponding one standard deviation bounds. (Top) Full PSD. (Bottom) Same PSD, zoomed to local field potential frequency range.

local field potential range (0-500 Hz).

To visualize the effectiveness of artifact suppression methods for the whole MEA, we spatially mapped the interference indices (Figure 4.13). Similar to the ECoG results, the map corresponding to the stimulation data exhibited the highest values. Likewise, upon artifact suppression, these map values were significantly reduced (paired, left-tailed, signed rank test; PWNP, $p = 8.4 \times 10^{-11}$; ICA, $p = 8.4 \times 10^{-11}$). Consistent with our worst-case electrode analyses, we observed that PWNP outperformed ICA. Specifically, the PWNP method achieved lower interference indices across electrodes (paired, left-tailed, signed rank test, p=0.000131).

Figure 4.14 shows the results of the baseline control experiment. As with the ECoG experiments, we expect artifact suppression methods to yield small RMSE values. The average RMSE value across electrodes was 10.5±2.2 μV for the PWNP method, which is approximately 4% of the pre-cleaning baseline voltage swing (235 μV). The ICA method, on the other hand, yielded much larger RMSE values (42.1±6.3 μV), and in turn, more significant signal distortions. Figure 4.14 shows time domain distortions for representative baseline signals after artifact suppression. These representative signals were taken from the electrode exhibiting the RMSE closest to the median RMSE across the grid. Similar to the ECoG experiments, the distortions introduced by PWNP were less prominent than those introduced by ICA. We also characterized these post-suppression baseline distortions in the frequency domain. Specifically, by comparing the PSDs before and after artifact suppression (signed rank test, $p<0.01$), we identified only two frequencies exhibiting significantly different power distributions after PWNP artifact suppression. In contrast, 54 frequencies were identified for ICA. To avoid potential performance bias towards the PWNP method, we performed control experiments on additional baseline epochs (C), while retaining the same PWNP and ICA parameters (same procedure as ECoG baseline experiments).

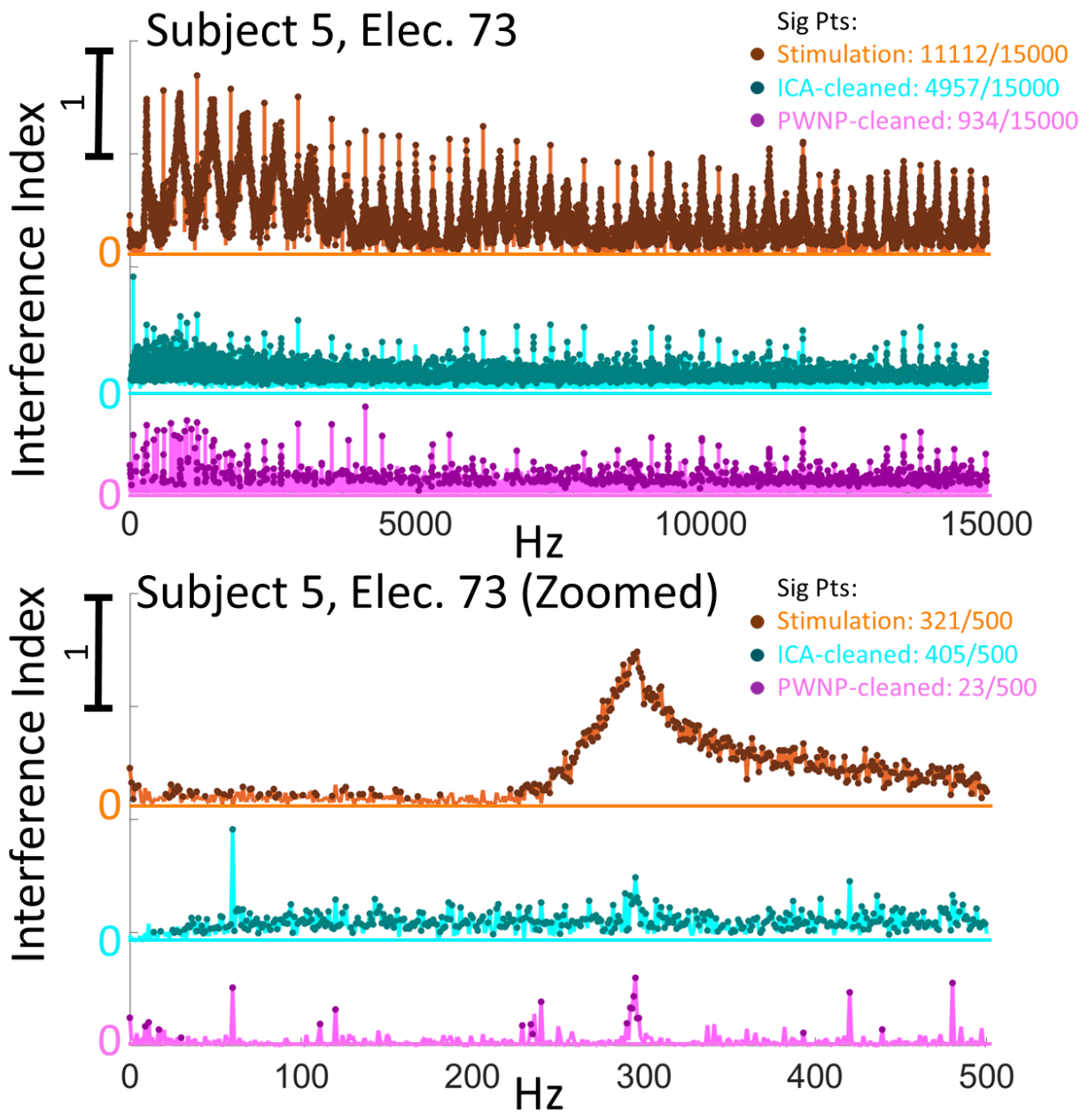

Figure 4.12: Interference index for the worst-case electrode from MEA2. Solid-colored lines are the interference index for the stimulation, ICA-cleaned, and PWNP-cleaned conditions. Filled-circle markers indicate frequencies were power distributions are significantly different from the baseline condition (rank-sum test, $p<0.01$). PWNP generally exhibited lower interference indices, as well as fewer frequencies with significant residual interference.

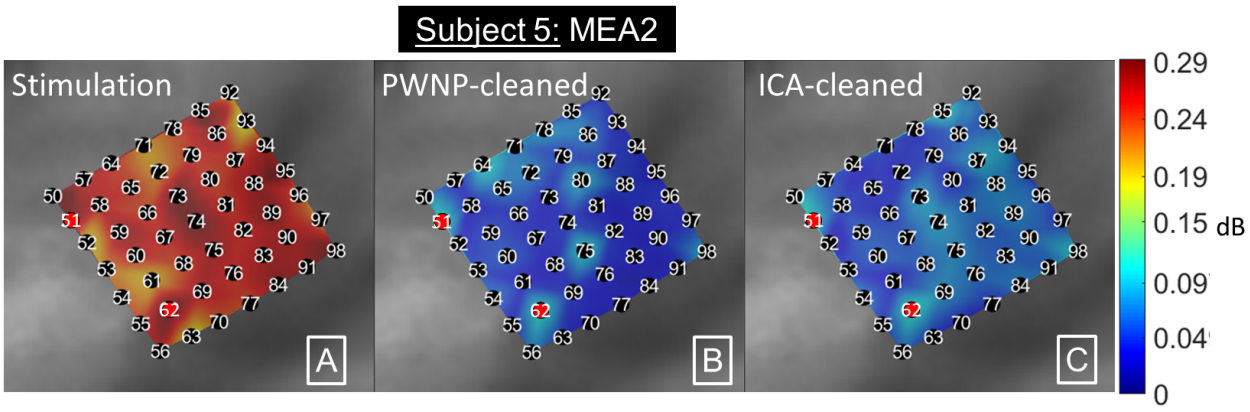

Figure 4.13: Interference indices spatially interpolated, color-coded and mapped to estimated MEA2 locations. (A) Interference indices for stimulation data. (B) Interference indices for PWNP-cleaned data. (C) Interference indices for ICA-cleaned data. Note that electrodes 51 and 62 were saturated, so their values were imputed to the highest in the grid to preserve the interpolation continuity.

4.3.4 Action Potential Recovery in MEA Stimulation Data

In the absence of stimulation data containing controlled behavioral tasks, we sought evidence for the PWNP method's ability to preserve neural features in recorded data. To this end, we observed stimulation data from an electrode containing action potentials (Electrode 59) before and after artifact suppression. Across the ten stimulation epochs a total of 135 action potentials were visually identified among the stimulation artifacts. The representative time domain data segments shown in Figure 4.15 demonstrate the ability of PWNP and ICA methods to selectively suppress the stimulation artifacts while preserving action potentials. Both techniques had a 100% retrieval rate of the observed action potentials.

4.4 Discussion

Our newly developed PWNP artifact suppression method has been extensively tested with a variety of neural data sets, ranging across EEG, ECoG and MEA. We compared the results

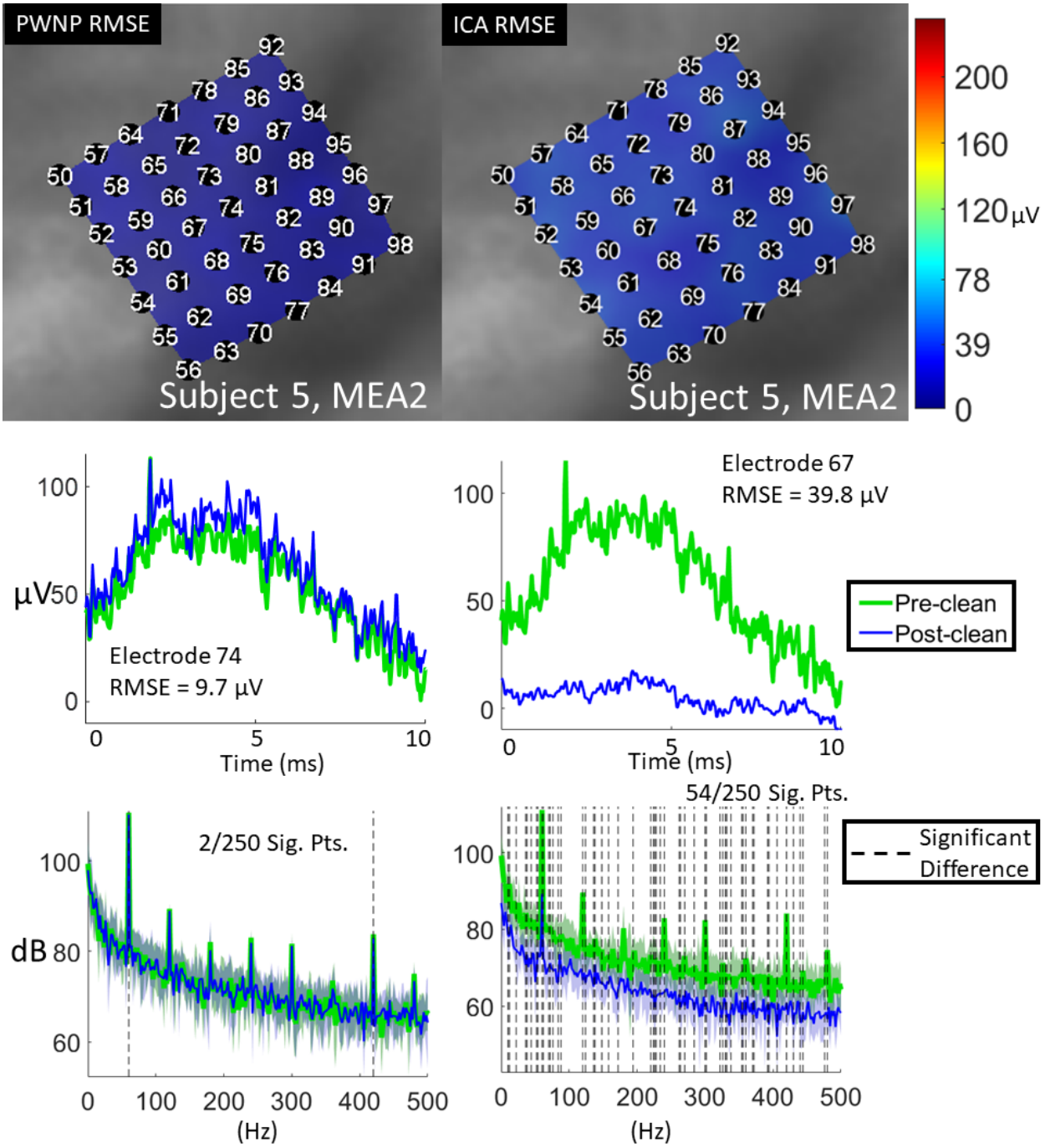

Figure 4.14: Baseline control experiment results for PWNP (Left) and ICA (Right) methods. (Top) RMSE values interpolated and mapped to estimated MEA2 electrode locations. Color bar range is from 0 μV to 235 μV (maximum absolute voltage of the baseline data). (Middle) Representative baseline time domain examples before and after artifact suppression. (Bottom) Representative frequency domain examples (mean PSD) from the same electrode before/after artifact suppression. Dashed lines indicate frequencies where the power distribution significantly differed before and after artifact suppression (signed rank test, $p<0.01$).

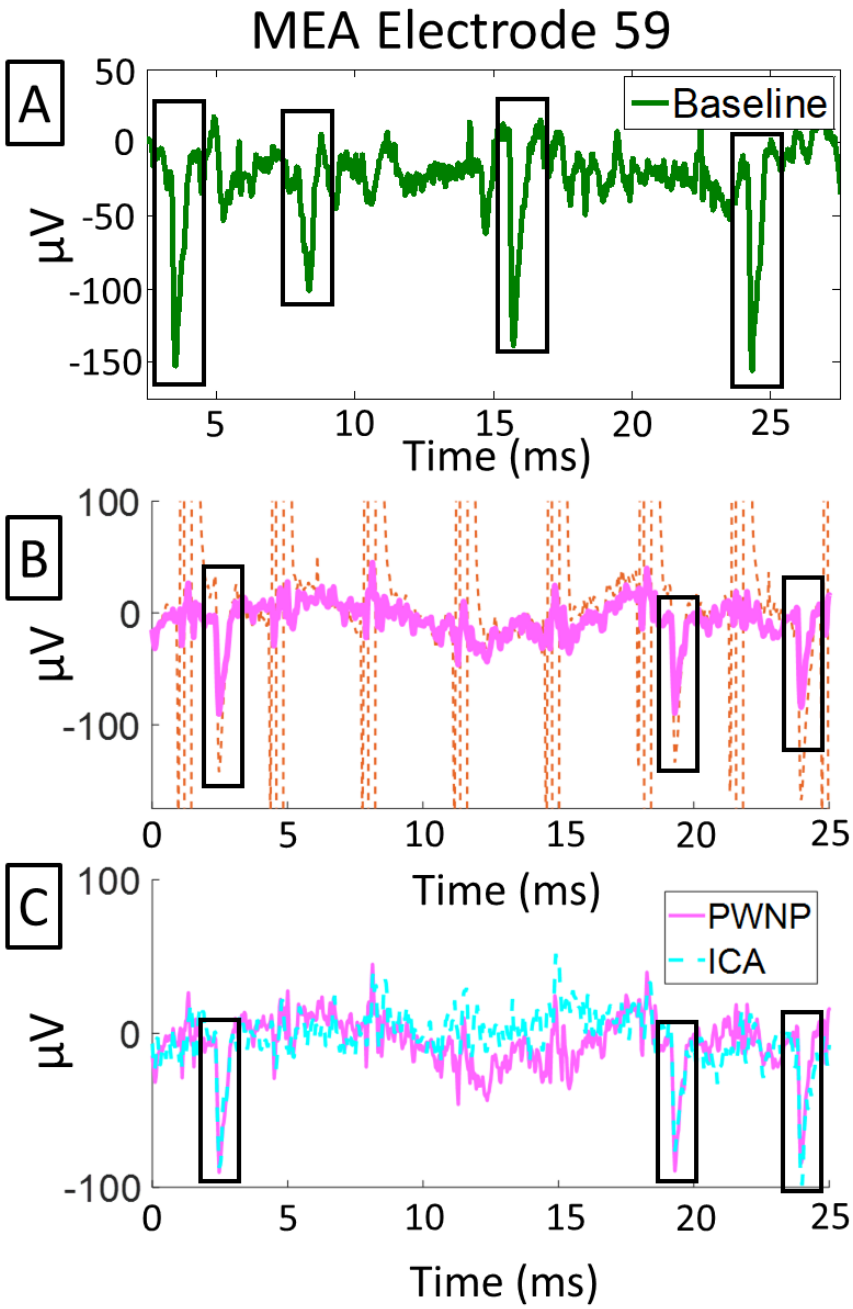

Figure 4.15: An example of action potentials in MEA data before and after application of PWNP and ICA methods. (A) Baseline data from an electrode exhibiting spontaneous action potentials (outlined in black). (B) Stimulation and PWNP-cleaned data from the same electrode. Stimulation artifacts reached ∼3 mV amplitudes, but are truncated for scale (C) Same data segment, comparing the PWNP-cleaned and ICA-cleaned conditions.

for our method to those of a state-of-the-art artifact suppression method, and generally found that it demonstrated a superior artifact suppression result.

In EEG data contaminated with narrowband artifacts, PWNP achieved substantial artifact suppression (expressed as SIR) while preserving the underlying α modulation (expressed as SNR). Specifically, PWNP effectively improved the SIR by a median of 32-34 dB, while preserving the SNR ($|\Delta\text{SNR}| \leq 0.18$ dB). Artifact suppression as high as 44-47 dB was achieved on electrodes nearby the stimulation channel (C3 for Subject 1 and Cz for Subject 2). Compared to ICA, PWNP achieved superior artifact suppression results, and these differences were statistically significant for both subjects. On the other hand, ICA yielded slightly higher SNR improvements ($|\Delta\text{SNR}| \leq 0.59$ dB), which is unsurprising as ICA inherently extracts neural sources. However, the primary objective of artifact suppression is SIR maximization, and we only used SNR to measure whether artifact suppression compromised physiological information. If the objective is SNR maximization, it would be more appropriate to apply supervised learning techniques [88] after artifact suppression is performed.

Extending our analysis from narrowband EEG artifacts to broadband ECoG artifacts, we observed that PWNP significantly reduced these features. Specifically, on worst-case electrodes, a reduction of broadband artifact features was indicated by a decrease of the frequency-averaged interference index by 0.31-0.32, while artifact suppression at the fundamental stimulation frequency and its harmonics were indicated by interference index reductions as high as 1.08-1.58. Additionally, upon PWNP artifact suppression, the average fraction of frequencies with significant contamination was reduced from 108/129 (84%) to 27.5/129 (22%). Our results generalize beyond the worst-case electrode, as we observed the reduction in interference indices across the whole grid. Similarly to the EEG results, the electrodes closest to the stimulation channel benefited the most from PWNP. Given that baseline data do not contain artifacts, we expect them to be unaffected by artifact suppression. Therefore, we performed baseline control experiments and demonstrated that the PWNP method did not significantly

distort these data. Specifically, PWNP yielded no statistically significant differences in the frequency domain, with a mean time-domain distortion of 6%. When these analyses were performed with ICA, the suppression results were inferior. Specifically, broadband suppression resulted in frequency-averaged interference index reductions of only 0.20-0.29 at the worst-case electrode, with reductions as high as 0.69-1.36 for the stimulation frequency and harmonics. Also, ICA yielded 66.5/129 contaminated frequencies on average. The ICA method also introduced significantly more distortion to the baseline data in comparison to the PWNP method. Thus, the results for the ECoG data show that PWNP outperforms ICA, and does so without imposing significant distortion onto the baseline data.

Repeating the analyses performed in ECoG data with MEA data, we observed a similar suppression of artifact features for the PWNP method. For a worst-case electrode, broadband artifact suppression was represented by a reduction in the frequency-averaged interference index of 0.25. Additionally, artifact suppression at the stimulation frequency and harmonics were represented by interference index reductions of 0.88 to 1.03. We also observed a decrease of the fraction of interference contaminated frequencies from 321/500 (64%) to 23/500 (5%) in the local field potential range. These worst-case electrode results also extend to the whole MEA, as we observed a significant reduction in interference indices across the whole grid. Similar to the ECoG analyses, PWNP introduced only a 4% time-domain distortion to the baseline with only two statistically significant frequencies in the frequency domain. The PWNP-cleaned data also achieved these artifact suppression results while preserving 100% of the action potentials in the stimulation data. Comparing the PWNP results to those of ICA, ICA yielded 405/500 contaminated frequencies in the local field potential range for the worst-case electrode. ICA broadband suppression achieved a frequency-averaged interference index reduction of 0.20, with reductions of 0.87-1.11 at the stimulation frequency and harmonics. The baseline control experiments also indicated ICA may be altering the underlying neural data, with a time-domain distortion of 25% and 54 frequency-domain points with significant difference after ICA cleaning. ICA did, however preserve the action

potential features, similarly to PWNP. Overall, PWNP again demonstrates effective artifact suppression performance, while retaining action potentials present in the stimulation data.

In addition to its superior artifact suppression performance, PWNP also provides the advantage of simplicity and ease of implementation. It is significantly easier to identify the artifact subspace in PWNP, as it natively collects high-energy features, like artifacts, into a few components. In contrast, ICA components are not ordered or sorted in anyway, requiring a combinatorial search to find the components spanning the artifact subspace. This is further complicated by the fact that even guiding measures like SIR cannot be solely relied upon, as a combination of components exhibiting the lowest SIR values are not guaranteed to achieve the optimal artifact suppression result. Additionally, artifact suppression methods must preserve the quality of underlying neural signals, which is a condition that ICA seems to fail in the presence of stimulation artifacts in ECoG and MEA data. This is likely due to the fact that ICA is over-constrained by the requirement of independence for its components, as artifacts and neural signals are not guaranteed to be independent of each other. This was evidenced by alternative artifact subspaces that we identified for the MEA data, which would improve the artifact suppression but also remove the action potentials. PWNP avoids these issues by rank-ordering its components, and separating neural and artifact subspaces based on a single, well-justified (Appendix ??) parameter α. We find that the $\hat{\alpha}$ parameters were close to the ideal value of 1, with all but a single EEG subject ($\hat{\alpha} = 2.7$) falling within $\hat{\alpha} \in [1.1, 1.7]$.

A limitation to the work is that the ECoG and MEA stimulation was collected without an underlying behavioral signal. We only have the α modulation EEG data to quantifiably demonstrate the preservation of behaviorally modulated signal after PWNP artifact suppression. We have compensated for this lack of behavioral task with the baseline control experiments and the demonstration of action potential retrieval, but ultimately, ECoG/MEA data with labeled behavioral tasks will be required to finalize our findings. Additionally, we

have yet to demonstrate the real-time artifact suppression capabilities of the PWNP method, wherein novel data is presented for artifact suppression after training. This would typically be done using an N-fold, cross validation analysis [111]. We did not perform such analysis in this work, as we wanted to compare PWNP to the current state-of-the-art ICA. It would be prohibitively time-consuming to perform the ICA method in a cross-validation analysis, as each fold would require a new combinatorial search. This very quickly becomes impractical as we approach a statistically significant number of folds. On the other hand, PWNP lends itself very readily to such a cross validation analysis, as only α needs to be found for each fold. This can be easily done with the worst-case electrode method described in Section 4.2.2. Thus, we propose that future analyses could very easily test the capability of PWNP in a cross-validation framework and, by extension, real-time BD-BCI operation.

Chapter 5

Demonstration of Walking Exoskeleton BD-BCI

5.1 Motivation

Informed by the artifact analyses from the works describe in previous chapters, as well as existing BCI development performed by our lab, we have designed a BD-BCI device intended to interface with a walking leg exoskeleton. The device was fabricated using off-the-shelf components and abides by fully-implantable restrictions (e.g. power dissipation, stimulation output). This mitigates costs and allows the device to serve as a test-bench for a fully-implantable, embedded system BD-BCI prototype. The BD-BCI used for this study incorporates both a version of the BCI designed by Wang et. al [99] and the stimulator device designed by Sohn et. al [112, 94, 96]. These devices were further integrated to allow the stimulator and BCI to work in a bi-directional control scheme, and as well as to allow for communication between the exoskeleton and the BD-BCI. For this study, we utilized signals from ECoG electrodes implanted in an epilepsy subject undergoing surgical evaluation as a

part of Phase II epilepsy monitoring. The subject was able to enact wireless BCI control over a robotic leg exoskeleton, while simultaneously receiving artificial sensation via cortical electrostimulation during leg swing.

5.2 Methods

5.2.1 Exoskeleton BD-BCI System Overview

An overview of the exoskeleton BD-BCI system is shown in Figure 5.1. Three main devices comprise this system: the BD-BCI itself, the Lower Limb Station (LLS) and the Ekso-GT lower extremity exoskeleton (Ekso Bionics, Richmond, CA, USA). The BD-BCI is responsible for both neural recording and stimulation feedback functions. It performs real time decoding of neural signals to determine movement commands for the exoskeleton. The BD-BCI accomplishes this by communicating wirelessly with the LLS to initiate steps on the exoskeleton, as well as to receive information about exoskeleton movement. The LLS, which contains a microcontroller and a transceiver, controls a servo that presses the stepping button on the exoskeleton. It is also wired to gyros attached to the ankles of the exoskeleton that report angular velocity. This kinematic data can then be used to wirelessly instruct the BD-BCI stimulator to trigger when the exoskeleton is in motion, thus completing the bi-directional loop. The following sections will describe more in detail the hardware and software specifications of these devices.

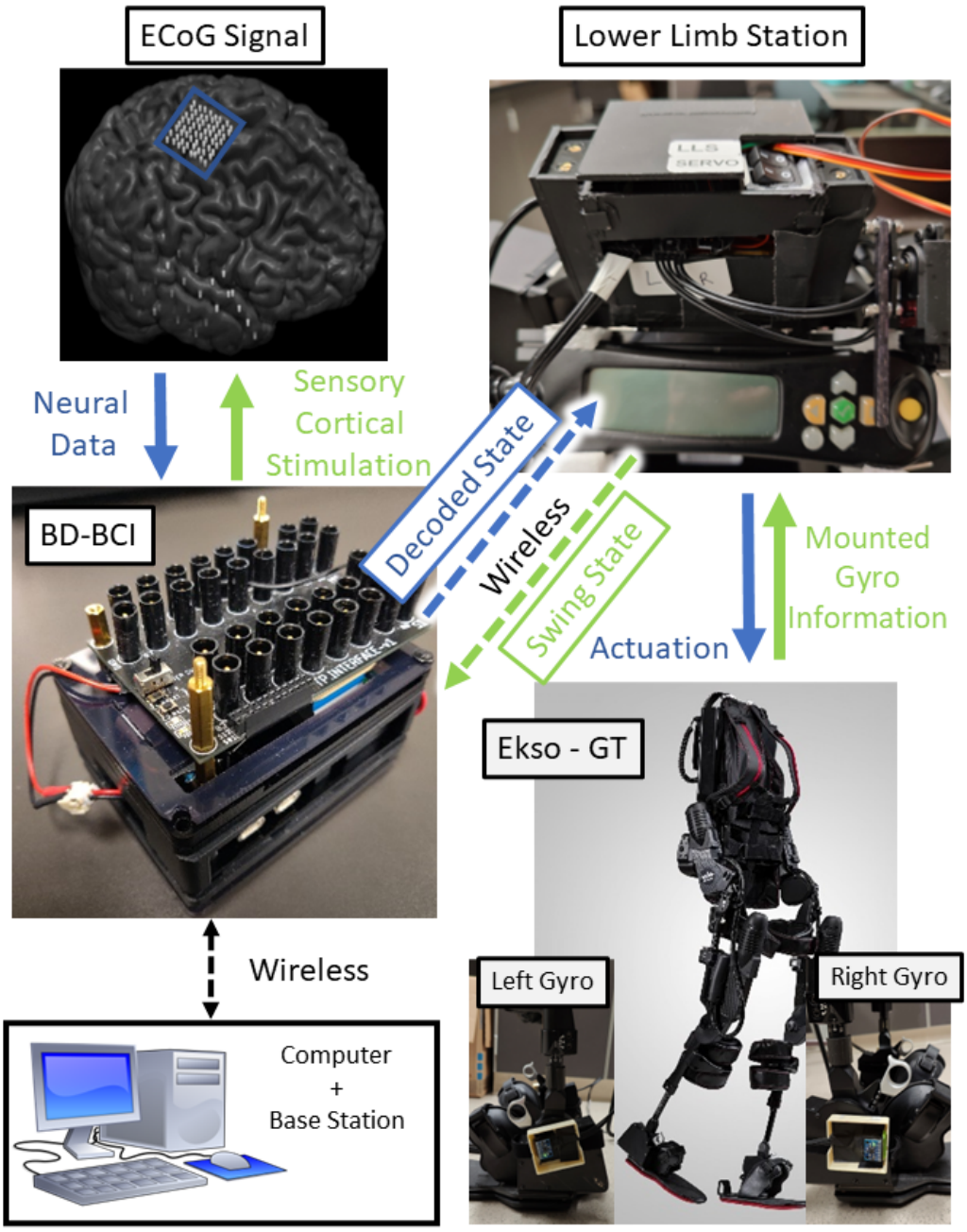

Figure 5.1: Overview of Ekso BD-BCI system. Computer and Base Station are used to initiate and stop training/decoding procedures on the BD-BCI, as well as program stimulation parameters. ECoG signals are recorded by the BD-BCI and are internally decoded into move or idle commands. These commands are transmitted wirelessly to the Lower Limb Station (LLS), which then actuates the Ekso if a move command is received. Gyros mounted on the ankles of the Ekso detect leg swing and inform the LLS, which in turn transmits the swing state wirelessly to the BD-BCI. The BD-BCI will then stimulate the ECoG electrodes to elicit leg-swing sensation.

5.2.2 BD-BCI Decoding Path Design

Hardware Design

The BD-BCI device consists of three microcontroller cores (48 MHz ARM Cortex-M0+ microcontrollers; Microchip, Chandler, AZ). Core 1 primarily handles signal acquisition, whereas Core 2 handles mathematical computation. Core 3 controls the stimulation and will be further discussed in Section 5.2.3. Processes were split amongst these three cores to enable efficient real-time performance of BD-BCI operations. The recording hardware consists of a 32-channel commercial bioamplifier integrated circuit with multiplexer and 16-bit analog-to-digital (ADC) converter (Intan Technology, Santa Monica, CA) that records neural data at 500 Hz. Due to physical constraints, only 16 of these channels are physically routed to 1.5 mm touch-proof jacks for connection to neural signal sources (EEG, ECoG, etc.). These components are assembled onto a custom PCB alongside other supporting hardware, including a LoRa MedRadio band transceiver (HOPE Microelectronics, Xili, Shenzhen, China), two 512 kB ferro-electric random access memory (FRAM) flash memory chips (Cypress Semiconductor, San Jose, CA), and a 512 mB NAND flash memory storage module (Micron, Boise, ID). A desktop computer connected to a Feather ARM M0 board (Adafruit Industries, New York City, NY) with an onboard RFM95 LoRa Packet Radio Transceiver issues commands wirelessly to the BD-BCI. This wireless communication is only necessary for training/building of decoding models, initiation/termination of online BCI operations, otherwise the BD-BCI is capable of operating independently from the desktop computer. All transceiver protocols comply with Federal Communication Commission designated Medical Device Radiocommunications Serivce for implantable medical devices [113]. The BD-BCI system is battery-powered with a 3.7 V, 2500 mAh Lithium-Potassium (Li-Po) battery, and thus is portable unlike most existing BCI systems which rely on bulky, stationary computer hardware. Additionally, our previous work [99] demonstrates how the power consumption of

the BCI device theoretically follows fully implantable power dissipation constraints.

BCI Software Design

The BD-BCI software implemented a binary state decoder, performing real time classification of neural signals into move/idle states, which was used to control the exoskeleton. This software was written in C++ and compiled using Visual Studio (Microsoft Corp., Redmond WA). A Windows Forms graphical user interface written in Visual C# allowed for training/building of decoding models, initiation/abort of online BCI operations, setting of BCI parameters, as well as offline downloading of training data. A supervised binary state decoder implemented in Core 1 and Core 2 enabled decoding of neural signals as has been performed in previous BCI developed by our lab [72, 114, 115, 116, 99].

BCI Decoder Training

To train the decoder, we must first build a feature extraction data using training data collected separately during idling and movement. Once this feature extraction matrix was learned, ECoG data collected in real time could be efficiently processed to determine the state of the data. To facilitate the decoder training procedure, we implemented a protocol on the BD-BCI wherein the BCI GUI displays and speaks either "IDLE" or "MOVE" to the BCI subject, while simultaneously acquiring a pre-specified duration of neural data and saving it to the NAND memory. When "IDLE" is displayed, the subject holds still and looks forward at the cue screen. When "MOVE" is displayed, the subject performs the motor task, e.g. left hip flexion/extension. This protocol was used to collect up to 5.5 sec idle or move epochs, alternating between the two conditions until a total of 90 sec of training data is acquired. These signals were captured at 500 Hz after application of a configurable 7.5 - 200 Hz 4th order analog biquadratic filters. The data were then stored and the decoder building

process began by calculating the average power in the μ - β band (8-35 Hz) and the high-γ (80-160 Hz) band for each saved epoch. These frequency bands were chosen as they have shown to exhibit modulation in response to movement. For the case of the μ - β band in lower extremity motor behavior, the power is higher during idle periods, and lower in move periods [117, 118, 26]. For high-γ, the power is increased during move periods and decreased during idle periods [117, 118, 26]. The first one second of each idle/move epoch is discarded to account for human response time to the cue and the latency of neural modulation. The remaining 4.5 sec of data is divided into 750 ms non-overlapping segments. These segments were then common average referenced, and the in-band power was calculated for each channel and segment.

The band powers were concatenated and then processed using a class-wise principal component analysis (CPCA) [119]. This CPCA was used to reduce the dimension of the training data by retaining only principal components accounting for 92% of the variance in each class. After application of the CPCA transformation, linear discriminant analysis (LDA) [120, 121] further improves the separability between classes. The CPCA and LDA transformations can then be combined as follows:

$$f = T_{\text{LDA}} \Phi_{\text{CPCA}}(d) \tag{5.1}$$

where f is the extracted feature resulting from the LDA (T_{LDA}) and CPCA (Φ_{CPCA}) transformation matrices, $d \in \mathbb{R}^{2c \times 1}$ contains the the band powers, and c is the number of recording channels. See Appendix D.1 and Appendix D.2 for a full description of the calculation of the CPCA and LDA transformations. The CPCA and LDA transformation matrices corresponding to individual training runs were saved to memory for use in subsequent online decoding runs.

BCI Online Decoding Operation

Online BCI operation was performed using a sliding window and was interleaved with the feedback stimulation (Figure 5.2). Details regarding the stimulation protocol are in Section 5.2.3. During online BCI decoding operation, Core 1 controlled the amplifier and acquired 500 ms of data at a time. The first 250 ms is rejected to account for amplifier settling. The rejected time also accounts for the time to discharge potential voltage deviations persisting in the neural tissue and electrode-tissue interface [2, 59, 5] when interleaved sensory stimulation is triggered. For the sliding window, the three most recent 250 ms online segments are appended together to form one 750 ms online window. While the state is decoded as idle, online segments are collected consecutively. Once a move state is detected, the BD-BCI switches to an interleaving acquisition mode to accommodate sensory feedback stimulation. This was done as the activation of the stimulator causes significant noise on the device ground, which can compromise decoding acquisition. During interleaved acquisition, the BD-BCI will pause the amplifier when a move state is decoded in anticipation of exoskeleton movement. Once the stimulation triggered by the exoskeleton is completed (i.e. exoskeleton finishes moving), acquisition will resume. If the move state persists, interleaving continues, otherwise if an idle state is detected, the device will revert back to non-interleaving acquistion.

The features are then extracted from each sliding window by applying the CPCA and LDA transformations. Using this feature, a linear Bayesian discriminant [121] is applied in order to determine the class for the online window. This assumes that the posterior probabilities for each class have Gaussian probability density functions with equal variances. The following class posterior probabilities are calculated: $\mathrm{P}_I(I \mid f^*)$, $\mathrm{P}_I(M \mid f^*)$, $\mathrm{P}_M(I \mid f^*)$ and $\mathrm{P}_M(M \mid f^*)$. Where f^* is the observed feature, and $P_I(\cdot|\cdot)$ and $P_M(\cdot|\cdot)$ are the posterior probabilities calculated for the idle and move class subspaces, respectively. Note that since we used a binary state decoder $\mathrm{P}(M \mid f^*) = 1 - \mathrm{P}(I \mid f^*)$. For a full description of how these

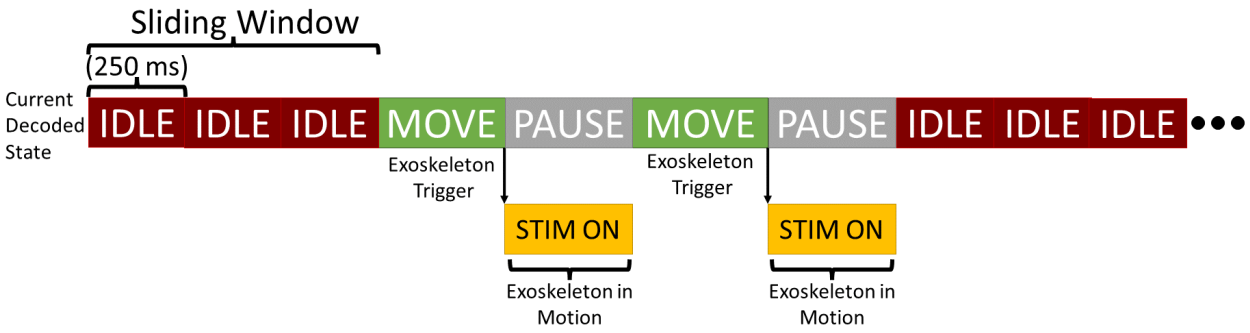

Figure 5.2: Diagram of online BD-BCI interleaving scheme. State is determined for each sliding window (3 most recent online segments). In the idle state, these segments are collected consecutively. If a move state is detected, the device will pause until the exoskeleton has finished moving and stimulation has finished. Interleaving persists if move state is detected again afterwards, or goes back to normal operation if idle state is detected.

posteriors were calculated, see Appendix D.3. These posteriors were compared, and the state in the subspace with the highest posterior probability becomes the dominant class posterior, $\bar{\mathrm{P}}(\cdot|f^*)$. If there is disagreement between subspaces, then the the overall highest posterior is used to determine the state. We then utilized a dual threshold to determine the decoded state from the dominant class posterior (cf. Figure 5.3). Specifically, $\bar{\mathrm{P}}(\cdot|f^*)$ was compared to move and idle thresholds, T_M and T_I, respectively. In the case of $\bar{\mathrm{P}}(\cdot|f^*) > T_M$, the device will transition to the move state, or retain the state if it is already currently in the move state. Similarly, if $\bar{\mathrm{P}}(\cdot|f^*) < T_I$, the device will transition to or retain the idle state. Consequently, when $T_I \leq \bar{\mathrm{P}}(\cdot|f^*) \leq T_M$, the BD-BCI maintains the current state. Once the state has been decoded for a sliding window in real time, the current state and its posteriors are transmitted to the base station for logging purposes. Typically, T_M and T_I were calibrated as part of the training process by performing an online decoding run after the decoder was built. The posteriors collected during this online decoding run were automatically labeled and logged by the device. We downloaded these posteriors and used a custom MATLAB script to plot a histogram of the posteriors for each state. We then chose T_I and T_M such that the move and idle states were the most clearly delineated. These thresholds are then input to the BD-BCI GUI for use during subsequent online decoding runs.

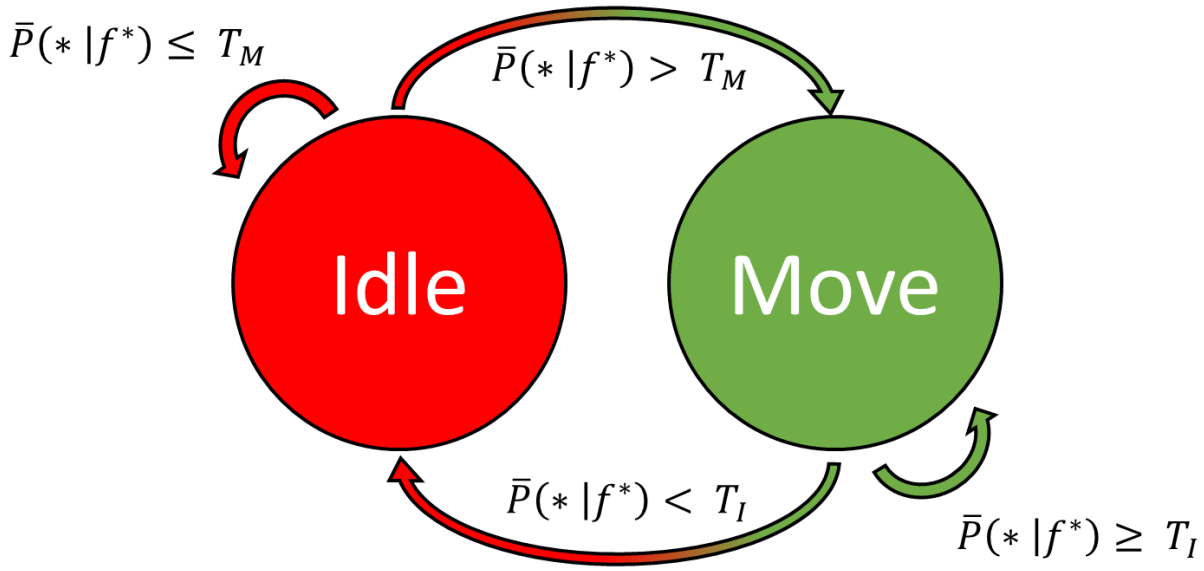

Figure 5.3: Binary state decoder for BD-BCI exoskeleton system. For each sliding window, the BD-BCI compares the dominant class posterior, $\bar{P}(\cdot|f^*)$ against T_M and T_I to determine the state.

5.2.3 BD-BCI Stimulator Design

The onboard stimulator and supporting software was designed to both elicit stimulation The stimulation was generated on-board the BD-BCI and was controlled primarily by Core 3. The current for the stimulation was supplied by a current source (Linear Technology, Norwood, MA), followed by a cascade of two charge pumps (Maxim Integrated, San Jose, CA) that increased the 3.3 V_{cc} up to 13 V depending on amperage requirements. The current amplitude is then determined by a programmable digipot parameter. An H-bridge then delivers the stimulation current as a bipolar, biphasic square pulse waves across a stimulation channel. The pair of electrodes that comprise the stimulation channel can be selected from 16 total electrodes using a 1:16 multiplexer (Analog Devices, Norwood, MA). These 16 electrodes are each connected to 1.5 mm touchproof jacks, which can then be interfaced with ECoG leads to deliver electrical current to the cortex. Additional charge-balancing mechanisms (described in [112, 94, 96]) were also implemented to minimize the effect of

stimulation artifacts on the neural signal. This architecture was designed in CAD software and realized on a custom PCB. This stimulator was demonstrated to have an equivalent output to an FDA-approved stimulator in a study performed by our group [96].

A software GUI programmed in Visual C# allows for the selection of anodic/cathodic pulse widths, current amplitude, pulse frequency and stimulation channel. These parameters are pushed wirelessly and saved locally on the BD-BCI. After these parameters are set, the GUI can be used to manually initiate stimulation to test sensory percepts. These parameters can also be programmed for stimulation initiated externally by an end-effector (e.g. by the LLS during exoskeleton movement).

5.2.4 Exoskeleton Integration

The BD-BCI was integrated with the Ekso-GT exoskeleton such that decoded move states initiated the exoskeleton's stepping functions. In turn, exoskeleton movement triggered the BD-BCI stimulator to elicit artificial sensation on the cortex. The Ekso-GT is a leg exoskeleton that has FDA approval for rehabilitation use in stroke and SCI patients. Physical therapists outfit a patient with the Ekso-GT in order to perform assisted walking exercises using the Ekso-GT's controller to manually initiate stepping cycles. We utilized this manual walking function to give the BD-BCI control over the exoskeleton. As the Ekso-GT does not natively have the ability to communicate wirelessly with external devices, we designed the LLS to give the BD-BCI the ability to interface with the Ekso-GT.

The LLS is responsible for both the actuation of exoskeleton in response to decoded state and detection of exoskeleton leg movement. It contains a Feather ARM M0 board with an onboard RFM95 LoRA Packet Radio Transceiver (Adafruit Industries, New York City, NY) and is powered by a 3.7 V, 2500 mAh Li-Po battery. The Feather M0 board is mounted onto a custom PCB, which connects it to two gyros (InvenSense MPU-6050, TDK Corporation,

Tokyo, Japan), a rotational servo (MG996R, Tower Pro, Hunt Valley, MD), and an electret microphone/amplifier sensor module (Tan Fei Fei, Dong Guan, Guangdong, China). The two gyros are connected to the custom PCB via a series of 2 ft stackable linear modular connectors (Molex, Lisle, IL) so that they can be attached at the exoskeleton ankle. The servo was mounted on a custom-built extruded aluminum mount designed to hold the controller of the Ekso-GT and was powered by four 1.5 V batteries contained inside the LLS. The servo would receive motor commands from the Feather M0 to press the stepping button on the Ekso-GT controller, initiating a walk cycle on one leg. Upon completion of a step, the exoskeleton emits an audio tone, which was detected by the microphone. In response to step completion, the LLS can then transmit a "stop stimulation" command to the BD-BCI. The microphone step completion detection was also used so that the LLS does not attempt to actuate the exoskeleton again until it has finished moving. Additionally, a 2.5 second stepping refractory period was implemented in the LLS to prevent excessive steps from being triggered.

During online decoding, the BD-BCI transmits the decoded state (move or idle) to the LLS. Upon receipt of a "move" decoded state, the LLS will actuate a servo which will push the "step" button on the exoskeleton. This will cause the exoskeleton to take a step, which will trigger the gyros attached to the ankle of the exoskeleton leg that is moving. These gyros stream the angular velocity of both legs via an SPI interface to the LLS. When either gyro exceeds a manually calibrated threshold (Figure 5.4), the LLS transmits the "start stimulation" command. The "stop stimulation" command is then transmitted when both gyros fall below a "stop" threshold or the detection of the exoskeleton's step completion audio cue, whichever comes first. The gyro thresholds are set to default values based on the exoskeleton kinematics to maximize sensitivity of movement onset, while not sacrificing stability when the exoskeleton is idle. Software on the LLS also allows for manual tuning of these thresholds based on the weight of the person in the exoskeleton. Upon receipt of the stop stimulation command, Core 1 is notified that acquisition of the next data window may proceed.

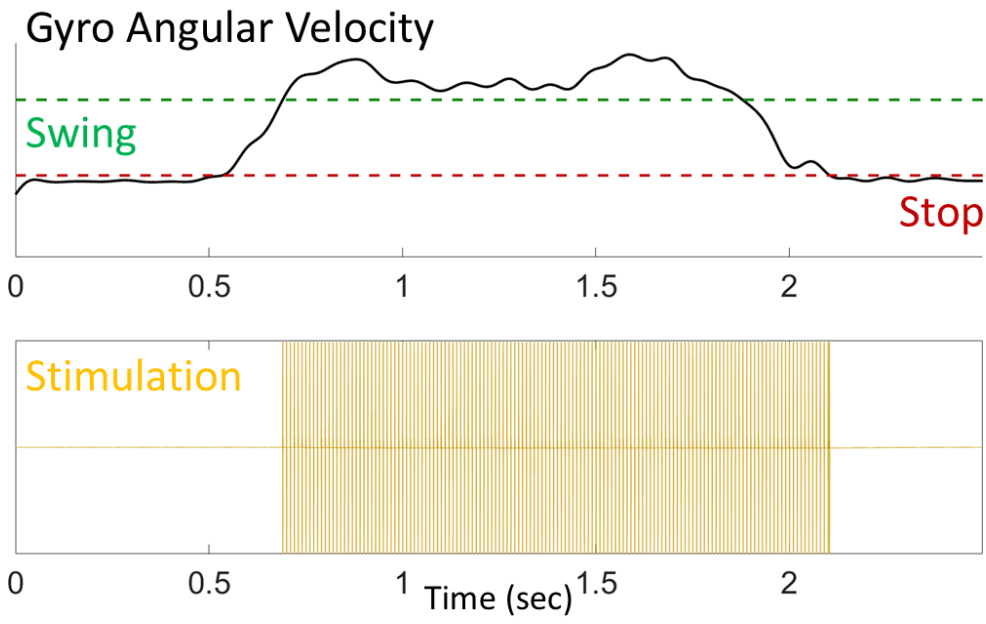

Figure 5.4: Diagram demonstrating stimulation triggering in response to exoskeleton movement. (Top) Data from the LLS gyros. Green line indicates the swing threshold, red line indicates the stop threshold. (Bottom) Data from the stimulator output. When the angular velocity exceeds the manually set swing threshold, the LLS triggers the stimulator to start. When angular velocity falls below the stop threshold, stimulation is terminated.

5.2.5 Bedside ECoG Signal Acquisition and BCI decoder training

A single subject undergoing Phase II epilepsy evaluation at Rancho Los Amigos National Rehabilitation Center is implanted over the right sensorimotor area an 8×8 ECoG grid (Ad-Tech, Oak Creek, WI). The MR-CT co-registered image (See Appendix A) for this sensorimotor grid (SMG) is shown in Figure 5.6. Data from all 64 electrodes was first recorded using a clinical-grade bioamplifier (Natus®Quantum™, Natus Medical Incorporated, Pleasanton, CA) during a left hip flexion/extension task. The subject was verbally cued to alternate between 10 second periods of leg motor task or idling task. These periods were annotated in the data to aid segmentation in offline analysis. These data were then saved and downloaded for analyses to determine which electrodes exhibited μ - β or high-γ modulation. The data were segmented based on the annotations, then the μ - β and high-γ amplitude envelopes were calculated by first band-passing (4th Order Butterworth) to the appropriate frequency band (8-35 Hz for μ - β band and 80-160 Hz for high-γ band) then low pass filtering at 2 Hz (2nd Order Butterworth). These amplitude envelopes were then visually inspected, and those exhibiting modulation following the motor task were then chosen for use with the BD-BCI.

Once the relevant motor electrodes were identified, the training data was collected. This was performed by positioning a computer monitor in front of the subject to present the cues. Cues are presented as a either the word "IDLE" or "MOVE", accompanied by a voice-to-text of the same word. To allow the subject more time to perform the motor behavior, the cue presentation was organized such that each block consisted of two consecutive 5.5 sec idle epochs followed by two consecutive 5.5 sec move epochs. Factoring in the one-second skip, this results in alternating periods of 9 seconds in each state, for a total of 3 idle epochs and 3 move epochs. After this data were saved by the BD-BCI, the decoding model is built using the procedure described in Section 5.2.2. The resulting feature matrices for the $\mu - \beta$ and high-γ bands can be visualized by interpolating, color-coding, and mapping the feature

weights to the ECoG location on an MR-CT co-registered image. Additionally, the quality of the training data was assessed by performing an offline decoding analysis using a custom MATLAB script that performs a stratified 10-fold cross-validation [111]. In this process, the training data was randomly separated into 10 folds, of which nine were designated to build the CPCA-LDA Bayesian decoder and one was left for classification. After a state was assigned to the classification fold, a new fold was selected for classification with a new CPCA-LDA Bayesian decoder built using the remainder of the folds. This was repeated until all 10 folds were classified, and the accuracy of the decoder was calculated by the proportion of correctly identified folds. This 10-fold cross validation is repeated 10 times, randomizing the separation of the folds each time, to obtain a mean and standard deviation of the decoder accuracy. Once the decoder was built, a short online decoding run consisting of 3 move/idle periods lasting 10 seconds was performed to log move/idle posterior probabilities to determine T_M and T_I.

5.2.6 Artificial Sensation Mapping

To determine what electrode pair and stimulation parameters to use for the exoskeleton sensory feedback, we first performed mapping the cortex covered by the ECoG grid. The procedure followed here is identical to the process performed in Phase II epilepsy clinical evaluation for eloquent cortex mapping. For the sake of time efficiency, we chose to map a subset of electrodes lying towards the sensory cortex, e.g. SMG41-43, SMG49-51, and SMG57-64. Adjacent electrode pairs were chosen from this subset to act as stimulation channels, and the current setting was varied to investigate whether sensory feedback could be elicited from each channel. Note that this current setting is proportional to the current applied (mA). A pulse frequency of 50 Hz and a pulse width of 250 μs was used for all stimulations to match the parameters typically used in the clinical mapping performed at Rancho Los Amigos. One-second test stimulation pulse trains were manually initiated using

the stimulation GUI and the subject was instructed to verbally describe whether or not a sensation was felt for each unique set of stimulation channels and parameters. Since we were deploying a walking exoskeleton BD-BCI, and the ECoG grid was implanted over the right sensorimotor area, we searched for those channels eliciting what the subject described as left leg sensation. As the objective was to obtain a single sensory percept to act as an exoskeleton feedback sensation, an exhaustive mapping of all stimulation channels and parameters was not performed.

Once the parameters for a suitable sensory percept was found, the consistency of that percept was validated using a step counting test. This ensured that the reported percept was repeatable and distinguishable over multiple stimulations. For this test, the BD-BCI was configured to stimulate using the channel and parameters identified to elicit left leg sensation in the previous sensation mapping task. Subsequently, one of the exoskeleton gyros was strapped to the left leg of one of the experimenters, and that experimenter was instructed to stand out of view outside of the subject's room. The experimenter was then instructed to take a predetermined number of steps within a 10 second period. The subject was then asked to report how many steps they perceived. This process was repeated for 14 trials, for a number of steps per trial between 2 and 8. The error between the taken and reported step numbers was then calculated over trials and the total percent correct as $P_{correct} = n_c/n_t * 100$, where n_c is the total number of counted steps across trials, and n_t is the total number of taken steps.

5.2.7 Demonstration of BD-BCI Ekso Operation

Once both the sensory feedback parameters and BCI decoder were prepared, we then performed online experiments using the exoskeleton BD-BCI in both stimulation and non-stimulation runs. In this way, we can demonstrate how bi-directional operation can be

enabled while not compromising BCI decoding performance. To do this, we set up the exoskeleton BD-BCI to work in a proxy control scheme. The ECoG subject remained in the bed and controlled the exoskeleton BD-BCI wirelessly using left leg hip flexion/extension movements (Figure 5.5). A healthy experimenter donned the exoskeleton while wearing an Xsens motion capture system (Xsens Technologies, Enschede, Netherlands) to record the kinematics of the exoskeleton walking. The exoskeleton is then set up outside the subject's room in a 30 m walking pathway. A webcam was also set up in the walking pathway to allow the subject to continue to observe the exoskeleton while it is walking. A second camera was used to capture the subject's left hip movement. The subject was then tasked with following a cued-online BCI decoding protocol, wherein alternating "IDLE" and "MOVE" commands were presented for the subject to follow. For each alternation, the "IDLE" or "MOVE" command was presented until 22 online segments were collected. For each run, the alternating commands would repeat until the full 30 m distance was traversed. A commercial acquisition system (Biopac MP150, Biopac Systems Inc, Goleta, CA) was used to capture the cue, the decoded state and stimulation voltage waveform. We repeated the protocol described here for 3 stimulation runs and 3 non-stimulation runs. In the non-stimulation runs, the ECoG leads for the stimulation channel were unplugged from the BCI, leaving the stimulation to output solely to the Biopac for recording. For the stimulation runs, the ECoG leads were plugged in to connect the subject's brain in parallel with the Biopac recording. All these data, as well as the motion capture kinematic data were then saved for later analysis.

5.2.8 BD-BCI Performance Evaluation

Using the data collected as described in the previous section, we sought to compare the relative performance of the BD-BCI with and without sensory feedback. Our aim was to demonstrate that performance would improve or remain the same while sensory feedback is being delivered to the subject. We characterized the BD-BCI performance by calculating

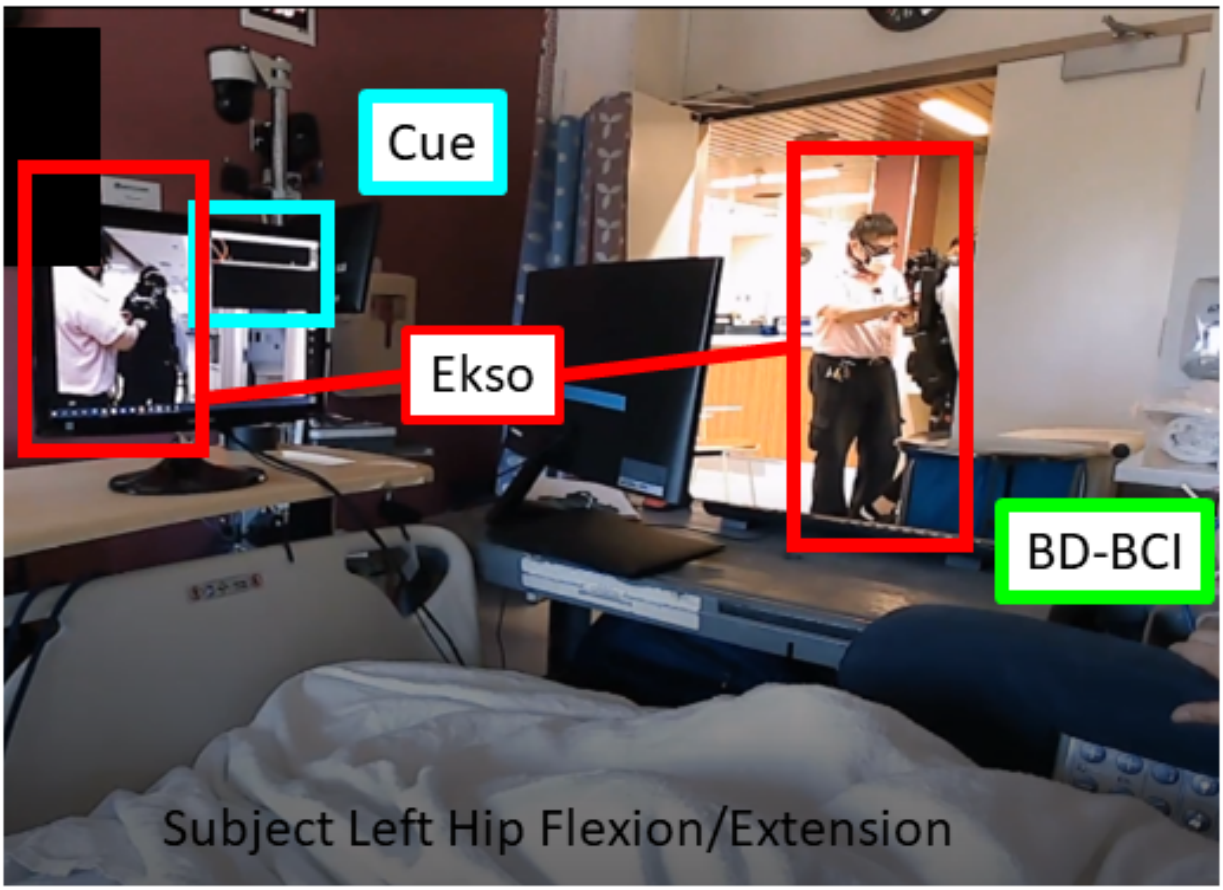

Figure 5.5: Setup of proxy-controlled exoskeleton BD-BCI with ECoG subject. The BD-BCI (not in picture) was placed on a table next to the subject's bed and the motor and sensory ECoG electrodes were plugged in (see Figure 5.6). The healthy experimenter wearing the exoskeleton and the exoskeleton operator were set up in the 30 m walking space outside the subject room. A monitor was placed in front of the subject to display the BCI cue, as well as video of the exoskeleton.

the decoded accuracy by comparing the decoded states to the displayed cues. The decoded accuracy was calculated by first segmenting the data for each run. We then appended the cue and decoded state data for both stimulation and non-stimulation conditions. By treating the displayed cue as the ground truth, we calculated the decoded accuracy by comparing the decoded state to the concurrent cue state. We then obtained the move state accuracy ($P(M|M)$ by calculating the proportion of correct move decoded states to the total number of move cue states. The same metric $P(I|I)$ was calculated for the idle states. Finally, the total decoding accuracy (P_{total}) was calculated as the proportion of correctly decoded states (comparing to the cue) to the total number of cues. These accuracies were calculated for both within-run and appended-run data.

5.3 Results

5.3.1 Motor and Sensory Electrode Selection

The MR-CT co-registered image (Appendix A) of the ECoG grid placed over the subject's right sensorimotor area is shown in Figure 5.6. Of the electrodes on the ECoG grid, we chose thirteen that exhibited $\mu - \beta$ and/or high-γ modulation in response to the left hip flexion/extension task. The choice of these electrodes was informed by inspection of the hospital system recorded data (Section 5.2.5). Representative time domain plots illustrating the modulations are shown in Figure 5.7.

From the channels mapped in the sensory mapping procedure, SMG41-49 was the sole channel exhibiting leg sensation (See Figure 5.6). The stimulation parameters chosen for this channel was a 1.4 mA current amplitude, 250 μs anodic/cathodic pulse width, and a 50 Hz pulse frequency. The subject reported a pressure sensation above their left knee in response to stimulation using these parameters. Using the sensory feedback channel in the step count-

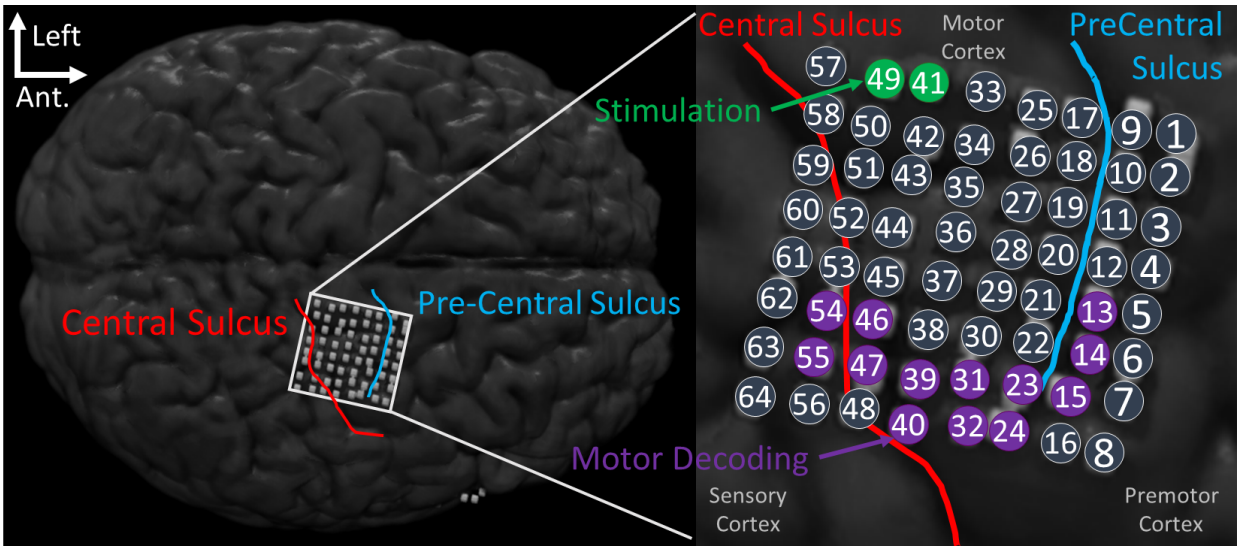

Figure 5.6: MR-CT co-registered images showing the placement of the ECoG sensorimotor grid (SMG) over a 3D brain render. (Left) Coronal view showing implantation location of the ECoG Grid. (Right) Zoomed view of the grid. The electrodes used for artificial stimulation feedback are colored green, and the electrodes used for motor decoding are colored purple.

ing test, the subject was able to consistently identify the number of steps in each trial, with an overall accuracy of 92.9%. Trial-by-trial step counting results are tabulated in Table 5.1.

5.3.2 BD-BCI Online Decoder Training and Parameters

Examples of the training data as recorded by the BD-BCI (See 5.2.5) are shown in Figure 5.8. The CPCA and LDA feature matrices for this training data are visualized in Figure 5.9. The μ - β modulation was evident across multiple recording electrodes, whereas the high-γ is more localized, specifically around SMG15. From the 10-fold cross validation analysis, we find that the collected training data had an idle state accuracy of 86.3±2.0% and a move state accuracy of 85.0±2.9%, leading to an overall accuracy of 85.6±1.6%. Based on the posteriors logged during the online decoding run, the decoding thresholds were chosen to be $T_i = 0.10$ and $T_m = 0.70$ to best separate the move and idle states (See Figure 5.10).

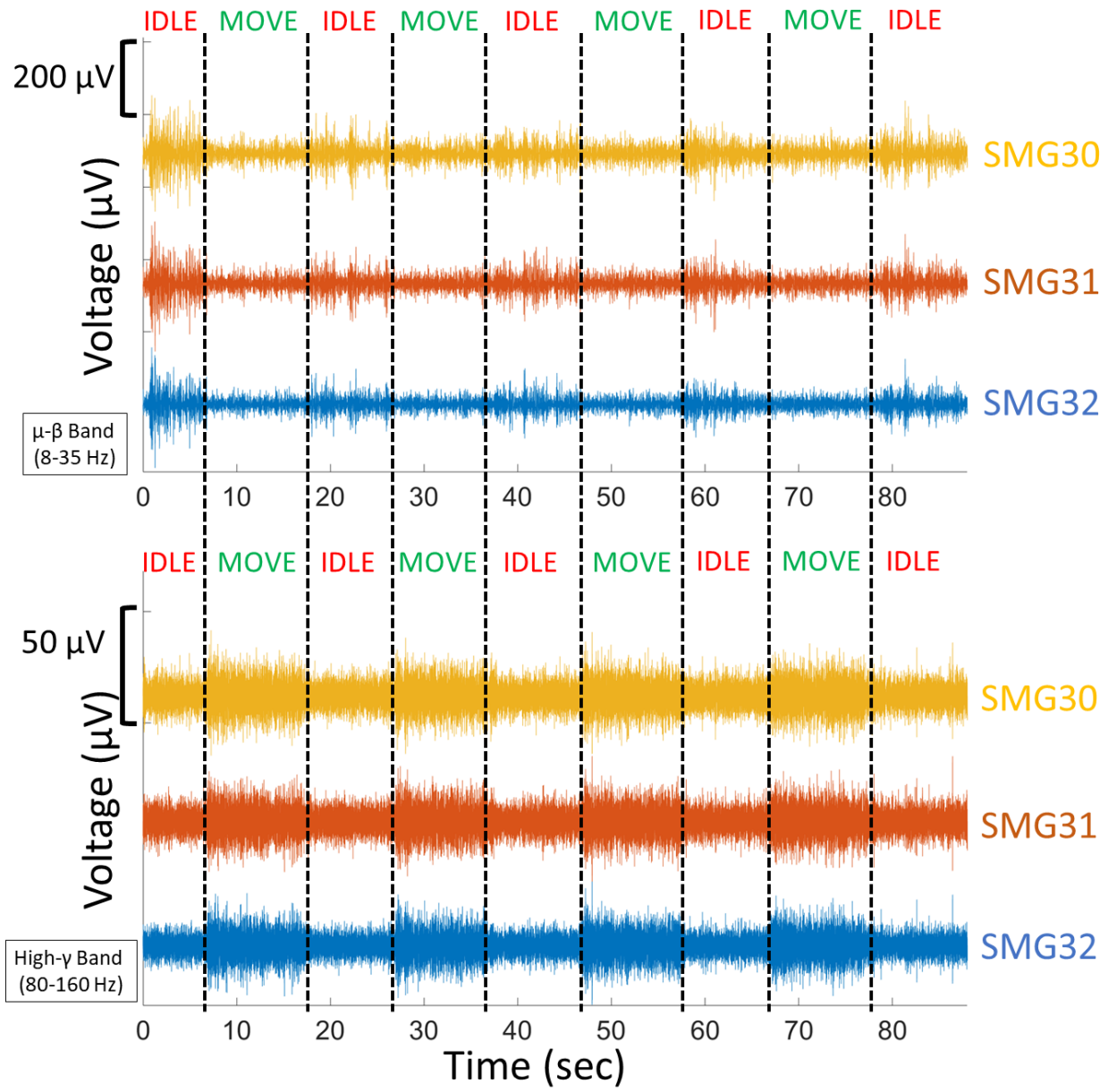

Figure 5.7: ECoG data from 3 representative electrodes exhibiting modulation in response to the motor task. This data was collected using the hospital acquisition system during left hip flexion/extension task. Top panel shows the data filtered to the $\mu - \beta$ band (8-35 Hz) while the bottom panel shows the same data filtered to the high-γ band (80-160 Hz). Move and idle state boundaries are marked with black dotted lines.

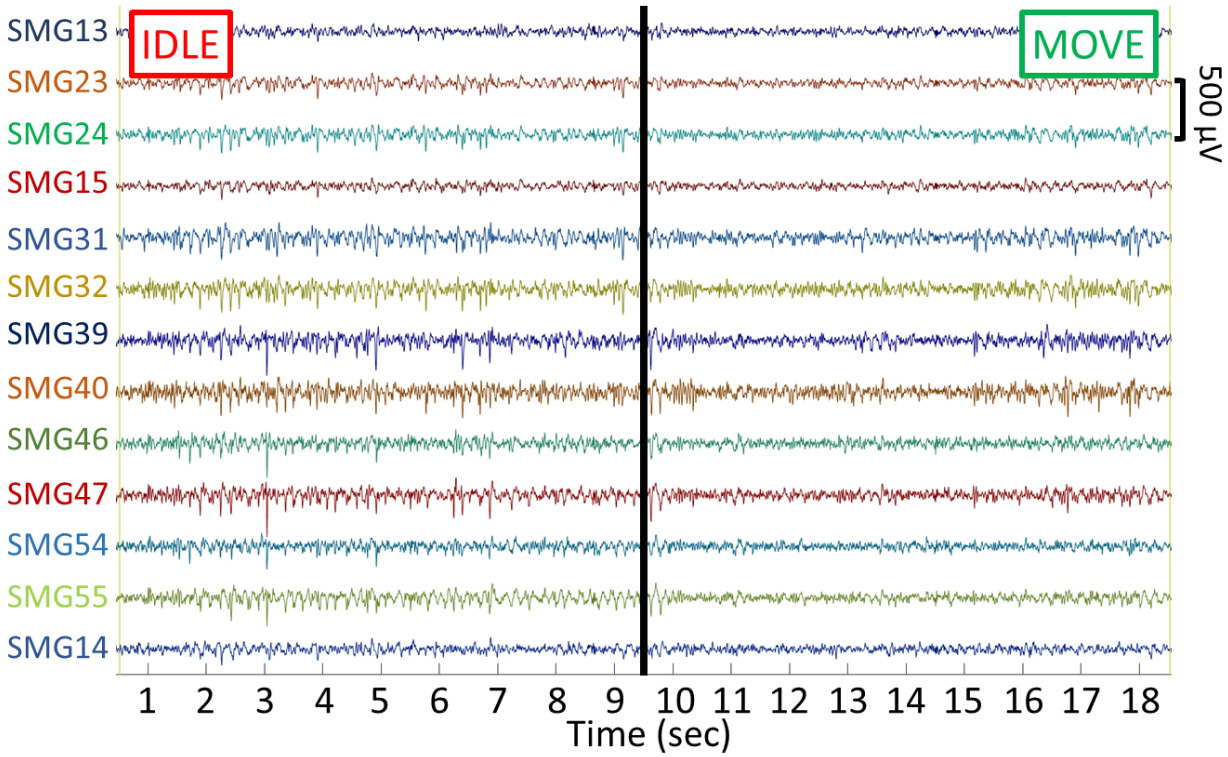

Figure 5.8: One idle epoch and one move epoch from the BD-BCI training data from the 13 channels used for online decoding. The $\mu - \beta$ oscillations are readily apparent in the idle state, particularly on SMG 31, SMG39 and SMG 40, which concurs with the generated feature map (cf. Figure 5.9.

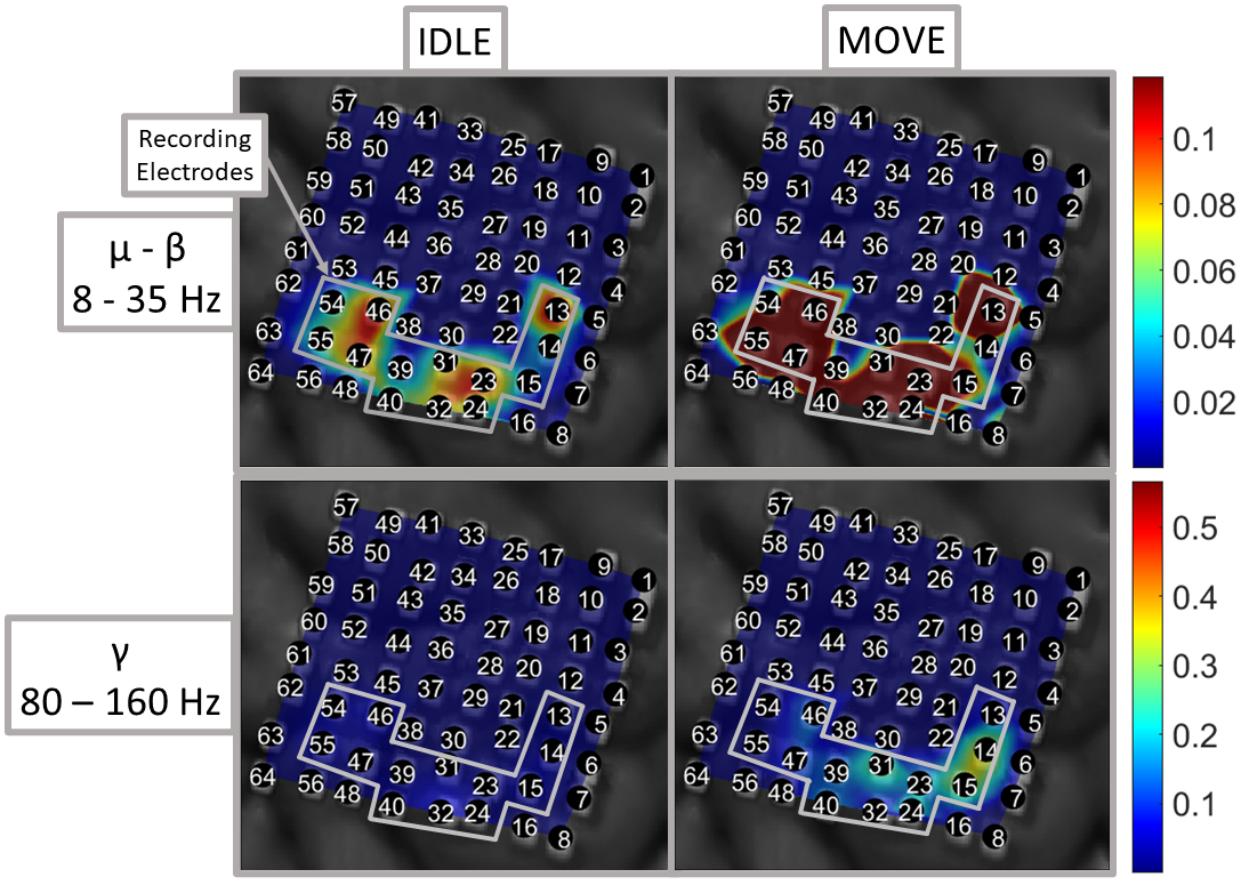

Figure 5.9: Combined CPCA and LDA feature matrices calculated for training data overlaid onto MR-CT co-registered images. Only those electrodes within the grey outline were plugged into the BD-BCI. Values for all other electrodes were set to zero as they did not contribute to the decoding. The weights corresponding to each electrode is shown for both the μ - β and γ bands, as well as for the idle and move states. Electrodes exhibiting higher feature weights are those that contribute more greatly to the state classification. high-γ features were more concentrated around SMG14-15, whereas μ - β features were more dispersed.

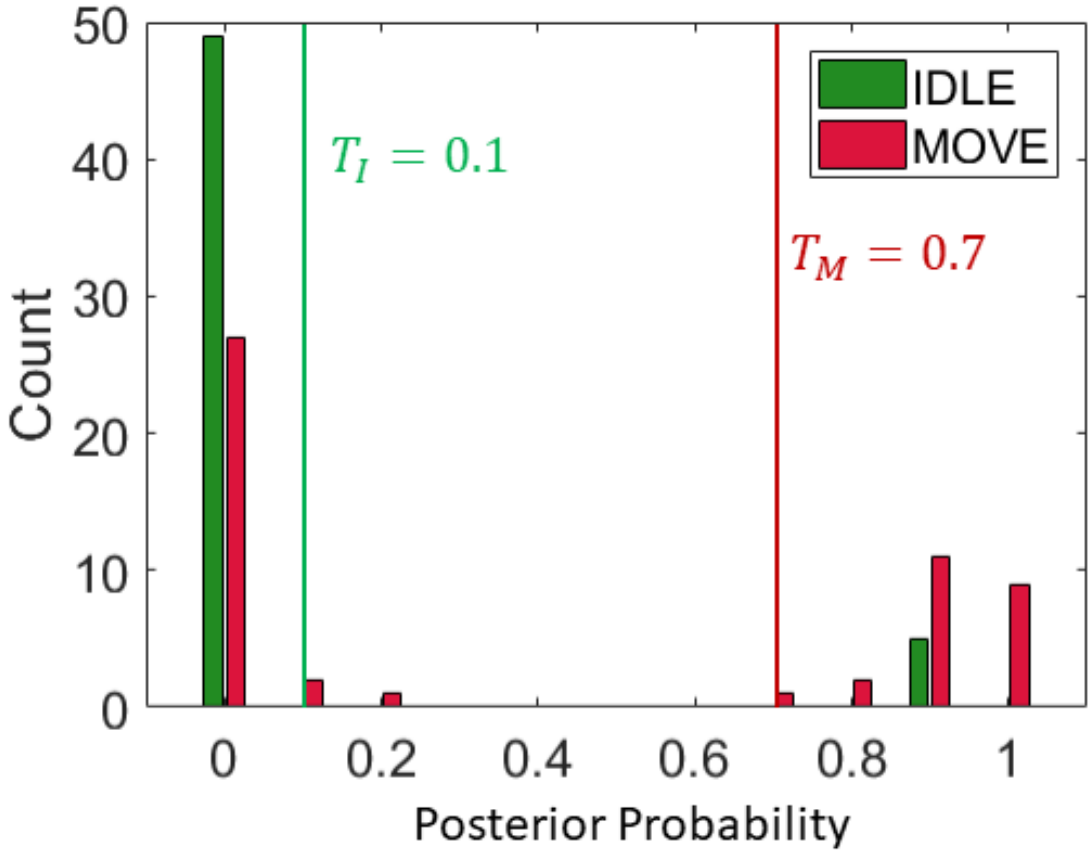

Figure 5.10: Histogram of posterior probabilities collected during an online decoding run. Posterior probabilities calculated during online BCI operation were logged and labeled with the concurrent cue state. The state transition thresholds, T_I and T_M were determined to best separate between move and idle states.

Trial #	Steps Taken	Steps Counted
1	3	2
2	2	2
3	8	7
4	2	2
5	4	5
6	7	7
7	4	3
8	8	8
9	5	4
10	8	8
11	5	4
12	5	5
13	6	6
14	6	4
Total	70	65
Accuracy	92.9%	

Table 5.1: Step Counting Experiment Results

5.3.3 Exoskeleton BD-BCI Demonstration and Evaluation

Using the chosen online BCI decoding parameters and the sensory feedback channel, the subject was able to successfully control the exoskeleton BD-BCI. An example of the cue state, decoded state, stimulation and kinematic data streams during a stimulation run are shown in Figure 5.11. Figure 5.12 shows a segment of ECoG data recorded by the BD-BCI during online decoding in a stimulation run. The online data verified the absence of stimulation artifacts in the recorded data and thus the success of the interleaved decoding paradigm. The cue and decoded states for the appended stimulation and non-stimulation runs are then shown in Figure 5.13. Generally, the decoded states followed the cue, with the primary exceptions being false move states identified during the idle state cue. The within-run and appended-run decoding accuracies for stimulation and non-stimulation runs were quantified in Table 5.2. Non-stimulation runs had a total decoding accuracy of 79.2% and stimulation runs having an accuracy of 74.7%, demonstrating that the sensory feedback

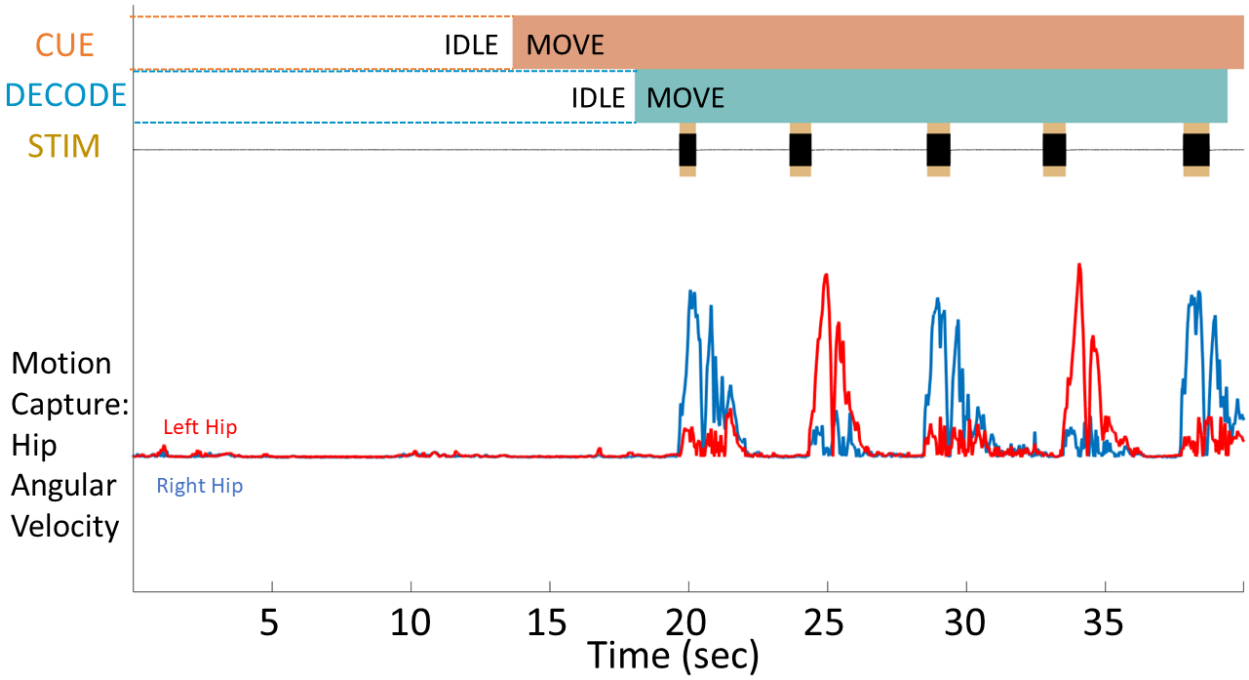

Figure 5.11: Data collected from a stimulation run during an idle to move state transition. Subject holds the idle state for 14 seconds. Cue state then changes from idle to move, and subject begins to move the left leg. Decoded state transitions to move, triggering the exoskeleton. Motion capture records exoskeleton movement, which triggers the stimulation. The tuning of the gyro thresholds caused the stimulation to trigger at different points in the gait cycle for the left and right legs.

was implemented without severely impacting the decoding accuracy.

5.4 Discussion

This work presents an exoskeleton BD-BCI system that was capable of motor intention decoding while intermittently delivering artificial sensory feedback. The sensory feedback was provided with only a 5% deterioration of the decoding performance of the BCI. Though the current results appear to indicate that the performance in non-stimulation runs is higher than stimulation runs, there was an insufficient number of runs to determine whether this performance difference was statistically significant. In theory, the control performance should

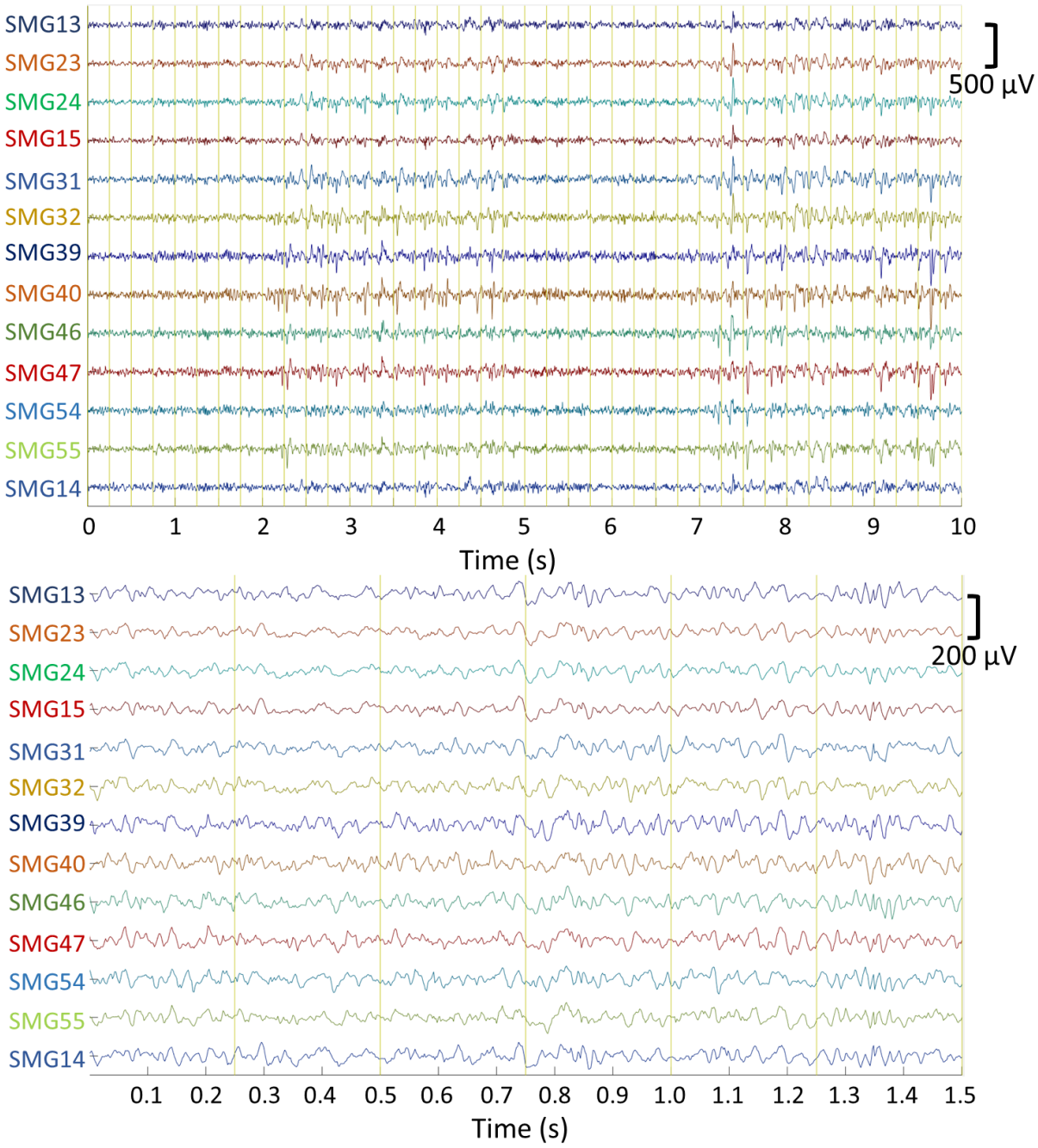

Figure 5.12: Appended online data windows collected during online BCI decoding with interleaved stimulation. Vertical yellow lines demarcate individual online segments. (Top) 10 seconds of online data. (Bottom) 1.5 seconds of online data (two online sliding windows). No stimulation artifacts are present in these data.

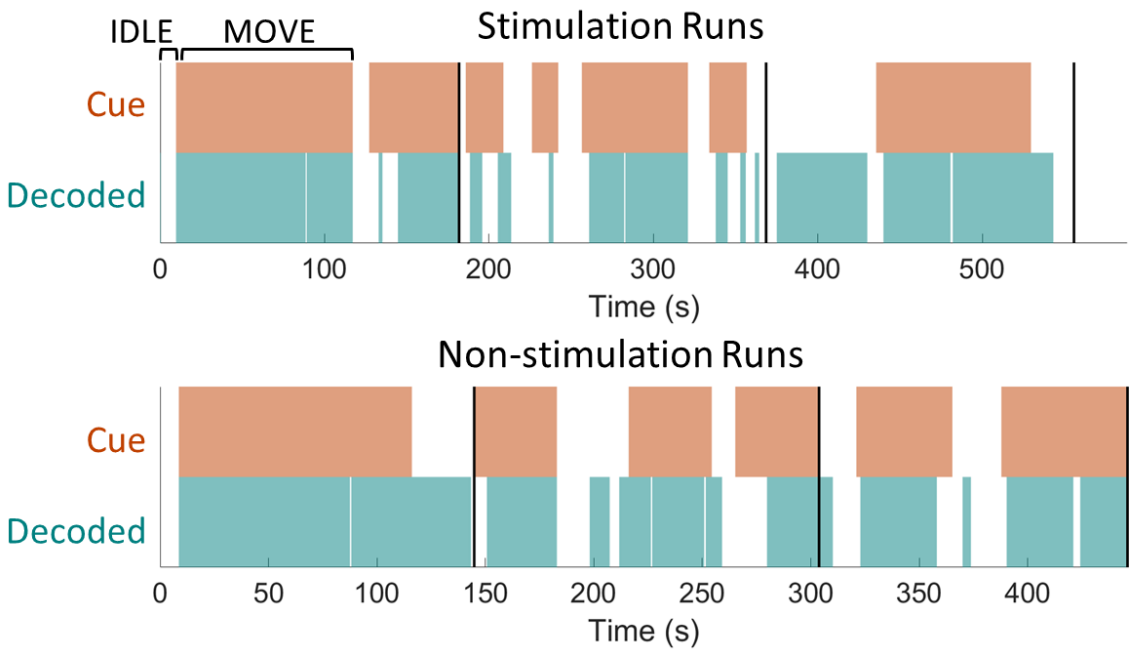

Figure 5.13: Cue and decoded states for appended stimulation and non-stimulation runs. Move states are indicated by the colored fill shapes, idle states are indicated by white sections. 3 runs were completed for each condition, delineated by the vertical black bars. Subject was generally able to maintain the move state when the "MOVE" cue is displayed, with some false move states occurring during "IDLE" cues.

	Stimulation			Non-stimulation		
Run #	$P_{\text{total}}(\%)$	$P(I\|I)$ (%)	$P(M\|M)$ (%)	P_{total} (%)	$P(I\|I)$ (%)	$P(M\|M)$ (%)
1	91.1	98.1	90.3	80.7	27.0	99.4
2	73.4	87.8	66.4	74.9	58.5	81.2
3	60.3	26.2	93.9	82.5	74.2	85.7
Total	74.7	60.3	80.7	79.2	64.0	83.7

Table 5.2: Decoded accuracies of stimulation and non-stimulation runs.

improve with sensory feedback [44], though this may only apply when the sensory feedback provides extra information for the behavioral task. This is true for reach-and-grasp upper-extremity tasks, where contact with the object is critical information. On the other hand, progression in the walking task is binary, and sensory feedback during the leg swing may not be expected to improve performance. Rather, we expect for this to be delivered without negatively impacting the decoding accuracy. The cases in which we observed poor decoding accuracy largely consisted of idling states wherein excessive move states were decoded. This phenomena was not exclusive to either condition, so we do not attribute it to the stimulation. We also note that due to the interleaving paradigm, decoding "move" will set the device to the move state for a disproportionately longer period of time compared to decoding "idle". This causes false move states to be more detrimental to decoding accuracy compared to false idle states.

We also note that there was a degradation in the performance compared to the ideal MATLAB-determined decoding accuracy (85%) in comparison to the online exoskeleton-interleaved performance (74.7% with stimulation, 79.2% without). This may be due to the relative complexities of the tasks, as the MATLAB-determined decoding accuracy is calculated using data collected during a simpler task, as well as it represents an ideal case scenario in which decoding is performed with no processing time or reaction delay. For the exoskeleton BD-BCI task, additional distractions such as watching the exoskeleton on the screen and receiving stimulation feedback may cause the performance to deteriorate. The absence of stimulation artifacts on recorded data (Figure 5.12) precludes electrical interference from the stimulator, however there is still a possibility underlying motor modulations were activated/suppressed by the stimulation. There was also a possibility that visual observation of the exoskeleton in movement was sufficient to cause desynchronization of $\mu - \beta$ oscillations [122].

A limitation to this study is that it is limited to the results of a single subject. Based on

the ECoG co-registration, the implantation for this subject was on the medial aspect of the lateral convexity of the motor cortex, where leg representation is sparse. Classically, leg motor activity would be best represented in the inter-hemispheric space, nevertheless we were still able to capture the hip movement task. It is possible that this decoding was driven primarily by $\mu - \beta$ modulations, as due to the placement of the ECoG grid, these could be triggered by either upper or lower extremity movement (e.g. subject grasping at the bed sides during leg movement or tensing of the upper body), even though the subject was instructed only to move the leg. The significance of our results are also limited by the few runs the subject was able to perform, making it difficult to compare results between stimulation and non-stimulation runs.

Benabid et. al [73] currently represents the state-of-the-art for invasive BCI control for a walking exoskeleton. The primary advantage of our work is that we implement sensory feedback in addition to walking intent decoding. On the other hand, Benabid et. al demonstrates a full body exoskeleton, as well as virtual control tasks and explores both upper and lower extremity BCI control. Additionally, their study places the subject directly in the exoskeleton, whereas ours utilizes proxy control. Our exoskeleton BD-BCI, however, was realized on an embedded system that abides by fully-implantable power constraints, whereas Benabid et. al utilizes a system that consists of bulky hardware that is mounted onto the exoskeleton. Over a span of two years, their subject managed to control the exoskeleton with a total decoding accuracy of 70.9%, whereas ours achieved a total decoding accuracy of 74.7% in stimulation runs over a period of a few days. As is the case with all BCI, there is an acclimation period for the subject to learn how to use the BCI, so it is likely that the performance for our system would only increase with more time. A noticeable observation in this regard is that our subject anecdotally reported the sensory feedback "like moving [their] own legs". It is possible that this associative learning could be reinforced with extended training, and could be utilized to teach paraplegic or tetraplegic individuals to replace lost sensory percepts with other surviving sensations.

Chapter 6

Conclusions and Future Work

In this dissertation, we have presented a thorough discussion of the problem of stimulation artifacts in BD-BCI, potential methodology for artifact suppression in real-time BD-BCI operation, as well as a demonstration of an actual BD-BCI device in an walking exoskeleton. We hope that the findings discussed herein serve to further BD-BCI technologies such that they can ultimately be used in the treatment and rehabilitation of motor conditions such as SCI-induced paraplegia or quadriplegia.

6.1 Artifact Propagation in Subdural Cortical Electrostimulation: Characterization and Modeling

The artifact characterization study has provided a comprehensive temporal, spectral and spatial analysis of cortical electrostimulation artifacts recorded subdurally by a grid of ECoG electrodes. We have also demonstrated that the spatial distribution of stimulation artifacts can be explained by a simple dipole model. These findings can help improve existing artifact suppression techniques, inspire the development of novel artifact mitigation methods, and

aid in the development of novel cortical stimulation protocols. Additionally, they may be useful for studies examining cortical functional tractography [123], cortico-cortical evoked potentials for clinical applications [124], and source localization for noninvasive functional neuroimaging [125].

The same characterization performed in this study can be performed for MEA stimulation. Though the underlying electrical properties likely remain the same between both modalities, there may be differences in artifact propagation in ECoG and MEAs, owing primarily to the difference in electrode geometry. While the analyses presented in this study were time invariant, the full time-frequency response of the artifact could potentially be modeled using a dynamical systems approach. The ECoG array could be treated as a multiple-input multiple-output (MIMO) system, with the stimulation channel acting as the input and the remainder of the channels as the output. A transfer function could be defined for such a system, which would give a more precise model for stimulation artifact propagation. Though the current data do not sample at a high enough frequency to capture the full response of the stimulation pulse (200-250 μs pulsewidth versus $\sim$20 ms sampling period), it does provide a similar response to what would be seen on fully-implantable BCI as these devices would have a limited sampling rate due to computational and power restrictions. Ultimately, the analyses in this work and the proposed work could both be applied to higher sample rate data to generate a more precise understanding of the propagation of subdural artifacts. In general, the results in our existing work deepen our understanding of cortical electrostimulation and could provide critical design specifications for future BD-BCI systems.

6.2 Front-End Artifact Suppression: Dipole Cancellation

The results from our dipole cancellation study suggest that it could potentially ward against stimulation artifacts in BD-BCI applications. The amplitude of the cancellation stimulation required to prevent saturation is only a fraction of the primary stimulation. Though higher amplitude cancellation can be used to more aggressively suppress artifacts, this would come at the cost of greater power expenditure, as well as greater risk of desensitization. Regardless, even

Our group has subsequently continued to develop the dipole cancellation technique. An optimization framework [59] has been developed to pre-determine the placement of the auxiliary dipole given the locations of stimulation and recording sites in a simulated BD-BCI scenario. We have also extended the idea from dipole cancellation to full multipolar cancellation. Building upon the ideas from our artifact characterization studies, we use multiplexed stimulators to shape the potential field of the stimulation artifacts, giving us a greater degree of control over the artifact suppression. We have implemented this feature into our BD-BCI [96] and initial tests in brain phantoms support the theory of multipolar artifact suppression. Additionally, other work from our group [95] has also implemented multipolar cancellation functionalities on a CMOS chip. Future work will continue testing on this functionality for potential incorporation into our Bd-BCI protocol.

6.3 Back-End Artifact Suppression: Pre-whitening and Null Projection

In this work, we present a back-end artifact suppression method based on pre-whitening and null projection techniques (PWNP). We demonstrate its effectiveness in suppressing stimulation artifacts across a variety of data, including EEG, ECoG and MEA data. The suppression results from applying the PWNP method to these data typically surpasses those of an state-of-the-art ICA-based methodolgy. The PWNP method more greatly mitigates artifacts while selectively preserving neuro-physiological features, like α modulations and action potentials. These results, in addition to an implementation that is more amenable to real-time operation, suggest that the PWNP method could potentially be used to enable simultaneous stimulation recording in bi-directional brain computer interfaces.

As was mentioned in Section 4.4, our current efforts are directed towards a real-time implementation of the PWNP method. This will consist firstly of pseudo-real-time N-fold cross validation analyses to assess whether the results observed in the existing study translate to real-time performance. We will then develop an implementation that can be uploaded to the BD-BCI device. This will require a protocol to acquire training data with examples of stimulation and baseline conditions. The pre-whitening and null projection matrices will then need to be generated and saved for online use. The performance of the online PWNP algorithm will then need to be tested with actual subdural stimulation a separate study.

6.4 Demonstration of Walking Exoskeleton BD-BCI

Herein, we have described an implementation of an embedded system BD-BCI integrated with a robotic leg exoskeleton. Using this exoskeleton BD-BCI, a single subject enacted con-

trol over the walking function of the exoskeleton using ECoG signals, while simultaneously receiving sensory feedback in the form of subdural cortical electrostimulation. The performance of our system (74.7%) was similar to the current state-of-the-art (70.9%) for BD-BCI exoskeleton systems, while making advances in the technology with regards to portability and implantability. Thus, this device serves as a prototype for a fully implantable BD-BCI system, capable of restoring motor and sensory walking functions in paraplegics and tetraplegics.

Further improvements and upgrades are currently under development for the BD-BCI walking exoskeleton system. Firstly, we have implemented software and hardware updates to support multiple stimulation outputs. This would allow for a different sensory percept to be triggered by each leg of the exoskeleton. In theory, for a subject with sensory coverage on both leg sensory areas (i.e. via bilateral electrodes placed in the inter-hemispheric fissure), it would be possible to elicit both left and right leg sensations when the ipsilateral exoskeleton leg is in swing. This capability could be further extended to include sensory feedback for stance phases on each leg, for a total of 4 sets of stimulation parameters being utilized simultaneously. This feedback paradigm would give the subject continuous information about the exoskeleton gait cycle, which could be especially useful for future studies in which the subject is placed inside of the exoskeleton. Meanwhile, work is continuing on preparing the BD-BCI for implantation, as others in our group have produced miniaturized versions of the front-end [126, 127, 128, 129], transceiver [130, 131], and stimulator [95, 129] in CMOS processes. The results shown here hopefully provide evidence to justify the implantation of a future version of the BD-BCI device into a paraplegic or tetraplegic subject.

Bibliography

[1] Michael R Neuman et al. Biopotential electrodes. In *Medical instrumentation: application and design*, volume 4, pages 189–240. Wiley New York, 1998.

[2] Jeffrey Lim, Po T Wang, Alireza K Bidhendi, Omid M Arasteh, Susan J Shaw, Michelle Armacost, Hui Gong, Charles Y Liu, Payam Heydari, An H Do, et al. Characterization of stimulation artifact behavior in simultaneous electrocorticography grid stimulation and recording. In *2018 40th Annual International Conference of the IEEE Engineering in Medicine and Biology Society (EMBC)*, pages 4748–4751. IEEE, 2018.

[3] Jeffrey Lim, Po T Wang, Haoran Pu, Charles Y Liu, Spencer Kellis, Richard A Andersen, Payam Heydari, An H Do, and Zoran Nenadic. Dipole cancellation as an artifact suppression technique in simultaneous electrocorticography stimulation and recording. In *2019 9th International IEEE/EMBS Conference on Neural Engineering (NER)*, pages 725–729. IEEE, 2019.

[4] Jeffrey Lim, Po T Wang, Susan J Shaw, Michelle Armacost, Hui Gong, Charles Y Liu, An H Do, Payam Heydari, and Zoran Nenadic. Pre-whitening and null projection as an artifact suppression method for electrocorticography stimulation in bi-directional brain computer interfaces. In *2020 42nd Annual International Conference of the IEEE Engineering in Medicine & Biology Society (EMBC)*, pages 3493–3496. IEEE, 2020.

[5] Jeffrey Lim, Po T Wang, Susan J Shaw, Hui Gong, Michelle Armacost, Charles Y Liu, An H Do, Payam Heydari, and Zoran Nenadic. Artifact propagation in subdural cortical electrostimulation: Characterization and modeling. *Frontiers in Neuroscience*, 16, 2022.

[6] Ujwal Chaudhary, Niels Birbaumer, and Ander Ramos-Murguialday. Brain–computer interfaces for communication and rehabilitation. *Nature Reviews Neurology*, 12(9):513–525, 2016.

[7] Jonathan R Wolpaw, Niels Birbaumer, William J Heetderks, Dennis J McFarland, P Hunter Peckham, Gerwin Schalk, Emanuel Donchin, Louis A Quatrano, Charles J Robinson, Theresa M Vaughan, et al. Brain-computer interface technology: a review of the first international meeting. *IEEE transactions on rehabilitation engineering*, 8(2):164–173, 2000.

[8] Guido Dornhege, Jose del R Millan, Thilo Hinterberger, Dennis J McFarland, and Klaus-Robert Müller. *Toward brain-computer interfacing*. MIT press, 2007.

[9] Marcel Van Gerven, Jason Farquhar, Rebecca Schaefer, Rutger Vlek, Jeroen Geuze, Anton Nijholt, Nick Ramsey, Pim Haselager, Louis Vuurpijl, Stan Gielen, et al. The brain–computer interface cycle. *Journal of neural engineering*, 6(4):041001, 2009.

[10] Bruce J Fisch and Rainer Spehlmann. *Fisch and Spehlmann's EEG primer: basic principles of digital and analog EEG*. Elsevier Health Sciences, 1999.

[11] Gert Pfurtscheller. Eeg event-related desynchronization (erd) and synchronization (ers). *Electroencephalography and Clinical Neurophysiology*, 1(103):26, 1997.

[12] Hans Berger. Electroencephalogram of humans. *Journal fur Psychologie und Neurologie*, 40:160–179, 1930.

[13] Lawrence Ashley Farwell and Emanuel Donchin. Talking off the top of your head: toward a mental prosthesis utilizing event-related brain potentials. *Electroencephalography and clinical Neurophysiology*, 70(6):510–523, 1988.

[14] Dean J Krusienski, Eric W Sellers, Dennis J McFarland, Theresa M Vaughan, and Jonathan R Wolpaw. Toward enhanced p300 speller performance. *Journal of neuroscience methods*, 167(1):15–21, 2008.

[15] Niels Birbaumer, Nimr Ghanayim, Thilo Hinterberger, Iver Iversen, Boris Kotchoubey, Andrea Kübler, Juri Perelmouter, Edward Taub, and Herta Flor. A spelling device for the paralysed. *Nature*, 398(6725):297–298, 1999.

[16] Femke Nijboer, EW Sellers, Jürgen Mellinger, Mary Ann Jordan, Tamara Matuz, Adrian Furdea, Sebastian Halder, Ursula Mochty, DJ Krusienski, TM Vaughan, et al. A p300-based brain–computer interface for people with amyotrophic lateral sclerosis. *Clinical neurophysiology*, 119(8):1909–1916, 2008.

[17] Ravikiran Mane, Tushar Chouhan, and Cuntai Guan. Bci for stroke rehabilitation: motor and beyond. *Journal of neural engineering*, 17(4):041001, 2020.

[18] Christine E King, Po T Wang, Colin M McCrimmon, Cathy CY Chou, An H Do, and Zoran Nenadic. The feasibility of a brain-computer interface functional electrical stimulation system for the restoration of overground walking after paraplegia. *Journal of neuroengineering and rehabilitation*, 12(1):1–11, 2015.

[19] Kai Keng Ang, Cuntai Guan, Karen Sui Geok Chua, Beng Ti Ang, Christopher Kuah, Chuanchu Wang, Kok Soon Phua, Zheng Yang Chin, and Haihong Zhang. A clinical study of motor imagery-based brain-computer interface for upper limb robotic rehabilitation. In *2009 annual international conference of the IEEE engineering in medicine and biology society*, pages 5981–5984. IEEE, 2009.

[20] Christine E King, Po T Wang, Luis A Chui, An H Do, and Zoran Nenadic. Operation of a brain-computer interface walking simulator for individuals with spinal cord injury. *Journal of neuroengineering and rehabilitation*, 10:1–14, 2013.

[21] Gerwin Schalk and Eric C Leuthardt. Brain-computer interfaces using electrocorticographic signals. *IEEE reviews in biomedical engineering*, 4:140–154, 2011.

[22] Ernst Niedermeyer and FH Lopes da Silva. *Electroencephalography: basic principles, clinical applications, and related fields*. Lippincott Williams & Wilkins, 2005.

[23] Thomas C Ferree, MT Clay, and Don M Tucker. The spatial resolution of scalp eeg. *Neurocomputing*, 38:1209–1216, 2001.

[24] Emily M Mugler, James L Patton, Robert D Flint, Zachary A Wright, Stephan U Schuele, Joshua Rosenow, Jerry J Shih, Dean J Krusienski, and Marc W Slutzky. Direct classification of all american english phonemes using signals from functional speech motor cortex. *Journal of neural engineering*, 11(3):035015, 2014.

[25] Po T Wang, Colin M McCrimmon, Christine E King, Susan J Shaw, David E Millett, Hui Gong, Luis A Chui, Charles Y Liu, Zoran Nenadic, and An H Do. Characterization of electrocorticogram high-gamma signal in response to varying upper extremity movement velocity. *Brain Structure and Function*, 222(8):3705–3748, 2017.

[26] Colin M McCrimmon, Po T Wang, Payam Heydari, Angelica Nguyen, Susan J Shaw, Hui Gong, Luis A Chui, Charles Y Liu, Zoran Nenadic, and An H Do. Electrocorticographic encoding of human gait in the leg primary motor cortex. *Cerebral Cortex*, 28(8):2752–2762, 2018.

[27] Wei Wang, Alan D Degenhart, Jennifer L Collinger, Ramana Vinjamuri, Gustavo P Sudre, P David Adelson, Deborah L Holder, Eric C Leuthardt, Daniel W Moran, Michael L Boninger, et al. Human motor cortical activity recorded with micro-ecog electrodes, during individual finger movements. In *2009 Annual International Conference of the IEEE Engineering in Medicine and Biology Society*, pages 586–589. IEEE, 2009.

[28] Leah Muller, Liberty S Hamilton, Erik Edwards, Kristofer E Bouchard, and Edward F Chang. Spatial resolution dependence on spectral frequency in human speech cortex electrocorticography. *Journal of neural engineering*, 13(5):056013, 2016.

[29] Po T Wang, Christine E King, Colin M McCrimmon, Jack J Lin, Mona Sazgar, Frank PK Hsu, Susan J Shaw, David E Millet, Luis A Chui, Charles Y Liu, et al. Comparison of decoding resolution of standard and high-density electrocorticogram electrodes. *Journal of neural engineering*, 13(2):026016, 2016.

[30] Marie Engelene J Obien, Kosmas Deligkaris, Torsten Bullmann, Douglas J Bakkum, and Urs Frey. Revealing neuronal function through microelectrode array recordings. *Frontiers in neuroscience*, 8:423, 2015.

[31] Eric C Leuthardt, Gerwin Schalk, Jonathan R Wolpaw, Jeffrey G Ojemann, and Daniel W Moran. A brain–computer interface using electrocorticographic signals in humans. *Journal of neural engineering*, 1(2):63, 2004.

[32] Wei Wang, Jennifer L Collinger, Alan D Degenhart, Elizabeth C Tyler-Kabara, Andrew B Schwartz, Daniel W Moran, Douglas J Weber, Brian Wodlinger, Ramana K Vinjamuri, Robin C Ashmore, et al. An electrocorticographic brain interface in an individual with tetraplegia. *PloS One*, 8(2):e55344, 2013.

[33] Matthew S Fifer, Guy Hotson, Brock A Wester, David P McMullen, Yujing Wang, Matthew S Johannes, Kapil D Katyal, John B Helder, Matthew P Para, R Jacob Vogelstein, et al. Simultaneous neural control of simple reaching and grasping with the modular prosthetic limb using intracranial eeg. *IEEE transactions on neural systems and rehabilitation engineering*, 22(3):695–705, 2013.

[34] David T Bundy, Lauren Souders, Kelly Baranyai, Laura Leonard, Gerwin Schalk, Robert Coker, Daniel W Moran, Thy Huskey, and Eric C Leuthardt. Contralesional brain–computer interface control of a powered exoskeleton for motor recovery in chronic stroke survivors. *Stroke*, 48(7):1908–1915, 2017.

[35] Jennifer L Collinger, Brian Wodlinger, John E Downey, Wei Wang, Elizabeth C Tyler-Kabara, Douglas J Weber, Angus JC McMorland, Meel Velliste, Michael L Boninger, and Andrew B Schwartz. High-performance neuroprosthetic control by an individual with tetraplegia. *The Lancet*, 381(9866):557–564, 2013.

[36] Leigh R Hochberg, Daniel Bacher, Beata Jarosiewicz, Nicolas Y Masse, John D Simeral, Joern Vogel, Sami Haddadin, Jie Liu, Sydney S Cash, Patrick Van Der Smagt, et al. Reach and grasp by people with tetraplegia using a neurally controlled robotic arm. *Nature*, 485(7398):372–375, 2012.

[37] A Bolu Ajiboye, Francis R Willett, Daniel R Young, William D Memberg, Brian A Murphy, Jonathan P Miller, Benjamin L Walter, Jennifer A Sweet, Harry A Hoyen, Michael W Keith, et al. Restoration of reaching and grasping movements through brain-controlled muscle stimulation in a person with tetraplegia: a proof-of-concept demonstration. *The Lancet*, 389(10081):1821–1830, 2017.

[38] Mariska J Vansteensel, Elmar GM Pels, Martin G Bleichner, Mariana P Branco, Timothy Denison, Zachary V Freudenburg, Peter Gosselaar, Sacha Leinders, Thomas H Ottens, Max A Van Den Boom, et al. Fully implanted brain–computer interface in a locked-in patient with als. *New England Journal of Medicine*, 375(21):2060–2066, 2016.

[39] Brandy B Ma and Vikram R Rao. Responsive neurostimulation: candidates and considerations. *Epilepsy & Behavior*, 88:388–395, 2018.

[40] Tara L Skarpaas, Beata Jarosiewicz, and Martha J Morrell. Brain-responsive neurostimulation for epilepsy (rns® system). *Epilepsy research*, 153:68–70, 2019.

[41] Roland S Johansson, Charlotte Häger, and Lars Bäckström. Somatosensory control of precision grip during unpredictable pulling loads: Iii. impairments during digital anesthesia. *Experimental brain research*, 89:204–213, 1992.

[42] Joël Monzée, Yves Lamarre, and Allan M Smith. The effects of digital anesthesia on force control using a precision grip. *Journal of neurophysiology*, 89(2):672–683, 2003.

[43] Ayman M Ebied, Graham J Kemp, and Simon P Frostick. The role of cutaneous sensation in the motor function of the hand. *Journal of Orthopaedic Research*, 22(4):862–866, 2004.

[44] Sharlene Flesher, John Downey, Jennifer Collinger, Stephen Foldes, Jeffrey Weiss, Elizabeth Tyler-Kabara, Sliman Bensmaia, Andrew Schwartz, Michael Boninger, and Robert Gaunt. Intracortical microstimulation as a feedback source for brain-computer interface users. *Brain-Computer Interface Research: A State-of-the-Art Summary 6*, pages 43–54, 2017.

[45] Francesco Clemente, Giacomo Valle, Marco Controzzi, Ivo Strauss, Francesco Iberite, Thomas Stieglitz, Giuseppe Granata, Paolo M Rossini, Francesco Petrini, Silvestro Micera, et al. Intraneural sensory feedback restores grip force control and motor coordination while using a prosthetic hand. *Journal of neural engineering*, 16(2):026034, 2019.

[46] Robert W Mann and Stephen D Reimers. Kinesthetic sensing for the emg controlled" boston arm". *IEEE Transactions on Man-Machine Systems*, 11(1):110–115, 1970.

[47] Th W Beeker, J During, and A Den Hertog. Artificial touch in a hand-prosthesis. *Medical and biological engineering*, 5(1):47–49, 1967.

[48] Svenja Borchers, Marc Himmelbach, Nikos Logothetis, and Hans-Otto Karnath. Direct electrical stimulation of human cortex—the gold standard for mapping brain functions? *Nature Reviews Neuroscience*, 13(1):63–70, 2012.

[49] Wilder Penfield and Edwin Boldrey. Somatic motor and sensory representation in the cerebral cortex of man as studied by electrical stimulation. *Brain*, 60(4):389–443, 1937.

[50] Lise A Johnson, Jeremiah D Wander, Devapratim Sarma, David K Su, Eberhard E Fetz, and Jeffrey G Ojemann. Direct electrical stimulation of the somatosensory cortex in humans using electrocorticography electrodes: a qualitative and quantitative report. *Journal of neural engineering*, 10(3):036021, 2013.

[51] Shivayogi V Hiremath, Elizabeth C Tyler-Kabara, Jesse J Wheeler, Daniel W Moran, Robert A Gaunt, Jennifer L Collinger, Stephen T Foldes, Douglas J Weber, Weidong Chen, Michael L Boninger, et al. Human perception of electrical stimulation on the surface of somatosensory cortex. *PLoS One*, 12(5):e0176020, 2017.

[52] Brian Lee, Daniel Kramer, Michelle Armenta Salas, Spencer Kellis, David Brown, Tatyana Dobreva, Christian Klaes, Christi Heck, Charles Liu, and Richard A Andersen. Engineering artificial somatosensation through cortical stimulation in humans. *Frontiers in Systems Neuroscience*, 12:24, 2018.

[53] Michelle Armenta Salas, Luke Bashford, Spencer Kellis, Matiar Jafari, HyeongChan Jo, Daniel Kramer, Kathleen Shanfield, Kelsie Pejsa, Brian Lee, Charles Y Liu, et al. Proprioceptive and cutaneous sensations in humans elicited by intracortical microstimulation. *Elife*, 7:e32904, 2018.

[54] Matthew S Fifer, David P McMullen, Tessy M Thomas, Luke Osborn, Robert W Nickl, Daniel N Candrea, Eric A Pohlmeyer, Margaret C Thompson, Manuel Anaya, Wouter Schellekens, et al. Intracortical microstimulation elicits human fingertip sensations. *MedRxiv*, pages 2020–05, 2020.

[55] Adam G Rouse, Scott R Stanslaski, Peng Cong, Randy M Jensen, Pedram Afshar, Dave Ullestad, Rahul Gupta, Gregory F Molnar, Daniel W Moran, and Timothy J Denison. A chronic generalized bi-directional brain–machine interface. *Journal of Neural Engineering*, 8(3):036018, 2011.

[56] Scott Stanslaski, Peng Cong, Dave Carlson, Wes Santa, Randy Jensen, Greg Molnar, William J Marks, Afsah Shafquat, and Tim Denison. An implantable bi-directional brain-machine interface system for chronic neuroprosthesis research. In *2009 Annual International Conference of the IEEE Engineering in Medicine and Biology Society*, pages 5494–5497. IEEE, 2009.

[57] Wenlong Jiang, Vahagn Hokhikyan, Hariprasad Chandrakumar, Vaibhav Karkare, and Dejan Marković. A±50-mv linear-input-range vco-based neural-recording front-end with digital nonlinearity correction. *IEEE Journal of Solid-State Circuits*, 52(1):173–184, 2016.

[58] Hariprasad Chandrakumar and Dejan Marković. A high dynamic-range neural recording chopper amplifier for simultaneous neural recording and stimulation. *IEEE Journal of Solid-State Circuits*, 52(3):645–656, 2017.

[59] Haoran Pu, Jeffrey Lim, Spencer Kellis, Charles Y Liu, Richard A Andersen, An H Do, Payam Heydari, and Zoran Nenadic. Optimal artifact suppression in simultaneous electrocorticography stimulation and recording for bi-directional brain-computer interface applications. *Journal of neural engineering*, 17(2):026038, 2020.

[60] Adam E Mendrela, Jihyun Cho, Jeffrey A Fredenburg, Vivek Nagaraj, Theoden I Netoff, Michael P Flynn, and Euisik Yoon. A bidirectional neural interface circuit with active stimulation artifact cancellation and cross-channel common-mode noise suppression. *IEEE Journal of Solid-State Circuits*, 51(4):955–965, 2016.

[61] Kanokwan Limnuson, Hui Lu, Hillel J Chiel, and Pedram Mohseni. Real-time stimulus artifact rejection via template subtraction. *IEEE transactions on biomedical circuits and systems*, 8(3):391–400, 2013.

[62] Erwin B Montgomery Jr, John T Gale, and He Huang. Methods for isolating extracellular action potentials and removing stimulus artifacts from microelectrode recordings of neurons requiring minimal operator intervention. *Journal of neuroscience methods*, 144(1):107–125, 2005.

[63] Andy Zhou, Samantha R Santacruz, Benjamin C Johnson, George Alexandrov, Ali Moin, Fred L Burghardt, Jan M Rabaey, Jose M Carmena, and Rikky Muller. Wand: A 128-channel, closed-loop, wireless artifact-free neuromodulation device. *arXiv preprint arXiv:1708.00556*, 2017.

[64] Leon F Heffer and James B Fallon. A novel stimulus artifact removal technique for high-rate electrical stimulation. *Journal of neuroscience methods*, 170(2):277–284, 2008.

[65] Colin Waddell, Judith A Pratt, Bernd Porr, and Samuel Ewing. Deep brain stimulation artifact removal through under-sampling and cubic-spline interpolation. In *2009 2nd International Congress on Image and Signal Processing*, pages 1–5. IEEE, 2009.

[66] Takao Hashimoto, Christopher M Elder, and Jerrold L Vitek. A template subtraction method for stimulus artifact removal in high-frequency deep brain stimulation. *Journal of neuroscience methods*, 113(2):181–186, 2002.

[67] Thomas Wichmann. A digital averaging method for removal of stimulus artifacts in neurophysiologic experiments. *Journal of neuroscience methods*, 98(1):57–62, 2000.

[68] Janis Hofmanis, Ricardo A Salido Ruiz, Olivier Caspary, Radu Ranta, and Valérie Louis-Dorr. Extraction of deep brain stimulation (dbs) source in seeg using emd and ica. In *2011 Annual International Conference of the IEEE Engineering in Medicine and Biology Society*, pages 834–837. IEEE, 2011.

[69] Tzyy-Ping Jung, Scott Makeig, Marissa Westerfield, Jeanne Townsend, Eric Courchesne, and Terrence J Sejnowski. Removal of eye activity artifacts from visual event-related potentials in normal and clinical subjects. *Clinical Neurophysiology*, 111(10):1745–1758, 2000.

[70] Tarik Al-ani, Fanny Cazettes, Stéphane Palfi, and Jean-Pascal Lefaucheur. Automatic removal of high-amplitude stimulus artefact from neuronal signal recorded in the subthalamic nucleus. *Journal of neuroscience methods*, 198(1):135–146, 2011.

[71] Ke Zeng, Dan Chen, Gaoxiang Ouyang, Lizhe Wang, Xianzeng Liu, and Xiaoli Li. An eemd-ica approach to enhancing artifact rejection for noisy multivariate neural data. *IEEE transactions on neural systems and rehabilitation engineering*, 24(6):630–638, 2015.

[72] Joseph E O'Doherty, Mikhail A Lebedev, Peter J Ifft, Katie Z Zhuang, Solaiman Shokur, Hannes Bleuler, and Miguel AL Nicolelis. Active tactile exploration using a brain–machine–brain interface. *Nature*, 479(7372):228–231, 2011.

[73] Alim Louis Benabid, Thomas Costecalde, Andrey Eliseyev, Guillaume Charvet, Alexandre Verney, Serpil Karakas, Michael Foerster, Aurélien Lambert, Boris Morinière, Neil Abroug, et al. An exoskeleton controlled by an epidural wireless brain–machine interface in a tetraplegic patient: a proof-of-concept demonstration. *The Lancet Neurology*, 18(12):1112–1122, 2019.

[74] Charles C Wood. Application of dipole localization methods to source identification of human evoked potentials. *Annals of the New York Academy of Sciences*, 388(1):139–155, 1982.

[75] Michael Scherg. Fundamentals of dipole source potential analysis. *Auditory Evoked Magnetic Fields and Electric Potentials. Advances in Audiology*, 6(40-69):25, 1990.

[76] Paul Boon, Michel D'Havé, C Adam, Kristl Vonck, Michel Baulac, Tom Vandekerckhove, and J De Reuck. Dipole modeling in epilepsy surgery candidates. *Epilepsia*, 38(2):208–218, 1997.

[77] William W Sutherling, Massoud Akhtari, Adam N Mamelak, John Mosher, Deborah Arthur, Steve Sands, Peter Weiss, Nancy Lopez, Mauricio DiMauro, Edward Flynn, et al. Dipole localization of human induced focal afterdischarge seizure in simultaneous magnetoencephalography and electrocorticography. *Brain Topography*, 14(2):101–116, 2001.

[78] Paul L Nunez, Ramesh Srinivasan, et al. *Electric fields of the brain: the neurophysics of EEG*. Oxford University Press, USA, 2006.

[79] Stefan Klein, Marius Staring, Keelin Murphy, Max A Viergever, and Josien PW Pluim. Elastix: a toolbox for intensity-based medical image registration. *IEEE transactions on medical imaging*, 29(1):196–205, 2009.

[80] Denis P Shamonin, Esther E Bron, Boudewijn PF Lelieveldt, Marion Smits, Stefan Klein, Marius Staring, and Alzheimer's Disease Neuroimaging Initiative. Fast parallel image registration on cpu and gpu for diagnostic classification of alzheimer's disease. *Frontiers in neuroinformatics*, 7:50, 2014.

[81] Jack L Lancaster, Matthew D Cykowski, David Reese McKay, Peter V Kochunov, Peter T Fox, William Rogers, Arthur W Toga, Karl Zilles, Katrin Amunts, and John Mazziotta. Anatomical global spatial normalization. *Neuroinformatics*, 8(3):171–182, 2010.

[82] Jack L Lancaster, D Reese McKay, Matthew D Cykowski, Michael J Martinez, Xi Tan, Sunil Valaparla, Yi Zhang, and Peter T Fox. Automated analysis of fundamental features of brain structures. *Neuroinformatics*, 9:371–380, 2011.

[83] Jack L Lancaster, Angela R Laird, Simon B Eickhoff, Michael J Martinez, P Mickle Fox, and Peter T Fox. Automated regional behavioral analysis for human brain images. *Frontiers in neuroinformatics*, 6:23, 2012.

[84] Po T Wang, Christine E King, Susan J Shaw, David E Millett, Charles Y Liu, Luis A Chui, Zoran Nenadic, and An H Do. A co-registration approach for electrocorticogram electrode localization using post-implantation mri and ct of the head. In *2013 6th International IEEE/EMBS Conference on Neural Engineering (NER)*, pages 525–528. IEEE, 2013.

[85] Martin Ester, Hans-Peter Kriegel, Jörg Sander, Xiaowei Xu, et al. A density-based algorithm for discovering clusters in large spatial databases with noise. In *kdd*, volume 96, pages 226–231, 1996.

[86] Keinosuke Fukunaga. *Introduction to statistical pattern recognition*. Elsevier, 2013.

[87] Steven M Kaye. Fundamentals of statistical signal processing. detection theory, 1989.

[88] Zoran Nenadic. Information discriminant analysis: Feature extraction with an information-theoretic objective. *IEEE Transactions on Pattern Analysis and Machine Intelligence*, 29(8):1394–1407, 2007.

[89] Nikos K Logothetis, Christoph Kayser, and Axel Oeltermann. In vivo measurement of cortical impedance spectrum in monkeys: implications for signal propagation. *Neuron*, 55(5):809–823, 2007.

[90] James B Ranck Jr. Specific impedance of rabbit cerebral cortex. *Experimental neurology*, 7(2):144–152, 1963.

[91] Charles Nicholson and JOHN A Freeman. Theory of current source-density analysis and determination of conductivity tensor for anuran cerebellum. *Journal of neurophysiology*, 38(2):356–368, 1975.

[92] Yoshio C Okada, J-Ch Huang, Margaret E Rice, Daniel Tranchina, and Charles Nicholson. Origin of the apparent tissue conductivity in the molecular and granular layers of the in vitro turtle cerebellum and the interpretation of current source-density analysis. *Journal of neurophysiology*, 72(2):742–753, 1994.

[93] Daniel R Merrill, Marom Bikson, and John GR Jefferys. Electrical stimulation of excitable tissue: design of efficacious and safe protocols. *Journal of neuroscience methods*, 141(2):171–198, 2005.

[94] Won J Sohn, Po T Wang, Spencer Kellis, Richard A Andersen, Charles Y Liu, Payam Heydari, Zoran Nenadic, and An H Do. A prototype of a fully-implantable charge-balanced artificial sensory stimulator for bi-directional brain-computer-interface (bd-bci). In *2020 42nd Annual International Conference of the IEEE Engineering in Medicine & Biology Society (EMBC)*, pages 3083–3085. IEEE, 2020.

[95] Haoran Pu, Ahmad Reza Danesh, Omid Malekzadeh-Arasteh, Won Joon Sohn, An H Do, Zoran Nenadic, and Payam Heydari. A 40v voltage-compliance 12.75 ma maximum-current multipolar neural stimulator using time-based charge balancing technique achieving 2mv precision. In *2021 IEEE Custom Integrated Circuits Conference (CICC)*, pages 1–2. IEEE, 2021.

[96] Won Joon Sohn, Jeffrey Lim, Po T Wang, Haoran Pu, Omid Malekzadeh-Arasteh, Susan J Shaw, Michelle Armacost, Hui Gong, Spencer Kellis, Richard A Andersen, et al. Benchtop and bedside validation of a low-cost programmable cortical stimulator in a testbed for bi-directional brain-computer-interface research. *Frontiers in Neuroscience*, 16, 2022.

[97] John G Webster. *Medical instrumentation: application and design*. John Wiley & Sons, 2009.

[98] Leslie A Geddes, LE Baker, and AG Moore. Optimum electrolytic chloriding of silver electrodes. *Medical and biological engineering*, 7:49–56, 1969.

[99] Po T Wang, Everardo Camacho, Ming Wang, Yongcheng Li, Susan J Shaw, Michelle Armacost, Hui Gong, Daniel Kramer, Brian Lee, Richard A Andersen, et al. A benchtop system to assess the feasibility of a fully independent and implantable brain-machine interface. *Journal of Neural Engineering*, 16(6):066043, 2019.

[100] Chang Won Lee, Hieu Dang, and Zoran Nenadic. An efficient algorithm for current source localization with tetrodes. In *2007 29th Annual International Conference of the IEEE Engineering in Medicine and Biology Society*, pages 1282–1285. IEEE, 2007.

[101] Madhuvanthi A Kandadai, Jason L Raymond, and George J Shaw. Comparison of electrical conductivities of various brain phantom gels: Developing a 'brain gel model'. *Materials Science and Engineering: C*, 32(8):2664–2667, 2012.

[102] Juha Latikka and Hannu Eskola. The electrical conductivity of human cerebrospinal fluid in vivo. In *World Congress on Medical Physics and Biomedical Engineering 2018: June 3-8, 2018, Prague, Czech Republic (Vol. 1)*, pages 773–776. Springer, 2019.

[103] Karl A Sillay, Paul Rutecki, Kathy Cicora, Greg Worrell, Joseph Drazkowski, Jerry J Shih, Ashwini D Sharan, Martha J Morrell, Justin Williams, and Brett Wingeier. Long-term measurement of impedance in chronically implanted depth and subdural electrodes during responsive neurostimulation in humans. *Brain stimulation*, 6(5):718–726, 2013.

[104] Po T Wang, Colin M McCrimmon, Payam Heydari, An H Do, and Zoran Nenadic. Subspace-based suppression of cortical stimulation artifacts. In *2018 40th Annual International Conference of the IEEE Engineering in Medicine and Biology Society (EMBC)*, pages 2426–2429. IEEE, 2018.

[105] Po T Wang, Colin M McCrimmon, Payam Heydari, An H Do, and Zoran Nenadic. Subspace-based suppression of cortical stimulation artifacts. In *2018 40th Annual International Conference of the IEEE Engineering in Medicine and Biology Society (EMBC)*, pages 2426–2429. IEEE, 2018.

[106] Shun Chi Wu, A Lee Swindlehurst, Po T Wang, and Zoran Zoran Nenadic. Projection versus prewhitening for eeg interference suppression. *IEEE transactions on biomedical engineering*, 59(5):1329–1338, 2012.

[107] Aapo Hyvarinen. Fast and robust fixed-point algorithms for independent component analysis. *IEEE T. Neural Networ.*, 10(3):626–634, 1999.

[108] Fengyu Cong, Tapani Ristaniemi, and Heikki Lyytinen. *Advanced signal processing on brain event-related potentials: filtering ERPs in time, frequency and space domains sequentially and simultaneously*, volume 13. World Scientific, 2015.

[109] Dietrich Lehmann. Multichannel topography of human alpha eeg fields. *Electroencephalography and clinical neurophysiology*, 31(5):439–449, 1971.

[110] Steven M Kay. *Fundamentals of Statistical Signal Processing. Detection Theory.* Prentice-Hall, Englewood Cliffs, New Jersey, 1998.

[111] Ron Kohavi et al. A study of cross-validation and bootstrap for accuracy estimation and model selection. In *Ijcai*, number 2 in 14, pages 1137–1145. Montreal, Canada, 1995.

[112] Won Joon Sohn, Jeffrey Lim, Po T Wang, Haoran Pu, Omid Malekzadeh Arasteh, Susan J Shaw, Michelle Armacost, Hui Gong, Spencer Kellis, Richard A Andersen, et al. A benchtop and bedside validation of a low-cost programmable cortical stimulator in a testbed for bi-directional brain-computer-interface (bd-bci) research. *Frontiers in Neuroscience*, 16:2275, 2016.

[113] 47 C.F.R. 47 c.f.r. part 95. subpart i-medical device radio communications service telecommunication. *Code of Federal Regulations*, 2017.

[114] An H Do, Po T Wang, Christine E King, Andrew Schombs, Steven C Cramer, and Zoran Nenadic. Brain-computer interface controlled functional electrical stimulation device for foot drop due to stroke. In *2012 Annual International Conference of the IEEE Engineering in Medicine and Biology Society*, pages 6414–6417. IEEE, 2012.

[115] Po T Wang, Christine E King, Luis A Chui, An H Do, and Zoran Nenadic. Self-paced brain–computer interface control of ambulation in a virtual reality environment. *Journal of neural engineering*, 9(5):056016, 2012.

[116] An H Do, Po T Wang, Christine E King, Sophia N Chun, and Zoran Nenadic. Brain-computer interface controlled robotic gait orthosis. *Journal of neuroengineering and rehabilitation*, 10(1):1–9, 2013.

[117] Kai J Miller, Eric C Leuthardt, Gerwin Schalk, Rajesh PN Rao, Nicholas R Anderson, Daniel W Moran, John W Miller, and Jeffrey G Ojemann. Spectral changes in cortical surface potentials during motor movement. *Journal of Neuroscience*, 27(9):2424–2432, 2007.

[118] Johanna Ruescher, Olga Iljina, Dirk-Matthias Altenmüller, Ad Aertsen, Andreas Schulze-Bonhage, and Tonio Ball. Somatotopic mapping of natural upper-and lower-extremity movements and speech production with high gamma electrocorticography. *Neuroimage*, 81:164–177, 2013.

[119] Koel Das and Zoran Nenadic. An efficient discriminant-based solution for small sample size problem. *Pattern Recognition*, 42(5):857–866, 2009.

[120] Ronald A Fisher. The use of multiple measurements in taxonomic problems. *Annals of eugenics*, 7(2):179–188, 1936.

[121] Peter E Hart, David G Stork, and Richard O Duda. *Pattern classification*. Wiley Hoboken, 2000.

[122] Claudio Babiloni, Claudio Del Percio, Fabrizio Vecchio, Fabio Sebastiano, Giancarlo Di Gennaro, Pier P Quarato, Roberta Morace, Luigi Pavone, Andrea Soricelli, Giuseppe Noce, et al. Alpha, beta and gamma electrocorticographic rhythms in somatosensory, motor, premotor and prefrontal cortical areas differ in movement execution and observation in humans. *Clinical Neurophysiology*, 127(1):641–654, 2016.

[123] Lena Trebaul, Pierre Deman, Viateur Tuyisenge, Maciej Jedynak, Etienne Hugues, David Rudrauf, Manik Bhattacharjee, François Tadel, Blandine Chanteloup-Foret, Carole Saubat, et al. Probabilistic functional tractography of the human cortex revisited. *NeuroImage*, 181:414–429, 2018.

[124] Simone Russo, Andrea Pigorini, Ezequiel Mikulan, Simone Sarasso, A Rubino, Flavia Maria Zauli, S Parmigiani, Piergiorgio d'Orio, Anna Cattani, Stefano Francione, et al. Focal lesions induce large-scale percolation of sleep-like intracerebral activity in awake humans. *NeuroImage*, 234:117964, 2021.

[125] Ezequiel Mikulan, Simone Russo, Sara Parmigiani, Simone Sarasso, Flavia Maria Zauli, Annalisa Rubino, Pietro Avanzini, Anna Cattani, Alberto Sorrentino, Steve Gibbs, et al. Simultaneous human intracerebral stimulation and hd-eeg, ground-truth for source localization methods. *Scientific Data*, 7(1):1–8, 2020.

[126] Alireza Karimi-Bidhendi, Omid Malekzadeh-Arasteh, Mao-Cheng Lee, Colin M McCrimmon, Po T Wang, Akshay Mahajan, Charles Yu Liu, Zoran Nenadic, An H Do, and Payam Heydari. Cmos ultralow power brain signal acquisition front-ends: design and human testing. *IEEE Transactions on Biomedical Circuits and Systems*, 11(5):1111–1122, 2017.

[127] Omid Malekzadeh-Arasteh, Haoran Pu, Jeffrey Lim, Charles Yu Liu, An H Do, Zoran Nenadic, and Payam Heydari. An energy-efficient cmos dual-mode array architecture for high-density ecog-based brain-machine interfaces. *IEEE Transactions on Biomedical Circuits and Systems*, 14(2):332–342, 2019.

[128] Omid Malekzadeh-Arasteh, Haoran Pu, Ahmad Reza Danesh, Jeffrey Lim, Po T Wang, Charles Y Liu, An H Do, Zoran Nenadic, and Payam Heydari. A fully-integrated 1μw/channel dual-mode neural data acquisition system for implantable brain-machine interfaces. In *2021 43rd Annual International Conference of the IEEE Engineering in Medicine & Biology Society (EMBC)*, pages 5780–5783. IEEE, 2021.

[129] Haoran Pu, Omid Malekzadeh-Arasteh, Ahmad Reza Danesh, Zoran Nenadic, An H Do, and Payam Heydari. A cmos dual-mode brain–computer interface chipset with 2-mv precision time-based charge balancing and stimulation-side artifact suppression. *IEEE Journal of Solid-State Circuits*, 57(6):1824–1840, 2021.

[130] Mao-Cheng Lee, Alireza Karimi-Bidhendi, Omid Malekzadeh-Arasteh, Po T Wang, Zoran Nenadic, An H Do, and Payam Heydari. A cmos inductorless medradio ook transceiver with a 42 μw event-driven supply-modulated rx and a 14% efficiency tx for medical implants. In *2018 IEEE Custom Integrated Circuits Conference (CICC)*, pages 1–4. IEEE, 2018.

[131] Mao-Cheng Lee, Alireza Karimi-Bidhendi, Omid Malekzadeh-Arasteh, Po T Wang, An H Do, Zoran Nenadic, and Payam Heydari. A cmos medradio transceiver with supply-modulated power saving technique for an implantable brain–machine interface system. *IEEE Journal of Solid-State Circuits*, 54(6):1541–1552, 2019.

Appendix A

Co-Registration with Elastix

The process of co-registration allows for the transformation and alignment of two brain images into the same space. We utilize the co-registration process multiple times in this work to align images of ECoG electrodes with its corresponding 3D brain rendering while preserving the dimensions of both images. The co-registration process requires two brain images: one computed tomography (CT) image and one magnetic resonance (MR) image. Post-implantation CT images are used to obtain the ECoG electrode coordinates. Due to the extreme image artifacts of bone and the metallic electrodes, CT images are unsuitable for segmenting brain tissue, so we use MR images to isolate the brain tissue. These MR images can be either pre- or post- implantation images, with post-implantation images providing the best spatial fidelity as they capture the tissue deformities from surgeries. Once the MR and CT images are chosen, the MRI must be processed to extract the brain tissue A.1. As the dimensions of the two images often do not match, the MRI is first non-rigidly transformed to the CT space using the Elastix toolbox [79, 80]. A normalized mutual information similarity metric is used to best align matching features of the two images. We then used the Mango [81, 82, 83] segmentation plugin to isolate the brain tissue from the transformed MR image.

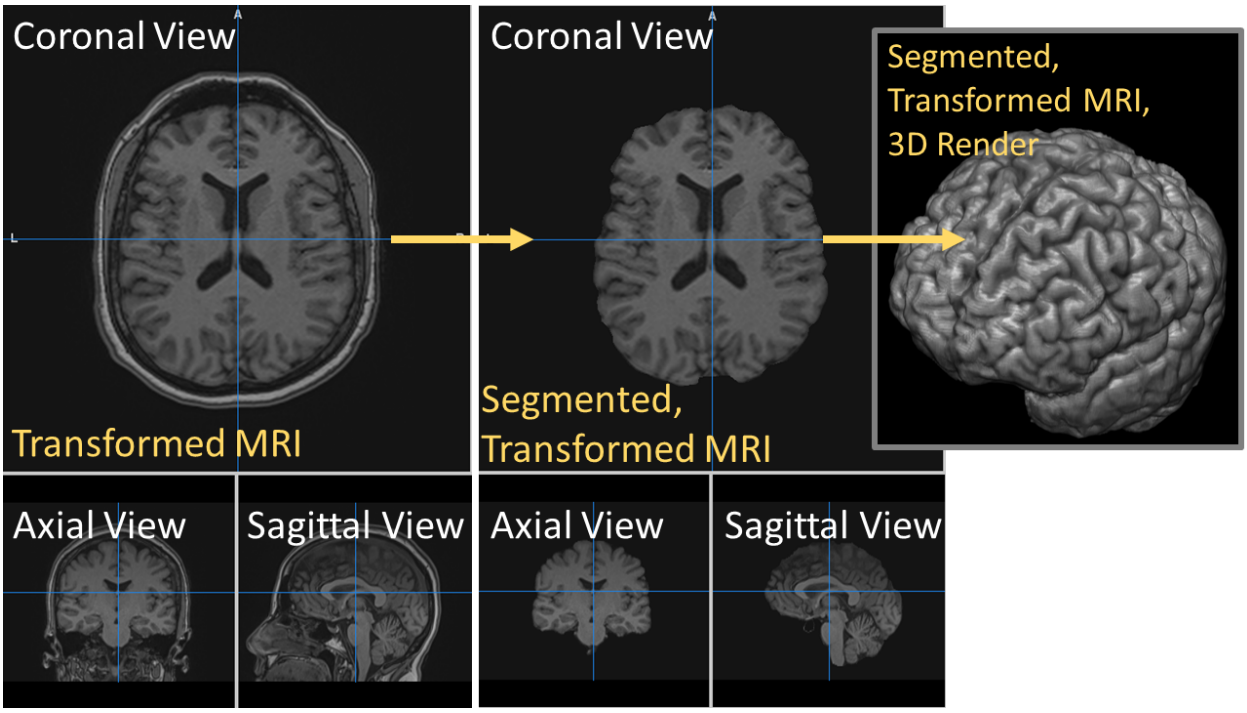

Figure A.1: MRI processing pipeline for co-registration. MRI image is first transformed to CT space, then segmented to isolate the brain tissue.

The electrode coordinates are then obtained using the CT images. As the electrodes appear as high-density artifacts in CT, they can be easily identified and localized using a DBSCAN approach [85]. By thresholding the image intensity data from the CT images, the electrodes can be isolated and a DBSCAN algorithm can obtain the coordinates for those electrodes (cf. Figure A.2).

Finally, a custom MATLAB script is used to overlay the isolated electrodes onto the segmented brain to complete the MR-CT co-registration. This overlay can be visualized as a 3D render which shows the ECoG electrodes over their cortical locations (cf. Figure A.3).

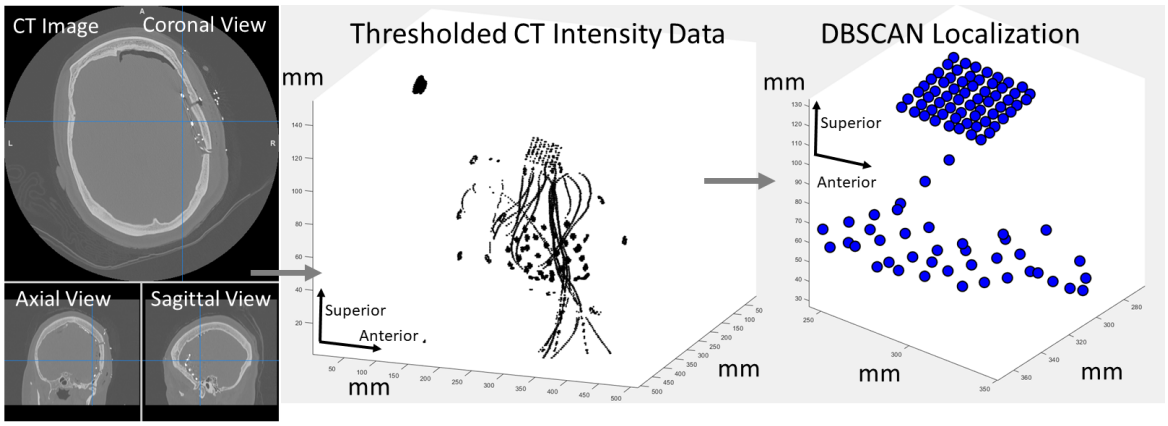

Figure A.2: Segmentation of ECoG electrode coordinates from CT image. Intensity data from CT images are first thresholded then segmented to isolate electrode clusters. Electrode clusters are then localized using DBSCAN to obtain electrode coordinates.

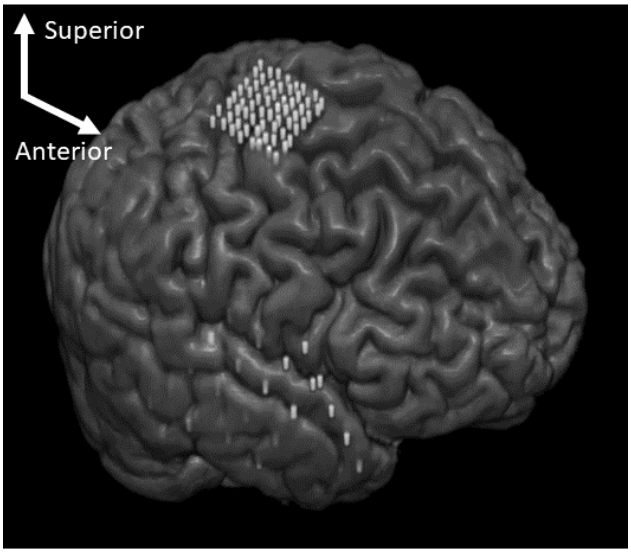

Figure A.3: Final result of MR-CT co-registration process.

Appendix B

Supplemental Artifact Characterization Tables

Table B.1: WCD for stimulation channels in representative grids across all subjects

Stim. Channel	WCD (mm)										
Current Amp (mA):	2	3	4	5	6	7	8	9	10	11	12
Subject 1											
LPG 4-5	12.23		12.39		12.42		12.44		12.13		
LPG 3-4	16.20		16.32								
LPG 5-10	15.10		15.19		15.26						
LPG 9 -10	12.06		12.17		12.23		12.24				
LPG 8-9	16.19		16.21		16.79		17.33				
LPG 7-8	16.05		16.12		16.13		15.49				
LPG 6-7	15.40										
LPG 1-2	15.07		18.07								
LPG 2-3	15.87										
LPG 11-12	14.83		38.01		38.34						

LPG 12-13	16.09		16.09		28.77						
LPG 13-14	16.72		17.32		17.93		25.53				
Subject 2											
LTG 1-2	14.71		15.13		15.49		17.69		18.96		
LTG 3-4	15.82		16.20		16.44		18.31		19.52		
LTG 5-10	14.35		14.63		14.82		14.92		15.01		16.95
LTG 6-7	15.13		15.57		36.45		36.17		36.15		
LTG 8-9	16.03		16.43		17.77		19.24		19.26		20.27
LTG 14-15	12.43		12.72		18.17		23.17		32.91		33.72
Subject 3											
LIHG 3-11		4.43	4.49	4.68							
LIHG 5-13		4.64	4.68								
LIHG 6-14		4.60	4.89	5.02							
LIHG 17-25		4.88		5.80		7.05		8.11	8.49		9.12
LIHG 19-27		5.11		6.48			8.07		8.71		
LIHG 20-28		4.73	4.78	5.47		6.93					
LIHG 21-29		4.65		5.01		6.10		7.34			
LIHG 22-30		4.66		7.80							
LIHG 23-30		6.30		7.20		7.79					
LIHG 7-15		5.26		5.55		6.47					
LIHG 15-23		5.38		5.51		6.24		5.10	6.95		
Subject 4											
RCG 7-8	5.40		6.90		8.12		9.60				
RCG 5-6	13.72		13.73		13.78		14.22				
RCG 3-4	6.41		10.13								
RCG 2-3	6.76		8.86								
RCG 1-2	5.92		5.91		7.08	9.78					

RCG 15-16	6.26		8.35		9.83						
RCG 13-14	8.04		9.51		10.67		11.25				
RCG 11-12	6.79		10.02		11.84		13.08		13.70		
RCG 9-10	6.04		8.69		10.49		11.87		13.96		
RCG 23-24	6.96		9.23		11.54		12.01				
RCG 21-22	7.49		10.09		10.71		11.14	11.10			
RCG 19-20	7.40		10.03		11.42		12.43		13.49	13.82	14.05
RCG 20-22	11.51		12.41		14.09		15.66		16.23		
RCG 17-18	8.26		9.89		10.19		11.54				
RCG 31-32	6.42		6.54		8.63						
RCG 29-30	7.53		8.60		9.41		10.02				
RCG 27-28	7.50		9.33		9.87		10.33		10.34		
RCG 25-26	11.95		13.30		14.30		14.84		8.13		
RCG 17-25	9.41		15.76								
RCG 18-25	9.33		13.96		13.97						
RCG 17-26	13.61		25.81		25.89						

Table B.2: Dipole Fits with Coefficient Values for representative grids across all subjects

Subject 1: LPG Summary					
Stim. Channel	Stim Range (mA)	# of Epochs	$\hat{k}$ (Ω*mm)	$\hat{n}$ (mV)	R^2
LPG4-5	2–8	5	2.2	-0.109	0.66
LPG3-4	2–4	2	3.5	-0.071	0.91
LPG5-10	2–6	3	3.3	0.045	0.5
LPG9-10	2–8	4	2.4	-0.132	0.74
LPG8-9	2–8	4	2.8	-0.075	0.89
LPG7-8	2–6	4	2.8	0.031	0.87

LPG6-7	2	1	6.4	0.026	0.95
LPG1-2	2–4	2	5.7	0.056	0.88
LPG2-3	2	1	6.2	-0.011	0.99
LPG11-12	2–6	5	4.3	0.161	0.43
LPG12-13	2–6	3	5.2	-0.013	0.88
LPG13-14	2–8	4	4.9	-0.133	0.92
Subject 2: LTG Summary					
LTG1-2	2–10	10	3.2	-0.023	0.9
LTG3-4	2–10	10	3.6	0.09	0.86
LTG5-10	2–12	12	2.8	0.049	0.76
LTG6-7	2–10	10	3.4	-0.099	0.67
LTG8-9	2–10	10	3.5	0.125	0.91
LTG14-15	2–12	12	2.8	0.407	0.68
Subject 3: LIHG Summary					
LIHG1-9	3–4	2	2.6	-0.054	0.81
LIHG3-11	3–5	3	2	0.001	0.87
LIHG5-13	3–4	2	2.4	0.035	0.75
LIHG6-14	3–5	3	2.1	0.127	0.81
LIHG17-25	3–12	6	1.5	-0.244	0.72
LIHG19-27	3–10	5	1.8	-0.19	0.77
LIHG20-28	3–7	4	2.1	-0.112	0.77
LIHG21-29	3–9	5	1.8	-0.113	0.78
LIHG22-30	3–5	4	2.3	-0.084	0.8
LIHG23-31	3–7	4	2.5	-0.179	0.82
LIHG7-15	3–7	3	1.8	0.003	0.67
LIHG15-23	3–10	6	1.1	-0.072	0.57
Subject 4: LIHG Summary					

RCG7-8	2–8	4	1.7	0.425	0.67
RCG5-6	2–8	4	4.5	-0.105	0.46
RCG3-4	2–8	4	3.5	-0.137	0.8
RCG2-3	2–4	2	4.8	-0.052	0.88
RCG1-2	2–7	4	2.3	-0.064	0.79
RCG15-16	2–6	3	2.6	0.324	0.92
RCG13-14	2–6	4	3.3	0.15	0.72
RCG11-12	2–10	4	3.5	0.059	0.74
RCG9-10	2–10	6	3.3	-0.084	0.75
RCG23-24	2–8	4	2.3	0.457	0.86
RCG21-22	2–9	5	3	0.058	0.91
RCG19-20	2–12	7	3.3	0.045	0.91
RCG20-22	2–10	5	2.9	0.127	0.89
RCG17-18	2–8	5	4.2	-0.12	0.86
RCG31-32	2–6	3	2.3	0.256	0.74
RCG29-30	2–8	4	3.5	0.129	0.95
RCG27-28	2–10	5	3.1	-0.004	0.87
RCG25-26	2–10	5	2.1	-0.257	0.33
RCG17-25	2–4	2	9.2	-0.149	0.37
RCG18-25	2–6	3	6.7	0.131	0.46

Appendix C

Additional Baseline Control Experiments for PWNP and ICA Artifact Suppression

In our baseline control experiments in Section 4.3.2 and 4.3.3, the PWNP artifact suppression method may have benefited over the ICA artifact suppression method from the fact that the baseline data epoch in this control experiment had been used to calculate the pre-whitening matrix, $\mathbf{\Sigma}_B^{-\frac{1}{2}}$, (see Equation 4.1). To rule this out, we performed control experiments on additional baseline epochs, while retaining the same PWNP and ICA parameters. ECoG results are shown for PWNP and ICA in Figure C.1 and Figure C.2, respectively. Similarly, the MEA results are shown for PWNP and ICA in Figure C.3 and Figure C.4, respectively. For all of these, the results are further quantified in Table C.1.

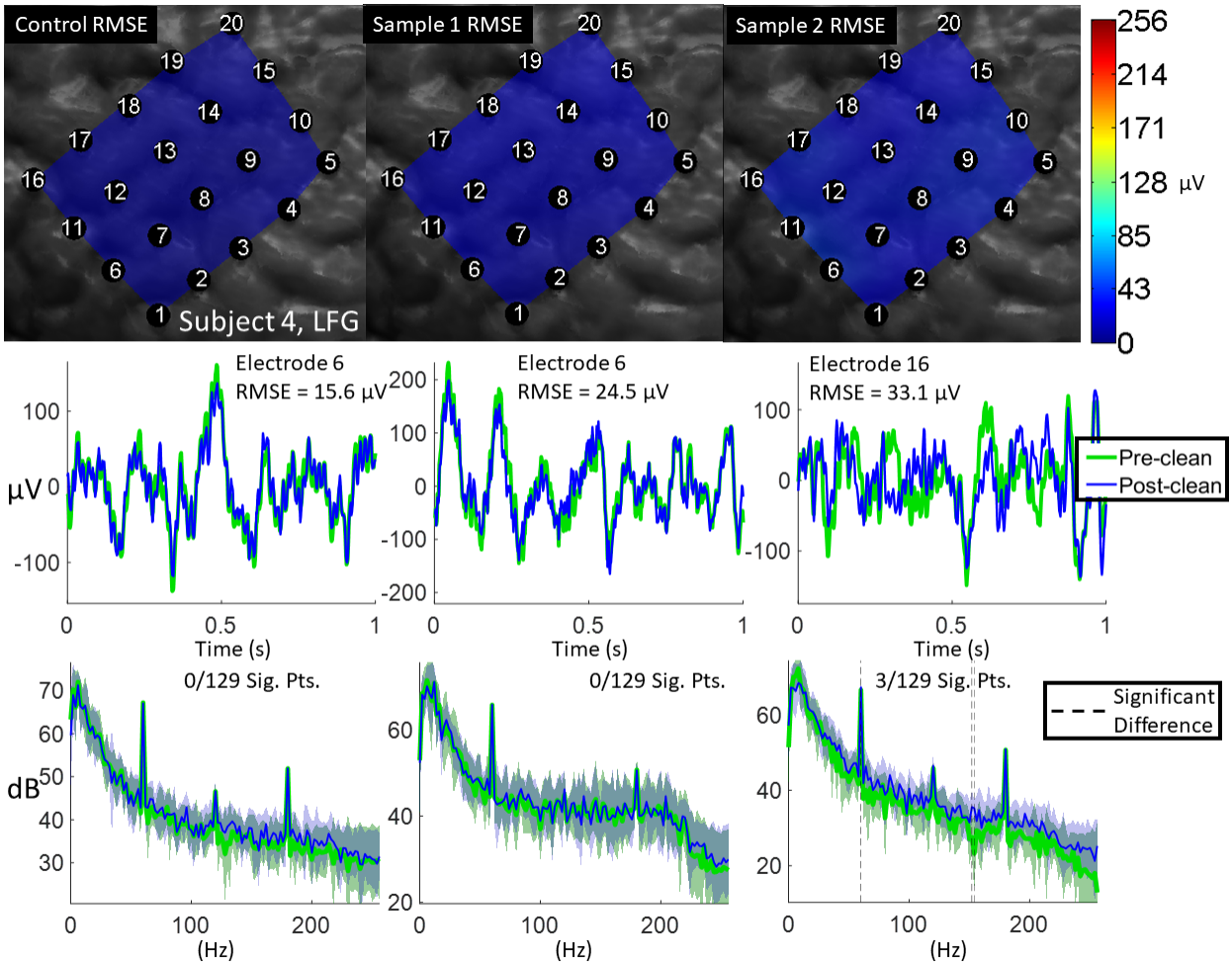

Figure C.1: Baseline control experiment results for PWNP method in ECoG data. (Top) RMSE values (Equation 4.6) interpolated and mapped to MR-CT co-registered images of the ECoG grids from Subject 4. Color bar range is from 0 μV to 256 μV (maximum absolute voltage of the baseline data). (Middle) Representative baseline time domain examples before and after artifact suppression (Bottom) Representative frequency domain examples (mean PSD) from the same electrode before/after artifact suppression. Dashed lines indicate frequencies where the power distribution significantly differed before and after artifact suppression (signed rank test, $p<0.01$).

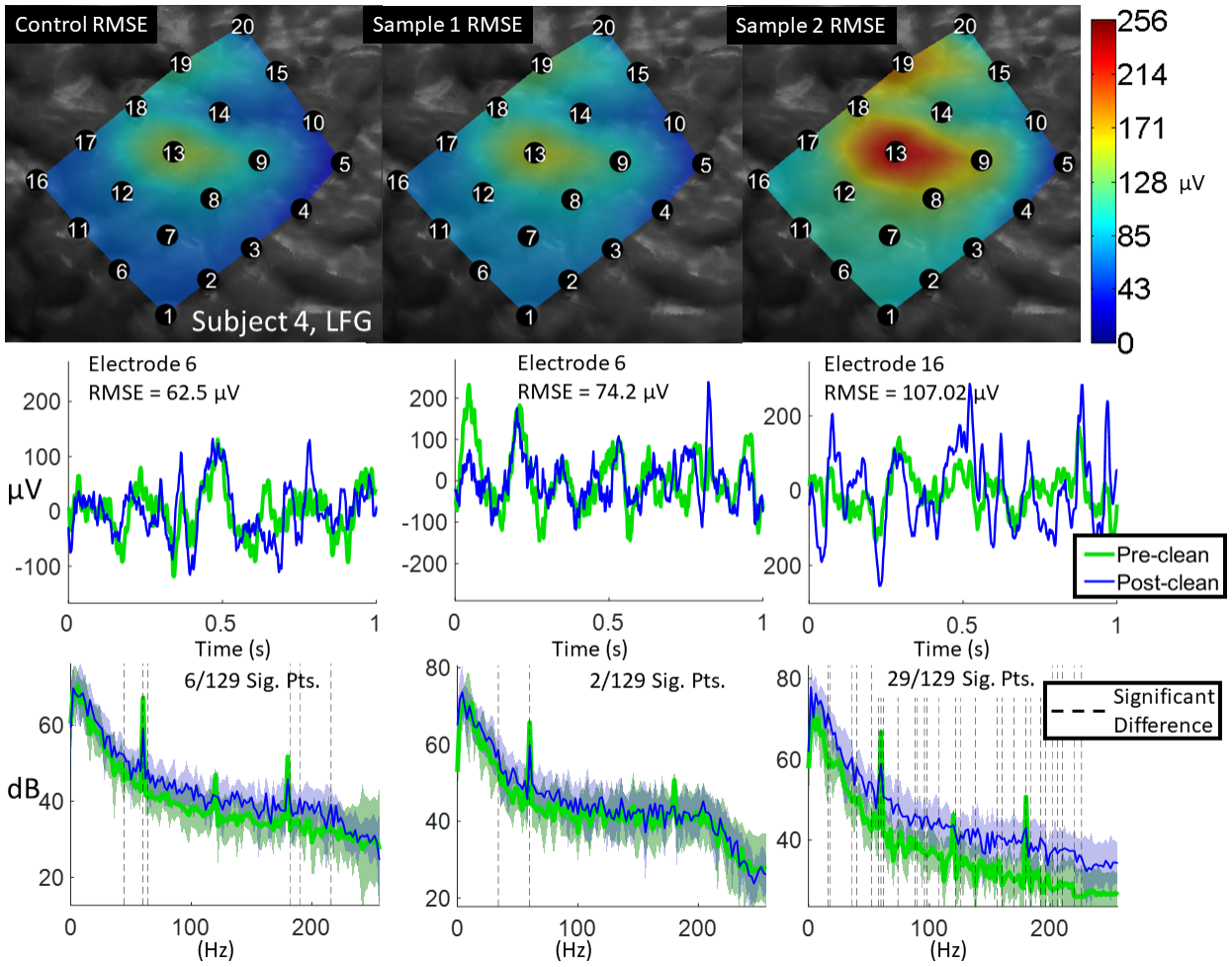

Figure C.2: Baseline control experiment results for ICA method in ECoG data. (Top) RMSE values (Equation 4.6) interpolated and mapped to MR-CT co-registered images of the ECoG grids from Subject 4. Color bar range is from 0 μV to 256 μV (maximum absolute voltage of the baseline data). (Middle) Representative baseline time domain examples before and after artifact suppression (Bottom) Representative frequency domain examples (mean PSD) from the same electrode before/after artifact suppression. Dashed lines indicate frequencies where the power distribution significantly differed before and after artifact suppression (signed rank test, $p<0.01$).

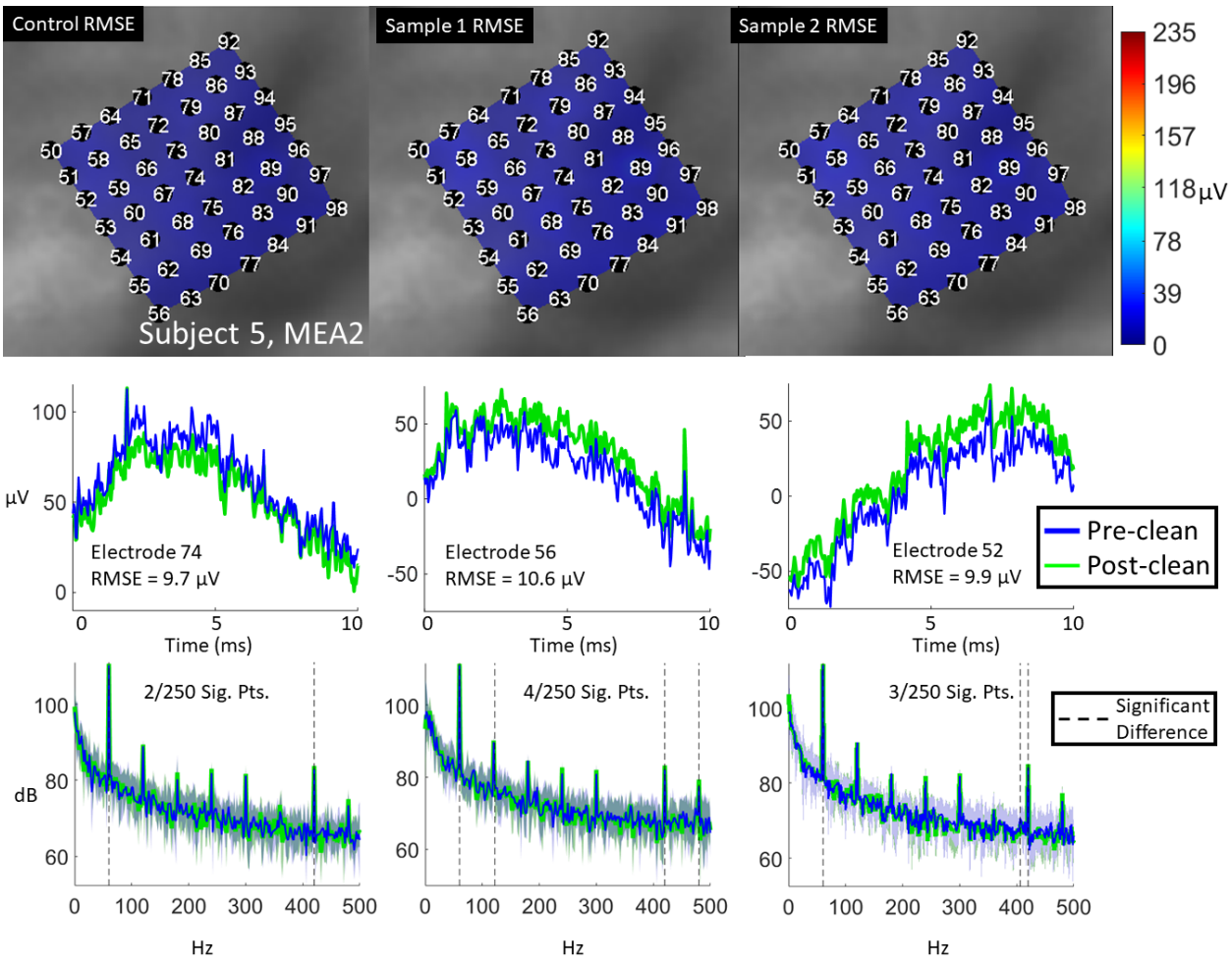

Figure C.3: Baseline control experiment results for PWNP method in MEA data. (Top) RMSE values interpolated and mapped to estimated MEA2 electrode locations. Color bar range is from 0 μV to 235 μV (maximum absolute voltage of the baseline data). (Middle) Representative baseline time domain examples before and after artifact suppression. (Bottom) Representative frequency domain examples (mean PSD) from the same electrode before/after artifact suppression. Dashed lines indicate frequencies where the power distribution significantly differed before and after artifact suppression (signed rank test, $p<0.01$)

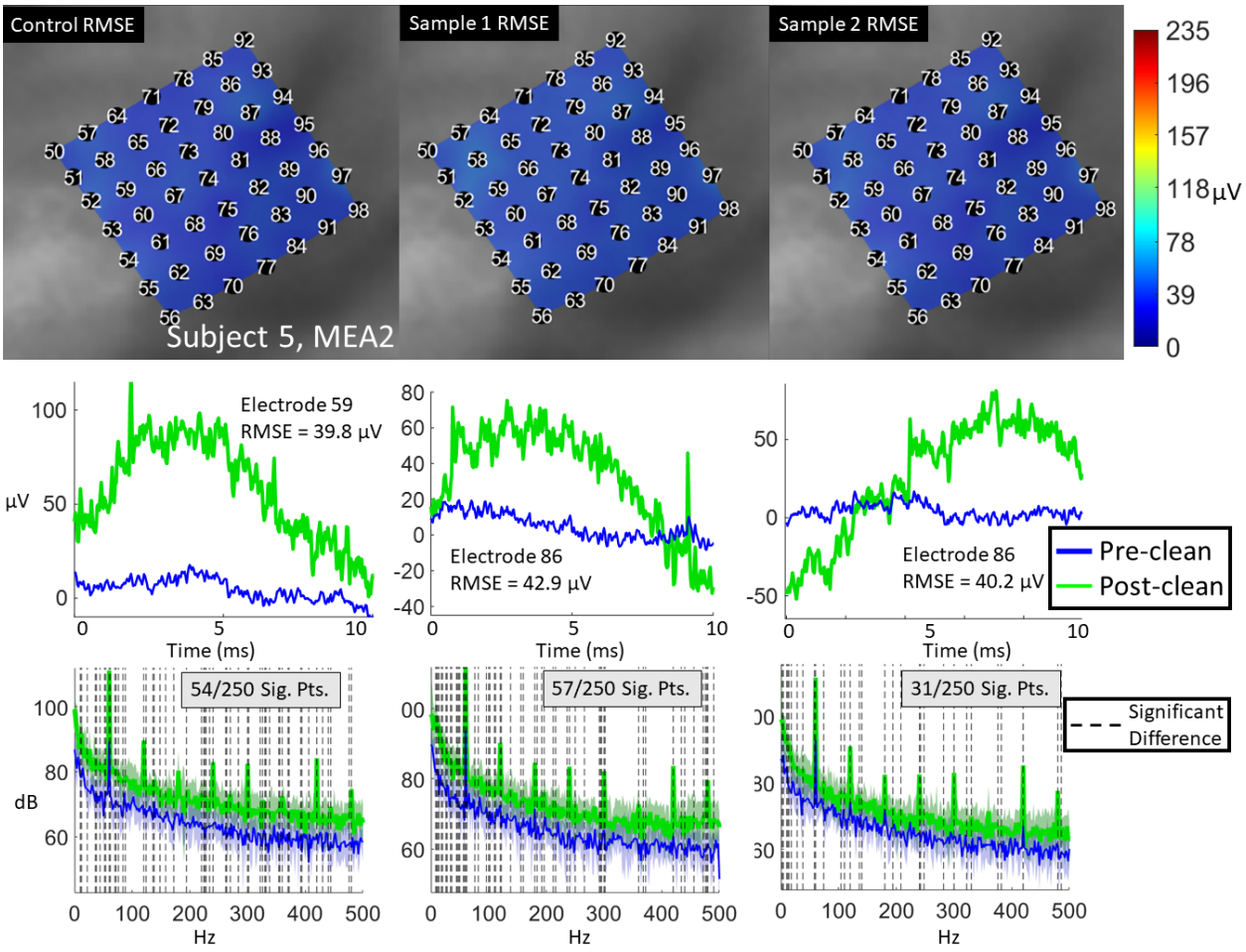

Figure C.4: Baseline control experiment results for ICA method in MEA data. (Top) RMSE values interpolated and mapped to estimated MEA2 electrode locations. Color bar range is from 0 μV to 235 μV (maximum absolute voltage of the baseline data). (Middle) Representative baseline time domain examples before and after artifact suppression. (Bottom) Representative frequency domain examples (mean PSD) from the same electrode before/after artifact suppression. Dashed lines indicate frequencies where the power distribution significantly differed before and after artifact suppression (signed rank test, $p<0.01$)

Table C.1: Electrode-averaged RMSE values and corresponding standard deviations for baseline control experiments.

Data Segment	RMSE (μV) (Mean $\pm$ 1SD)	Max Abs. Amp. (μV)
	ECoG Data (PWNP)	
Control	15.3 $\pm$ 2.3	206
Sample 1	23.5 $\pm$ 3.9	256
Sample 2	34.5 $\pm$ 6.3	252
	MEA Data (PWNP)	
Control	10.5 $\pm$ 2.1	168
Sample 1	11.5 $\pm$ 2.5	235
Sample 2	10.9 $\pm$ 2.1	192
	ECoG Data (ICA)	
Control	68.8 $\pm$ 27.4	206
Sample 1	79.7 $\pm$ 27.2	256
Sample 2	112.1 $\pm$ 45.1	252
	MEA Data (ICA)	
Control	42.1 $\pm$ 6.3	168
Sample 1	45.5 $\pm$ 5.4	235
Sample 2	42.9 $\pm$ 6.1	192

Appendix D

Brain Computer Interface Decoder Training and Implementation

Online segments are acquired for decoding in 750 ms sliding windows. These online segments were represented as time series data $\mathbf{X} \in \mathbb{R}^{n \times t}$, where n is the number of channels and t is the number of samples in the sliding window time series. Using a fast Fourier transform, these time series can be transformed into frequency domain data $\mathbf{Y} \in \mathbb{R}^{n \times f}$ where $f = N/f_s$ is the frequency resolution of the signal. In the case of the BD-BCI, $f_s = 500$ Hz is the sampling frequency and $N = 750$ ms. These frequency domain data are further processed into PSDs, which can be integrated over the relevant physiological bands, e.g. $\mu - \beta$ and high γ bands, in 2 Hz bins. To prepare neural training data for CPCA, both idle and move sample data are vertically reshaped into $\bar{Y} \in \mathbb{R}^{nf \times 1}$.

D.1 Classwise Principal Component Analysis (CPCA)

The first step for feature extraction ($f^* = T_{\text{LDA}}\Phi_{\text{CPCA}}(d)$) is to perform CPCA [88] to reduce the dimensionality of the data. CPCA is performed in the following steps:

1. Calculate the class-specific covariance:

$$\mathbf{\Sigma}_i = \bar{Y}\bar{Y}^T \tag{D.1}$$

for $i = 1....c$ where c is the total number of classes. For the binary state decoder context, we have $c = 2$, one class for each of the move (C_M) and idle (C_I) subspaces.

2. We then perform principal component analysis (PCA) by calculating the eigenvalues and eigenvectors of each class-specifc covariance

$$\mathbf{\Sigma}_i V = \lambda V \tag{D.2}$$

where V contains the eigenvectors and λ contains the eigenvalues of the class-specific covariance matrix. The dimension of the data is reduced by applying a threshold to the eigenvalues at the mean eigenvalue, $\bar{\lambda}$. The eigenvectors corresponding to $\lambda < \bar{\lambda}$ are then nulled.

3. Calculate the between-class covariance

$$\mathbf{\Sigma_b} = \sum_{i=1}^{c} p_i(\mu_i - \mu)^T(\mu_i - \mu) \tag{D.3}$$

where μ_i are class-specific means and the prior probability of each class is p_i, which is calculated as the fraction of samples in class i to the total number of samples among all classes. Note that in the binary decoder context, with equal samples for move and idle conditions, the prior probabilities are equal ($p_I = p_M$). The global mean μ is

calculated as:

$$\mu = \sum_{i=1}^{c} p_i \mu_i \tag{D.4}$$

4. Perform PCA on the between-class covariance as was done for the class-specific covariance (Step 2)

5. Augment the class-specific eigenvectors to the between-class eigenvectors

6. Orthonormalize the resulting augmented matrix to obtain the CPCA transformation matrix $\mathbf{\Phi}_{\text{CPCA}}$

D.2 Linear Discriminant Analyis (LDA)

To further reduce the dimension of the data down to a 1-D feature f^*, we perform a linear discriminant analysis [120, 121] to obtain the linear discriminant transformation matrx, $\mathbf{T}_{\text{LDA}}$. The steps to do so are as follows:

1. Compute the m-dimensional class-specific means (μ_i), prior probabilities (p_i) and class-specific covariances (Σ_i). Here, m is the dimension of the data after application of the CPCA transformation matrix.

2. Calculate the within-class covariance matrix $\mathbf{\Sigma_w}$

$$\mathbf{\Sigma_w} = \sum_{i=1}^{c} p_i \mathbf{\Sigma}_i \tag{D.5}$$

3. Next we calculate the criterion function $J(\cdot)$ as a generalized Rayleigh quotient [121]:

$$J(\mathbf{z}) = \frac{\mathbf{z}^T \mathbf{\Sigma_b} \mathbf{z}}{\mathbf{z}^T \mathbf{\Sigma_w} \mathbf{z}} \tag{D.6}$$

where $\mathbf{z}$ is the matrix that projects the samples onto the discriminating line. The $\mathbf{z}$ that maximizes $J(\cdot)$ satisfies the following equation:

$$\mathbf{\Sigma_b z} = \lambda \mathbf{\Sigma_w z} \tag{D.7}$$

where λ are the eigenvalues of the within-class covariance matrix.

4. In the case that $\Sigma_{\mathbf{w}}$ is non-singular, then $\mathbf{z}$ can be solved for using eigenvalue decomposition:

$$\mathbf{\Sigma_w^{-1} \Sigma_b z} = \lambda \mathbf{z} \tag{D.8}$$

From this, we can infer that the criterion function is maximized then when the LDA transformation matrix $\mathbf{T}_{\text{LDA}}$ is equal to the eigenvectors of $\mathbf{\Sigma_w^{-1} \Sigma_b}$. Using this, there will be at most $c-1$ eigenvectors with non-zero, real eigenvalues, thus mapping the m-dimensional data from the CPCA transformation onto a $c-1$ dimension.

D.3 Bayesian Linear Discriminant Classification

Having obtained both CPCA and LDA transformation matrices, we can calculate the feature $f^* = T_{\text{LDA}} \Phi_{\text{CPCA}}(d)$. Classification is performed on f^* using a Bayesian linear classifier [120]. We first calculate the overall risk:

$$R = \int R(\alpha(f^*)|f^*) P(f^*) df^* \tag{D.9}$$

where $\alpha(f^*)$ is the decision function for the action α, which is the determination of the state. The conditional risk for α is then:

$$R(C_M|f^*) = \lambda_{C_M,C_I} P(C_I|f^*) + \lambda_{C_M,C_M} P(C_M|f^*) \tag{D.10}$$
$$R(C_I|f^*) = \lambda_{C_I,C_M} P(C_M|f^*) + \lambda_{C_I,C_I} P(C_I|f^*)$$

where $R(C_I|f^*)$ is the conditional risk of classifying f^* as "Class 1" (C_M) and $R(C_I|f^*)$ is the conditional risk of classifying f^* as "Class 2" (C_I). The factors λ_{C_i,C_j} are the cost of identifying Class i as Class j, where $j \in [I, M]$. Using these risks, the feature f^* is classified as the class with the lower risk. Expressed mathematically, this classification criteria is:

$$\frac{R(C_M|f^*)}{R(C_I|f^*)} \underset{C_M}{\overset{C_I}{\gtrless}} 1 \tag{D.11}$$

Using D.10, we can also express the classification in terms of conditional probabilities:

$$\frac{(\lambda_{C_M,C_I} - \lambda_{C_I,C_I}) P(C_I|F^*)}{(\lambda_{C_I,C_M} - \lambda_{C_M,C_M}) P(C_M|F^*)} \underset{C_M}{\overset{C_I}{\gtrless}} 1 \tag{D.12}$$

. Note that for our binary state decoder, we assume an equal prior probability for each state ($P(C_M) = P(C_I)$ and an equal probability for false classification (i.e. $\lambda_{C_M,C_I} = \lambda_{C_I,C_M}$). Additionally, we assign no penalty for the identification of the correct state (i.e. $\lambda_{C_M,C_M} = \lambda_{C_I,C_I} = 0$) The posterior probabilities can then be calculated using Bayes' Formula:

$$P(C_i|f^*) = \frac{P(f^*|C_i)P(C_i)}{P(f^*)} \tag{D.13}$$

which gives the posterior probability of class i given the feature f^* as the likelihood ($p(f^*|C_i)$ times the prior ($P(C_i)$) divided by the evidence $P(f^*)$. After substituting using Bayes'

Formula, our classification criteria becomes:

$$\frac{P(f^*|C_I)}{P(f^*|C_M)} \underset{C_M}{\overset{C_I}{\gtrless}} 1 \tag{D.14}$$

We then calculate the $P(f^*|C_i)$ for each class as:

$$P(f^*|C_i) = \frac{P_{\text{PDF}}(f^*|C_i)P(C_i)}{P_{\text{PDF}}(f^*)} \tag{D.15}$$

where $P_{\text{PDF}}(f^*|C_i)$ is the conditional probability density function of features for Class i. These probability density functions are generated using the data collected in the BCI training procedure. Assuming that the features are conditionally Gaussian, we can define the parameters of the linear Bayesian classifier as $f|C_i$ $\mathbb{N}(\hat{\mu_{C_i}}, \hat{\sigma}^2)$ where μ_{C_i} is the conditional sample means for Class i training data and $\hat{\sigma}^2$ is the unconditional sample variance of the features [121].